# TEMPERATURE COUPLING EFFECTS IN RADIATIVELY HEATED PARTICLE-LADEN FLOWS

By
Ji Hoon Kim and John Eaton

Prepared with support from
the Predictive Science Academic Alliance Program II


Report No. TF-188

Flow Physics and Computational Engineering Group
Department of Mechanical Engineering
Stanford University
Stanford, CA 94305

May 2022

# Temperature Coupling Effects in Radiatively Heated Particle-Laden Flows

By

Ji Hoon Kim and John Eaton

Prepared with support from
the Predictive Science Academic Alliance Program II

Report No. TF-188

Flow Physics and Computational Engineering Group
Department of Mechanical Engineering
Stanford University
Stanford, CA 94305

May 2022

# Abstract

Turbulent particle-laden flows are common in many natural phenomena and engineering applications. While particle-laden turbulence is a relatively well-studied subject, not many studies address the concurrent effect of an radiative heat transfer on the multiphase system. Understanding such an interaction can be key to designing effective spray combustors, fire suppression systems, and particle solar receivers. Using the particle solar receiver as a test bed for investigation, this work aims to experimentally investigate the coupling between radiation, turbulence, and particles in such a system using two different flow configurations of a duct flow and an isokinetic co-flowing jet. The goals of the work are to examine the effects of preferential concentration on the behavior of the radiation transport through the disperse medium and the convective heat transfer between the carrier and disperse phase. In addition, it also aims to study the converse effect of how the radiative heating can effect the clustering behavior of the particles by examining measures of preferential concentration of particles in the flow in the presence of radiative heating. The study finds that the preferential concentration of particles can cause the radiation transmission to deviate from a classical Beer's Law extinction behavior, due to increased line of sight distances in the medium. Measurements of the carrier phase temperature statistics show that large coherent particles clusters dominate the modulation of the gas phase temperature, especially in the boundary layer in wall-bounded flows. Measurements of the radial distribution function, clustering index, and Voronoi cell area PDFs all indicated a reduction of preferential concentration within clusters, particularly in denser clusters with smaller associated separation length scales, which correspond to the most intensely heated regions of the flow. Particle velocity statistics showed

evidence of bulk turbulence modification by radiative heating, as particle velocity fluctuations were dampened. This was likely caused by variable property effects from temperature-dependent properties, specifically from the increase in fluid kinematic viscosity. Buoyancy and dilatation effects were identified as possible mechanisms for turbulence modification at the smaller cluster scales, supported by scaling analyses and directional measures of preferential concentration.

# Acknowledgments

The authors acknowledge the support of the Department of Energy Predictive Science Academic Alliance Program II.

# Contents

# List of Tables

# List of Figures

# Chapter 1

# Introduction

## 1.1 Motivation

Particle-laden flows are a subset of a broader range of flows classified as multiphase flows. Most flows can be categorized as single or multi-component, and single or multi-phase. An example of a multi-component flow would be the flow of air, which is made up of components such as nitrogen and oxygen. A multi-phase flow, as its name implies constitutes multiple different phases, which indicates the state of matter (such as solid, liquid, or gas). Multiphase flows can be further subdivided into gas-liquid, gas-solid, liquid-solid, and three-phase flows. This work aims to study a specific type of flow called particle-laden flows. In a particle-laden flow small solid or liquid particles are dispersed into a gas or liquid phase. Sometimes the distinction is made between particle-laden and droplet-laden flows, where the former has solid particles dispersed in liquids or gases, and the latter has liquids dispersed in a gas phase. It is worth noting that while the distinction is important in many cases, many of the statements made for particle-laden flows can also be made for droplet-laden flows. The particles or droplets that are dispersed in the fluids are often referred to as the dispersed phase, while the fluid carrying the particles are referred to as the carrier phase.

Particle-laden flows are ubiquitous in both nature and engineering applications. In

nature, we can find particle-laden flows in volcanic plumes, where small ash aggregates are carried upwards into the atmosphere by the buoyant heated air-ash mixture, as shown in Figure 1.1a. Correctly predicting the dispersion and sedimentation of ash aggregates in the atmosphere is critical for the safety of nearby inhabitants and air traffic. The study of atmospheric transport of particles, however, are not limited to just volcanic plumes; predictions of atmospheric aerosols are important in determining the global radiative balance (IPCC, 1995). The interaction between gas and particles are also critical in the study of protoplanetary discs and planet formation; vertical sedimentation from drag on small particles in the protoplanetary disc is necessary for the creation of a dense midplane of solids from which larger objects can grow (Youdin and Johansen, 2007). An example of a protoplanetary disc is shown in Figure 2.12b, around the nascent star HL Tauri. In engineering applications, particle-laden flows are commonly found in combustion, where liquid or solid fuel often is dispersed in a gas phase oxidizer. A fuel injector is a common way to disperse droplets of fuel in a diesel engine, and the manner of the injection of the fuel can be critical to the performance of the engine. For instance, the droplet spacing of the fuel in a combustor can affect pollutant levels and fuel consumption rate (Law, 2006). Particle solar receivers, as shown in Figure 1.1c, work to gather radiative energy from the sun to convert to useful work. These receivers rely on particles dispersed in a working fluid to absorb radiative thermal energy, which is then convectively transferred into the fluid.

In the aforementioned examples of aerosols or cloud droplets in the atmosphere, combustion of fuel droplets, and particle solar receivers, another key aspect of understanding the interaction involves radiative heat transfer. In the case of aerosols and droplets, understanding the effect of the particle phase on radiation transport through the atmosphere can sometimes be the key motivation to predicting the behavior of the particle phase, as the primary objective of these studies is to compute the global heat balance and its effect on climate change. In combustors, radiative transfer can play an important role, as it can control charge heating in furnaces and is a key mechanism in thermal heat losses (dos Santos et al., 2008). In particle solar receivers, turbulent fluctuations and the preferential concentration of the particle phase can have a strong influence on the heat transfer statistics (Pouransari and Mani, 2017).

These examples show that while particle-laden flows subject to radiation are just a special case of the general particle-laden flows, they have relevance in a variety of applications. When studying a potentially complex multi-physics phenomenon such as this, it is necessary to construct an experiment in a relatively simple, canonical geometry to simplify the problem where possible. The present work aims to study the three-way interaction between radiation, turbulence, and disperse particles in two simple geometries, a square duct flow and a co-flowing sqaure jet.

## 1.2 Overview and Literature Review

### 1.2.1 Particle-laden turbulent flows and preferential concentration

Flows in the aforementioned applications and phenomena usually are turbulent. A turbulent flow is characterized by random fluid motions and swirling eddies. The large, energy containing turbulent flow structures cascade the energy down to much smaller structures, resulting in a large spectrum of length and time scales. Particles suspended in a turbulent carrier phase can interact with these structures, and if the flow parameters are right, can distribute themselves non-uniformly within the flow. The instantaneous particle field can become correlated with the turbulent motions, forming clusters with high concentrations of particles, and voids of essentially pure gas. This behavior is referred to as preferential concentration. Accurately capturing the behavior of the preferential concentration of particles is often times key to predicting the overall system behavior. However, predicting the turbulence alone can often be challenging, but the addition of particles that potentially do not distribute uniformly adds another layer of complexity to the problem. Due to the spectrum of scales in the underlying turbulence, inertial particles in turbulence can also display a large range of scales in their clustering behavior. If the characteristic particle length scales are smaller than the smallest flows scales, then that introduces additional computational challenges as the smaller length scales either need to be resolved or modeled. In turbulent flows this smallest length scale is the length scale at which

(a) A volcanic plume over Sicily's Mount Etna, (source: photograph by Boris Behncke).

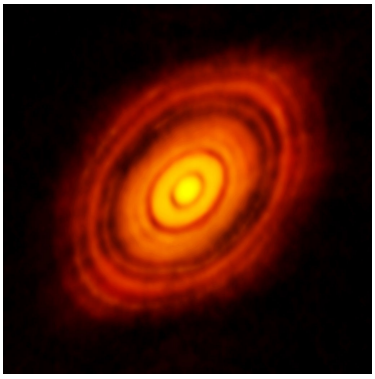

(b) The protoplanetary disk of HL Tauri, from the Atacama Large Millimeter Array (source: European Southern Observatory).

(c) Sandia National Laboratory's High Temperature Falling Particle Receiver (source: Sandia National Labs).

Figure 1.1: Particle laden flows in a variety of applications and phenomena.

viscous dissipation occurs, and referred to as the Kolmogorov length scale $\eta$.

Early studies of preferential concentration in turbulence was conducted by Maxey (1987), in which turbulence was simulated using Gaussian random flow fields in the presence of gravity. It was found that particles with inertia produced a bias in trajectory towards regions of high strain rate or low vorticity, which increased the settling velocity. Crowe et al. (1988) studied particle motions in free shear flows, and found that in a variety of particle and flow parameters, the particles can become entrained in the rotating large scale structures and subsequently be centrifuged to the outer edges of the structures. Squires and Eaton (1991) observed the preferential concentration of particles in homoegenous isotropic turbulence using direct numerical simulations for a variety of Stokes numbers, and introduced the phrase preferential concentration. Eaton and Fessler (1994) conducted a comprehensive review of preferential concentration in the limit of low volume fraction and small particle diameter (particle diameters smaller than the Kolmogorov scale) such that particle-particle interaction were rare and the presence of the particle did not affect the fluid phase. They found that across many different studies, the governing parameter for the degree of preferential concentration was the particle Stokes number. The Stokes number is a time scale ratio between the particle response time and the characteristic flow time scale, defined as follows:

$$St \equiv \frac{\tau_p}{\tau_f} \tag{1.1}$$

While selecting the correct flow time scale was not always straightforward in turbulent flows, they found that particle response to vortex motion is most dramatic for Stokes numbers (based on the Kolmogorov time, eddy turnover time, or an integral scale depending on the study) between 0.1 and 1, and this was corroborated in many experimental studies. This implied that particles with time scales on the same order as the fluid time scale responded strongly to particle vortical motions. Lighter particles with $St \ll 1$ tended to follow the fluid trajectories, while particles with $St \gg 1$ could not respond to the fluid motions, both of which did not result in preferential concentration. The work further outlined the basic mechanism for small,

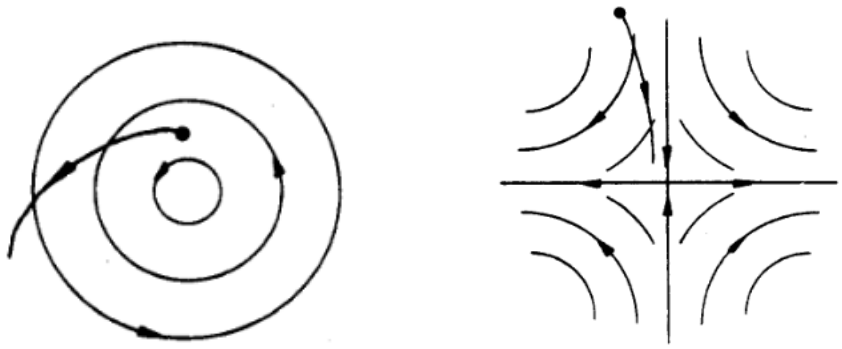

(a) An inertial particle is centrifuged out of a vortical region of the flow (illustration from Eaton and Fessler (1994)).

(b) An inertial particle is entrained into a convergent region of the flow (illustration from Eaton and Fessler (1994)).

Figure 1.2: Schematic description of the centrifugal mechanism for preferential concentration.

dilute, inertial particles to preferentially concentrate: take a simple 2-D vortex, as outlined in 1.2a. Due to the particle inertia, the particles cannot perfectly follow the fluid streamlines and tend to be centrifuged out of vortex cores. Now consider a convergent region of high fluid strain, as shown in 1.2b. A particle crosses streamlines and eventually is likely to settle in the center of the convergent zone . While a real turbulent flow is not stationary nor 2-D as just described, it was found that many experiments and simulations corroborated this idea that particles concentrate in regions of high strain rate and low vorticity when the particle response time is on the order of the turbulence time scale (while the aforementioned limits of small particles and dilute concentration still apply).

A theoretical treatment for a mechanism for preferential concentration was proposed by Maxey (1987) by performing an asymptotic analysis for particles with small inertia. Assuming $St \ll 1$, Stokesian drag, the Lagrangian equation motion for particles can be approximated as:

$$\frac{\mathrm{d}\mathbf{U_p}}{\mathrm{d}t} \approx \mathbf{u_f} - St_\eta \left( \frac{\partial \mathbf{u_f}}{\partial t} + \mathbf{u_f} \cdot \nabla {\mathbf{u_f}}^2 \right) \tag{1.2}$$

Where $\mathbf{U_p}$ is the Lagrangian particle velocity, and $\mathbf{u_f}$ is the local fluid velocity. Using

the Lagrangian particle velocity to define a particle velocity field $\mathbf{u_p}$, and by taking the divergence of the particle velocity field, it was shown that:

$$\nabla \cdot \mathbf{u_p} = -St_\eta \left( \mathbf{S}^2 - \mathbf{\Omega}^2 \right) \tag{1.3}$$

Where $\mathbf{S}$ is the strain rate tensor, and $\mathbf{\Omega}$ is the rotation rate tensor. This relation shows that the divergence of the particle velocity field is positive in regions of high vorticity and low strain rate, and negative in regions where the strain rate dominates, resulting in preferential concentration. Works as recent as that by Esmaily-Moghadam and Mani (2016) show that the contraction rate of the particle velocity field as defined above agree well with direct numerical simulations of particles in homogeneous isotropic turbulence for small Stokes numbers, but fails to predict the expansion of particle clouds at higher Stokes numbers.

The centrifuging mechanism described thus far has been limited to cases where the particle response time was smaller than the dissipative time scales of turbulence. However, a characteristic of higher Reynolds number turbulent flows is the presence of self-similar multi-scale eddies in the inertial range of turbulence, between the dissipative and the energy-containing integral scales. Yoshimoto and Goto (2007) found through DNS of homogeneous isotropic turbulence (HIT) that preferential concentration of small heavy particles in HIT developed a self-similar multiscale nature when the particle relaxation time is within the inertial time scales of the turbulence. Alternatively stated, when the particle Stokes number was appropriately scaled with an alternative inertial length scale $l$, preferential concentration could be observed when the Stokes number was $\mathcal{O}(1)$, analogous to what was observed in the smaller dissipative scales. The work showed that preferential concentration was not limited to just the dissipative scale, and the centrifugal mechanism is active at larger scales to bring about clustering. By studying acceleration statistics of particles and flow topology in HIT, Bec et al. (2006) found that there is a strong correlation between flow structure and particle preferential concentration, but the correlation is much smaller for larger Stokes numbers. Chen et al. (2006) proposed an alternative mechanism for clustering at scales smaller than the integral scale called the sweep-stick mechanism, which was

further expanded to three-dimensional turbulence by Coleman and Vassilicos (2009). The sweep-stick mechanism posits that particles accumulate or "stick" in zero acceleration stagnation points (while moving away from non-zero acceleration points), and are moved in the flow by the "sweeping" motions of the local fluid velocity, which is valid at both the dissipative and inertial scales. (Bragg et al., 2015), however, argue that there is no need for a separate mechanism for the inertial region. It is pointed out that the sweep-stick mechanism fails in kinematic simulations of turbulence, and rather than proposing an alternative mechanism for the kinematic simulation as done by (Chen et al., 2006), perhaps that the sweep-stick mechanism is not the underlying cause for preferential concentration. It is instead proposed that for any separation $r$ which is less than the integral length scale of the flow, the clustering mechanism for $St_r \ll 1$ is related to the preferential sampling of the coarse-grained fluid velocity gradient tensor at scale $\approx r$, which is associated with centrifuging out of eddies at that scale. When $St_r \geq \mathcal{O}(1)$, a non-local mechanism contributes to the inward drift that generates clustering through the statistical asymmetry of the path history of approaching and separating particle pairs. The sweep-stick mechanism is found to only be valid when $St_r \ll 1$, and since the new proposed mechanism is valid in any spatially correlated velocity field, it is argued to provide the more fundamental explanation.

### 1.2.2 Turbulence modulation in particle-laden flows

In certain flow regimes we can observe what is called turbulence modulation by particles, which refers to the action of the disperse phase actively modifying the carrier phase turbulence. Early studies of turbulent modification were hampered either by lack of computing power or experimental difficulties in measuring turbulent statistics in a particle-laden flow. In experiments, the main difficulty was in making measurements of fluid phase statistics in the presence of particles. Hetsroni and Sokolov (1971), however, did successfully use hot-wire anemometry in the presence of liquid droplets in a axially symmetric free jet. By studying the gas-phase spectra and velocity fluctuations, it was concluded that the presence of the droplet phase caused the

suppression of turbulence in the dissipative range. The introduction of LDV (Laser Doppler Velocimetry) in the 1970s resulted in a large increase in studies of multiphase flows turbulence, and since then studies on turbulence modulation have been conducted in a variety of configurations.

Tsuji et al. (1984) made measurements in a vertical pipe flow laden with solid plastic particles of a variety of sizes using LDV. It was found that larger particles intensified the carrier phase turbulence throughout the pipe section, while small particles reduced it. Both effects of suppression and promotion of turbulence was observed for intermediate sized particles.Varaksin et al. (2000) also studied a vertical pipe configuration with glass particles with a Stokes number based on the integral scale of about 1. The mass loading was varied between 0 to 1.2, and results showed that axial velocity fluctuations were damped with increasing loading, but were enhanced near the pipe wall. Numerous works also examined the problem in a channel configuration. Using a vertical channel with sub-Kolmogorov scale particles, Kulick et al. (1994) found that turbulence was attenuated to varying degrees as mass loading, distance from the wall, and Stokes number were changed. Paris and Eaton (2001) also used a vertical channel with small particles, and found that the particle Reynolds number was an important parameter for turbulence attenuation. Kussin and Sommerfeld (2002) studied a horizontal channel configuration in which in addition to particle size and mass loading, the wall roughness was also varied. The work found that pronounced turbulent attenuation could be present for particles depending on the particle size, and that increasing wall roughness caused a stronger turbulence reduction with increasing mass loading. Both Tsuji et al. (1984) and Kussin and Sommerfeld (2002) both observed turbulent augmentation, which was limited to the center of the pipe/channel and high particle Reynolds number. Sato et al. (1996) studied a particle-laden wall-jet configuration, and found that the streamwise turbulence intensity was strongly attenuated in the free shear region by the addition of particles. This attenuation was attributed to enhanced dissipation caused by the introduction of particles.

Numerous criteria for the enhancement or attenuation of turbulence have been proposed in the literature; (Gore and Crowe, 1989) and (Hetsroni, 1989) summarized the available literature on turbulence modulation at the time and found that the

length scale ratio $d/L$, where $d$ is the particle diameter, and $L$ is the integral length scale, was an important parameter. It was observed that turbulence intensity was generally attenuated for $d/L$ less than approximately 0.1, while the turbulence was enhanced otherwise. The effects are similar to that observed in grid turbulence, where turbulence can be attenuated or enhanced based on the size of the grid. Another proposed parameter is the relative particle Reynolds number; Hetsroni (1989) noted that a low particle Reynolds number could suppress turbulence, while particles with high Reynolds numbers tended to enhance turbulence. (Ferrante and Elghobashi, 2003) studied the effect of Stokes number based on the Kolmogorov time scale on turbulence modulation, and found that for $St_\eta \ll 1$, turbulent kinetic energy (TKE) and viscous dissipation rate were increased, while for $St_\eta \gg 1$, TKE and strain rate decayed faster than in particle-free turbulence. As summarized by Balachandar and Eaton (2010), studies have attempted to combine these different criteria and collapse turblence modulation using new dimensionless parameters. Tanaka and Eaton (2008) compiled turbulence modulation data for pipes and channel flows, and showed that turbulence attenuation occured for $3 \times 10^3 \leq Pa_{St} \leq 10^5$, whereas augmentation was found for $Pa_{St}$ outside this range, where $Pa_{St}$ was defined as follows:

$$Pa_{St} \equiv StRe_L^2 \left(\frac{\eta}{L}\right)^3 \tag{1.4}$$

Poelma et al. (2007) posited that particle effects on turbulence are proportional to the product of the number density and particle time constant non-dimensionalized by the Kolmogorov scales, calling this parameter the Stokes load:

$$\Phi_{St} \equiv \frac{\Phi_{nu}\rho_p\eta^3}{3\pi\nu d\tau_\eta} \tag{1.5}$$

Based on these studies, as organized by Crowe et al. (2011) the effects of various parameters can be summarized as following: surface effects (particle size normalized by a length scale), loading effects (mass or volume fraction), inertial effects (particle Reynolds number), response effects (particle Stokes number), and interaction effects (wall roughness or particle collisions). As for the mechanism behind turbulence modulation, Balachandar and Eaton (2010) summarize the various mechanisms

for attenuation and enhancement succinctly: for attenuation, the enhanced inertia of the particle-laden flow, increased dissipation arising from particle drag, and enhanced viscosity of the particle-laden fluid are found to be contributing mechanisms. For enhancement, enhanced velocity fluctuation due to wake dynamics and self-induced vortex shedding, and buoyancy induced instabilities due to density variation arising from preferential particle concentration were listed as possible contributing mechanisms. Since the publication of this review, various works have expanded on understanding turbulence modulation. On the modelling front, (Meyer, 2012) proposed a two-part model: the first sub-model was a Lagrangian particle phase model that could be used to calculate the extra dissipation effects acting on the fluid phase, and the second sub-model reproduced anisotropic dissipation effects of the Reynolds stresses that originate from a mean relative velocity between the phases. Researchers have also revisited the previously examined parameters and their effect on turbulence modulation; (Lucci et al., 2011) found that Stokes number was not a good indicator of turbulence modulation for relatively large Taylor-microscale-sized particles. Numerous works have also investigated effects of new parameters on turbulence modulation, such as compressibility (Dai et al., 2017) and particle sphericity (Ardekani and Brandt, 2019). The consensus, however, seems to be that the mechanisms behind turbulence modulation by particles is still not fully understood, and there is no general model that can reliably predict turbulence modulation.

### 1.2.3 Heat transfer and radiation transport in particle-laden flows

When radiation is incident on a single particle, some fraction is absorbed, scattered, and transmitted. Radiation transport around a single particle can be solved by returning to first principles and numerically solving Maxwell's equations. The most commonly used solution for this problem employs Mie theory for homogeneous spheres; however, limiting cases can be identified based on the particle size parameter $x \equiv \pi d/\lambda$, (where $d$ is the particle diameter and $\lambda$ is the wavelength of incident light), and the complex index of refraction $\tilde{n}$ (Baillis and Sacadura, 2000). Regimes

where $x \ll 1$ is referred to as Rayleigh scattering, while regimes where $x \gg 1$ are called geometric optics and diffraction theory. When considering a disperse medium with a large number of particles, an additional parameter to consider is the particle volume fraction, as this mostly determines whether the medium is in the independent scattering regime. Independent scattering can be described by a regime in which particles are located in the far-field zones of each other, and light interacts independent of neighbouring particles. Practical solutions of radiation transport through disperse media employ a solution of the radiative transfer (RT) equation, a differo-integral transport equation that describes the radiation intensity $I$ propagating along a particular direction $\hat{\Omega}$:

$$\frac{dI}{ds}(\hat{\Omega}) = -(\sigma_s + \sigma_a)I(\hat{\Omega}) + \sigma_a I_b + \frac{\sigma_s}{4\pi}\int_{4\pi} I(\hat{\Omega})P(\hat{\Omega}' \rightarrow \hat{\Omega})d\Omega' \tag{1.6}$$

Where $\sigma_s$ and $\sigma_a$ refer to the particle scattering and absorption efficiencies, and $P$ is the scattering phase function. When the RT equation is applied to particle-laden flows, the carrier phase is assumed to be non-participating, and other relevant parameters such as scattering/absorption efficiencies and the phase function are obtained from Mie scattering solutions for the particular material of the disperse phase. Solving the RT equation generally falls into two families of approaches: the first approach is based on a continuous formulation of the RT equation, in which the medium is treated as a pseudo-continuous medium and the RTE is written in its classical continuous formulation. The other family of approaches is based on a discrete formulation of the RT equation, which often leads to Monte Carlo ray tracing methods (Baillis and Sacadura, 2000).

The RT equation can be further simplified if we neglect the scattering of light into the beam path and blackbody emission, whose solution then becomes the classical Beer-Lambert law, with exponential extinction of light. An important assumption made in the derivation of the Beer-Lambert law is the random, spatially uncorrelated distribution of the disperse medium. Particles in stochastic, correlated media such as those resulting from preferentially concentrated particles in turbulence are spatially correlated, and deviations from the Beer-Lambert law have been theorized

and observed in the literature. Kostinski (2001) adopted a stochastic approach to exponential extinction, and showed that when a dilute random medium is statistically homogeneous but spatially correlated, the attenuation of incoherent radiation with depth is often slower than exponential. This is theorized to occur because spatial correlations among obstacles of the medium spread out the probability distribution of photon extinction events. Using a Monte-Carlo approach Shaw et al. (2002) expanded on this line of thought to show that when the volume-averaged pair correlation function is negative, super-exponential extinction with propagation distance occurs. Frankel et al. (2017) pointed out that posing the radiation transmission through a preferentially concentrated medium through ensemble-averaging the transmission results in a closure problem for the extinction field-transmission correlation $\langle \sigma' I' \rangle$. A closure model was then proposed based on the particle radial distribution function to capture the effect of turbulent fluctuations in the concentration on radiation intensity. These works demonstrate that turbulent fluctuations in number density caused by preferential concentration of particles can alter the absorption and transmission laws of radiation.

The works mentioned thus far have been limited to issues of radiation transport in a stochastic medium, and have not considered the effects of radiative heating on the disperse and carrier phase through convective heat transfer from the absorbing disperse phase to the optically transparent carrier phase. Zamansky et al. (2014) used direct numerical simulations to study initially stationary particles and quiescent fluid subject to an incident radiative flux. The study found that non-uniformities of the disperse and carrier phase resulted in inhomgeneous heat absorption and spatial temperature variations. As the fluid motions were induced by local gas expansion and buoyancy, the resulting baroclinic vorticity production led to higher non-uniformities in the medium, leading back to further non-uniformities in the heat absorption. This created a feedback loop that could trigger and maintain turbulence. Further work by Zamansky et al. (2016) further expanded on the previous work and identified various regimes depending on particle inertia. For small particle inertia, the behaviour of the system is governed by many thermal plumes generated independently from each other, while for large particle inertia, clusters of particles are observed and their

dynamics control the flow. Pouransari and Mani (2017) studied a slightly different system in which heated particles were placed in decaying homogeneous isotropic turbulence over a wide range of Stokes numbers. Applying a high-fidelity framework to perform a spectral analysis of kinetic energy in a variable-density fluid, the study found that particle heating can have a significant effect on the turbulence cascade. For low levels of particle heating intensity, turbulence modification occurred primarily in the dilatational modes of the velocity field. However, as heating levels increased, the energy was converted from dilational modes to divergence-free modes. While works that study cases in which a particle-laden flow is forced by heating at large scales are numerous (see Oresta and Prosperetti (2013), Zonta et al. (2008), or Gotoh et al. (2004)), studies in which the particles provide the heating are relatively sparse. Based on the above studies, an experimental study of preferentially concentrated heated particles is lacking in the literature, and would be a suitable area for further exploration.

### 1.2.4 Turbulent square duct flows and square jets

A turbulent square duct flow is a pressure driven flow through a square-cross sectioned duct. While maintaining some similarities to its sister configuration channel flow, the most notable difference is the three-dimensionality of the flow due to the confinement of the side walls not present in a channel flow. First observed by Nikuradse (1926), the defining feature of the turbulent square duct flow are secondary mean velocity components which develop in the corners of the duct. It was found that large-scale secondary motions in the corners have a significant effect on the mean velocity contours throughout the cross-section. Experiments by Brundrett and Baines (1964) observed the distortion of isovelocity contours of the mean streamwise velocity and the presence of weak longitudinal vortices symmetric about the corner bisector. These vortices acted to entrain fluid towards the corner along the corner bisector, which then turned to move away from the corner parallel to the wall, and finally turned to move parallel to the wall bisector towards the center of the duct. The effect of increasing the bulk Reynolds number was also discussed, and was found to move the secondary

flow towards the corners. Gessner (1973) experimentally evaluated terms of an energy and vorticity balance applied to the mean motion along a corner bisector to analyze the production mechanism of these secondary vortices. The study found that the secondary flows were initiated and directed towards the corner as a result of turbulent shear stress gradients normal to the corner bisector, while the anisotropy of turbulent normal stresses did not play a major role. This implied that anisotropic turbulence models were necessary to correctly capture these secondary flows, and a later work by Launder and Ying (1973) indeed verified that isotropic Reynolds Averaged Navier-Stokes (RANS) models cannot produce these corner vortices. Gavrilakis (1992) used a direct numerical simulation of a fully developed square duct at $Re_\tau = 300$ and confirmed the presence of counter-rotating pairs mirrored across the corner bisector, but also noted the existence of a smaller and much weaker pair situated about the wall bisectors. Despite the presence of these secondary flows, the work also noted that along the wall bisector similarities with plane channel flow could be noted. Vinuesa et al. (2014) performed direct numerical simulations of channel flows with various aspect ratios and Reynolds numbers (including the square duct configuration) and noted that when normalized by the local friction velocity, the mean streamwise velocity profile showed good agreement with the log law. Coherent vortical structures were also compared between channel flows and square duct flows; using the $Q$ criterion to define coherent vortical structures, the work found that coherent vortices are much more elongated than the equivalent structures found in turbulent channels, and the forest of structures were much less densely populated.

Square jets, while not as commonly studied as square ducts, still have relevance in applications such ink-jet printing. The streamwise development of square jets (and most non-axisymmetric jets) can be broken down into three regions in the axial direction, as described in Sforza et al. (1966): the potential core region, in which the effect of mixing has not permeated the entire flowfield; the characteristic decay region, where axial velocity decay is dependent upon orifice configuration, and velocity profiles in the plane of the minor axis are found to be similar, wheras those in the plane of the major axis are not similar; and finally the axisymmetric type decay region, where the entire flow is found to approach axisymmetry. A notable feature of

square jets is the enhanced mixing of the ambient fluid relative to round jets near the jet nozzle. This can be attributed to higher values of Reynolds normal and primary shear stresses in the square jet compared to those found in a round jet Quinn (1992). The controlling mechanism behind this enhanced mixing, however, is agreed to be due to the dynamics of large scale, coherent vortical structures. Due to Biot-Savart self-induction, portions of the initial vortex ring with small radius of curvature (at the vertices of the square) will move downstream faster than the rest, leading to their deformation. As the vortex convects downstream, the deformations yield a complex structure of hairpin vortices and vortex rings (Gutmark and Grinstein (1999), Grinstein and DeVore (1992)). As a result of this complex self-induction and evolution of the jet cross-section, it has been observed that the cross-section can evolve through shapes similar to those of the jet nozzle but with axes successively rotated at angles characteristic of the jet geometry. This is known as the axis-switching phenomenon. Further downstream, vortex interactions and azimuthal instabilities lead to more contorted vortices, to their breakdown, and to a more disorganized flow regime characterized by small scale, elongated vortex tubes (Grinstein and DeVore, 1992). The eventual redistribution of energy between azimuthal and streamwise vortices and their subsequent interaction increases the small-scale content of the jet (Gutmark and Grinstein, 1999).

### 1.2.5 Precursor studies

The present work follows from studies performed by Banko (2018), which had a very similar focus to the present work. Much of the duct flow facility and radiative heating source used in this work was set up by Andrew Banko and postdoctoral fellow Laura Villafane. Initial characterization of the turbulence and preferential concentration in the duct configuration was performed prior to the author's participation in this study, and is described in Banko (2018). Banko (2018) developed a reduced order, quasi-1D model to describe the thermal energy transport in a particle-laden duct flow subject to radiation, and analyzed the radiation transmission in a preferentially concentrated medium by stochastic modelling of the instantaneous particle number density field

(Banko et al., 2019). Measurement of radiation transmission, temperature, and particle phase statistics in the presence of radiation in the duct flow configuration was performed by Banko, Villafane, and the author of the present work, and is detailed in Banko (2018), Banko (2020), and the present work. A critical finding of the previous work and a parallel computational effort (Esmaily et al., 2020) was that turbophoresis (Reeks, 1983) produces a strong increase in the particle concentration near the wall. However, particle collisions within the high concentration layer significantly suppresses turbophoresis, even when the volume loadings are well below levels where collisions typically are ignored.

## 1.3 Objectives

Broadly, the chief objective of this work is to study the coupling between radiation, inertial particles, and turbulence. The work will not study in detail the relatively well-explored interactions of particles in turbulence, but will rather focus on interactions between radiation and the disperse particle phase, and the interactions between the radiation and carrier phase through the particle phase. Review of the literature shows that the effect of disperse point sources of heat on turbulence is not well studied, especially through experiments. The specific goals of the present work at the outset were to extend the precursor studies to provide more comprehensive understanding and documentation of the radiation environment, to extend the measurements in the square channel flow to higher mass loadings and radiation intensities, and to develop and apply measurement techniques to detect changes in the particle concentration and velocity distributions attributable to three-way radiation/turbulence/particle motion coupling. The working hypothesis at the outset was that order of magnitude increases in the radiation-driven temperature rise were achievable, and that the temperature fluctuations associated with particle preferential concentrations might produce changes to the flow structure that would be observable in the particle concentration field.

The goals were not realizable in the original apparatus due to the heating limitations imposed by the square duct configuration. The original apparatus used a single,

monolithic piece of borosilicate glass in the radiated section, and the accumulation of particles on the duct wall in the presence of radiation caused significant local heating and stress to the glass walls, resulting in breakage. The maximum allowable radiation in the duct configuration did not have sufficient heating and temperature rise for any observable turbulence modulation effects by the heated particles to occur. After numerous failed efforts in attempting to reduce the particle accumulation on the duct walls, a change in the flow configuration was proposed. In order to keep the flow as similar as possible to the duct flow without the particles accumulating on the walls, a co-flowing jet configuration was developed in which the glass duct test section was removed so that the square duct flow discharged as a jet into a larger glass test section. The goal here was to examine the evolution of the particle-laden turbulence under intense radiation so jet instabilities had to be suppressed as much as possible. This was partially accomplished by adding a tapered trailing edge to the square duct and more importantly by establishing a co-flow around the jet matching the jet's bulk velocity. With the flow configuration changes in mind, the following objectives are proposed:

- Characterize the unladen, unheated flow statistics in the duct flow and co-flowing square jet, and compare these results to what is expected from literature.
- Characterize the preferential concentration in the duct flow and co-flowing square jet using measures commonly used in the literature to describe preferential concentration, in the absence of radiation.
- Experimentally examine effects of preferential concentration on radiation transmission, and compare these results to what is proposed in the literature.
- Through temperature measurements in the presence of radiative heating, examine the effects of mass loading on the temperature statistics, and how preferential concentration can affect the transport of thermal energy.
- Through measurements of temperature and preferential concentration in the presence of radiative heating, examine any effects of radiation on preferential concentration statistics or turbulence statistics.

- Propose a mechanism for the aforementioned changes in preferential concentration and turbulence statistics caused by the radiative heating.

# Chapter 2

# Experimental Setup

## 2.1 Wind tunnel facility

The facility used in this work can be broken down into four parts: the particle seeding/conditioning section, the development section, the test section, and the particle reclamation section. The facility is designed such that a fully developed, turbulent, particle-laden duct flow can be delivered to two different test section configurations, where radiative heating is applied to the air-particle mixture. Various components of the facility were designed and built by multiple generations of researchers, but much of the initial design was done by Banko (2018) and postdoctoral fellow Laura Villafane, prior to the present author's involvement in the research project. Figure 2.1 provides an overview of the main components of the wind tunnel.

### 2.1.1 Flow conditioning and development section

The flow conditioning and particle seeding section introduces the particles and air into the wind tunnel. The wind tunnel configuration is vertical to prevent gravitational effects on the flow and particles in the wall-normal direction. The seeding section is positioned on a platform two stories above the lab space where the test section is situated. Ambient air in the lab space is drawn into the wind tunnel past a venturi

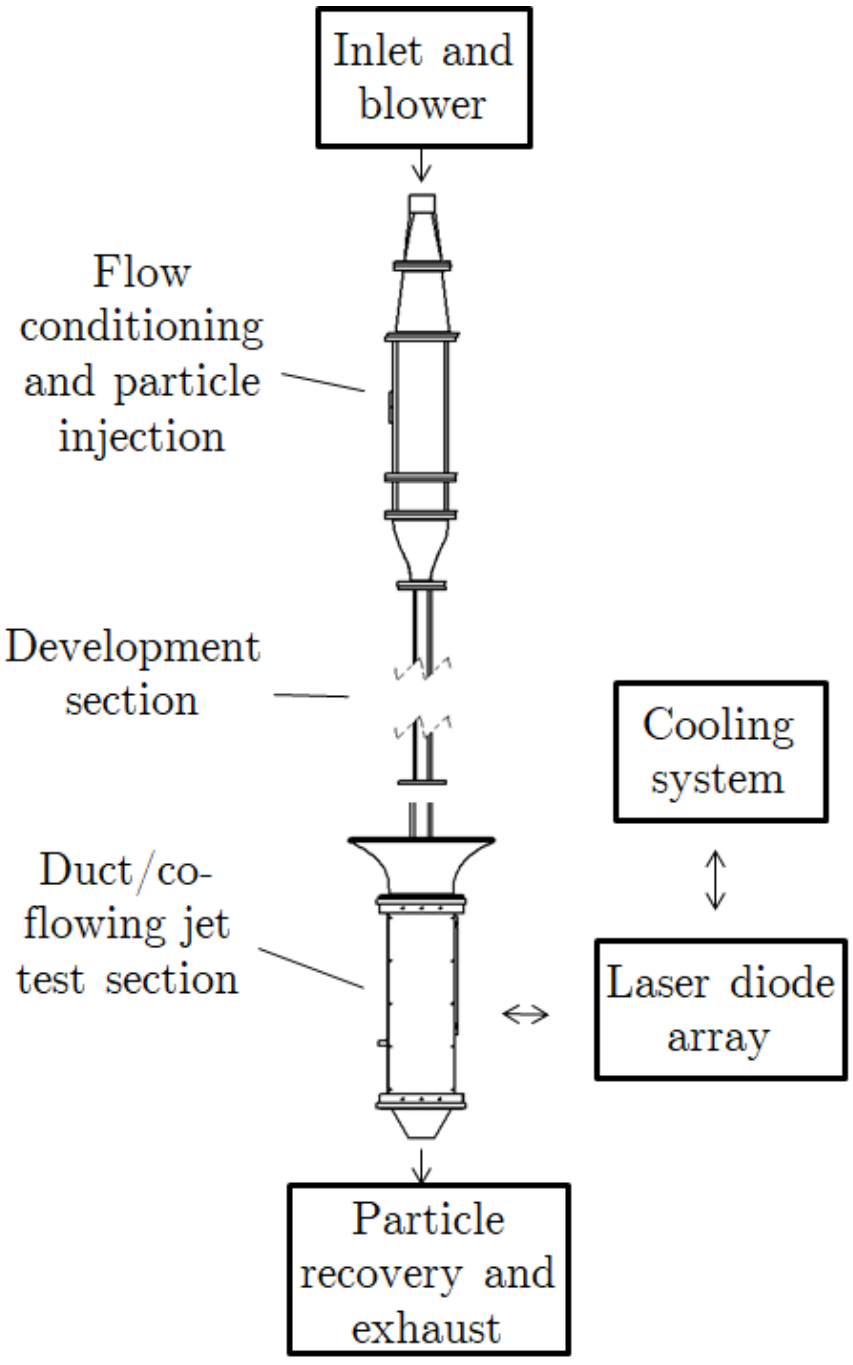


Figure 2.1: Overview of key components of experimental facility used in the present work.

and filter box using a model 2204 New York Blower. The blower is driven via a belt drive by a 5 hp Ajusto Speed motor from Eaton Dynamatic, which is controlled with an Eaton Dynamatic Model 400 speed controller on the lab level. The control signal for the speed controller is generated using a LabView program developed by Banko (2018). The blower and motor are placed on vibration damping feet to reduce vibrations being transmitted to the seeding and development section via the platform. From the blower the air then passes through 4 inch piping, which then forks as shown in Figure 2.2. One of the forks exhausts to atmosphere, while the other fork continues on towards the wind tunnel. This is necessary for stable operation of the wind tunnel. The piping then transitions to approximately 40 inches of 2 inch diameter straight pipe, which leads to a 1.45 in diameter bore Dywer orifice flow meter. In accordance with the ISO 5167 standard, 20 diameters of straight pipe precede the orifice plate, and 10 diameters of straight pipe are downstream. The differential pressure between the upstream and downstream taps of the orifice flow meter is measured using a Setra model 239 pressure transducer, which has a range of 5 in of water ($\pm$2.5 in). The pressure between the upstream tap and atmosphere is measured using Setra model 264 pressure transducer, which can measure up to 50 in of water. The voltage signals from the transducers are sent downstairs and used as inputs for the LabView program that controls the blower. The temperature of the flow through the orifice flow meter is monitored using a K-type thermocouple, which is also used as input for the blower control. This temperature is always checked during the initial blower startup, and varies less than a degree Celsius once the wind tunnel reaches steady state. The actual value of the temperature from day-to-day varies depending on the ambient temperature. Once the flow passes through the orifice meter, it passes through more piping, a diaphragm valve, and a few bends before finally reaching the seeding and conditioning section.

The flow conditioning section's purpose is to prepare the flow for entering the wind tunnel by removing secondary flows, and also to accommodate the particle injection into the system. A cross-sectional view of the the section is shown in Figure 2.3. The section is constructed by using 3-D printed parts made by stereolithography at the University of Texas' at El Paso's W.M Keck Center. The section starts with a square

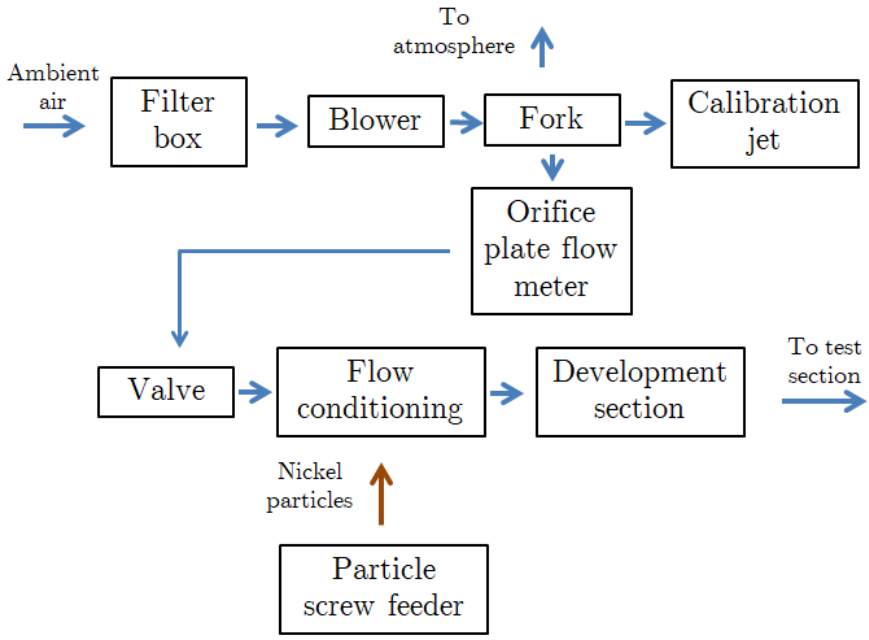


Figure 2.2: Overview of the inlet and flow conditioning sections.

cross-section diffuser that expands at a half-angle of 7.2 degrees, then levels out at a 160 mm x 160 mm cross section. Five grids are spread evenly along the diffuser to eliminate pressure rise and flow separation, thereby promoting flow uniformity. The next section is a straight 160 mm square duct, which has an opening to accommodate the nozzle of the screw feeder at its half-way point on one side of its walls. Following the particle-feeding section, two more grids act to further condition the flow, and the final contraction section accelerates the flow again. The contraction profile is a fifth order polynomial fit to have zero slope and curvature at the ends, and is 1.51 times as long as the inlet cross-sectional dimension in order to produce a top hat velocity profile. A thermocouple was placed in this section to monitor the temperature of the flow, and a small tube was set up to connect this section and the screw feeder hopper in order to equalize the pressure between the two chambers. The screw feeder is described in more detail in the following section.

The development section follows after the conditioning section, which is constructed using 1/2 in thick cast and precision ground aluminum side walls. The development cross section is 40 mm x 40 mm, and matches that of the test section

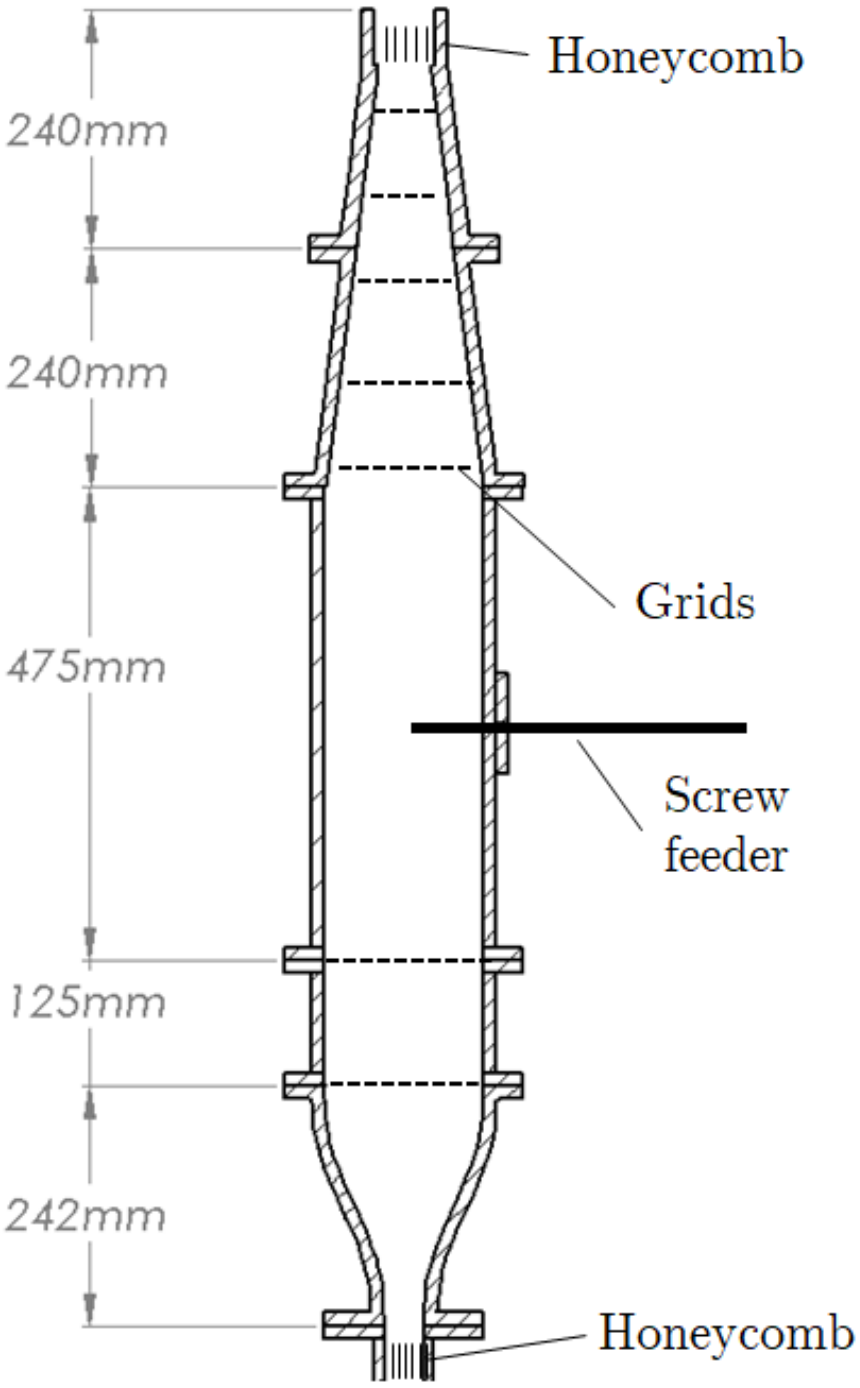


Figure 2.3: Cut-out view of the flow conditioning and particle feeding section.

(except for the rounded corners in the duct flow configuration). It is 5.48m long, which corresponds to a streamwise length of 137 channel widths; this is a sufficient distance for the particle concentration distribution to become fully-developed (Lau and Nathan, 2014). The full section is built by assembling three separate sections, joined by flanges and sealed using high-temperature carbon gaskets. Each individual section is assembled by screwing the side walls together and sealing the wall with high-temperature epoxy. Support for the section is provided by an intermediate Unistrut frame that was attached to an I-beam at the ceiling level of the ground floor. Pressure taps are installed at various locations along the development section: two taps are drilled for the two upstream sections at 1.2 m intervals, and five taps are drilled in the third (downstream) section at 0.3 m intervals. The pressure is acquired using a Scanivalve multiplexer, but these pressure measurements are not part of the present work. Further details of the measurement can be found in Banko (2018). The development section is also grounded at various intervals to counter the accumulation of static charge from collisions from the particles.

### 2.1.2 Particle feeding, particle reclamation, and particle properties

The particles must be introduced into the wind tunnel in a reproducible and controlled manner; to that end, a screw particle feeder is employed. The feeder is an Accu-rate model 302 volumetric screw feeder. The feeder is composed of hopper section which can hold up to 10 kg of particles, and a screw section that collects the particles from the bottom of the hopper and transfers them into the flow conditioning section. The hopper section holds up to 10 kg of particles, allowing for continuous feeding at the highest feed rate for about 10 minutes. The screw used for the experiments is a 1/2 inch helix screw, for mass loadings from $\Phi_m = 0.1-0.4$, and a 9/8 inch helix screw, for mass loadings from $\Phi_m = 0.4-1$. The screws are enclosed by a long hollow aluminum sheath which serves to contain the particles while they are transferred from the feeder to the conditioning section. The aluminum sheath has an opening near the end on its side-wall, where the particles exited the sheath into the conditioning section. To

mitigate pulsatile feeding from the screw feeder, much of the machined opening in the sheath is covered. This resulted in more compacted particles in the sheath, producing a smoother feed. The amount the opening was covered has to be carefully tuned; if it is too low the feed will pulse, while if the amount covered is too high the sheath cannot be held in place and will burst off the feeder. The feeder itself is placed on a translating base, which allows the screw/sheath section of the feeder to be slid in and out of the conditioning section. This is necessary when calibrating the feeder or switching out the screw for a different size. The translating base can be lowered onto a scale (Mettler Toledo PBA655-B60) placed under the base, which allows an in-situ measurement of the weight of feeder and the particles within. The power supply to the feeder is set up such that the feeder can be turned on and off from the ground level, which is necessary for a possible emergency shut-off. The feed rate, however, has to be set manually from the platform.

The feed rate of the feeder is calibrated by running the feeder at the ranges used in experiments over a one-minute interval, and using a scale to measure the total output over that interval. The calibration is found to be linear for the ranges used in the experiment, with a small offset due to the start-up torque required to start turning the screw. To ensure that the feed rate during the open-to-atmosphere calibration matches that of the pressurized state during experiments, Banko (2018) performed a test in which the feeder was run at test conditions. The weight of the feeder and particles in the feeder were measured using the Mettler Toledo scale under the feeder before and after feeding, and the feed rate was found to match that of the calibration done at atmospheric pressure to within measurement uncertainty.

Once the particles pass through the development section and the test section, they must be separated from the air to be recycled. To achieve this, a combination of a cyclone separator and an auxiliary blower are used. A New York Blower compact GI fan on the ground floor preceded by a filter box supplies dilution air at approximately $1.4 \times 10^{-1} m^3/s$. The air supplied by the blower is fed into a muffler to reduce potential perturbations to the main flow, then enters 4 inch diameter PVC pipe. Meanwhile the main flow, once past the test section, enters vertical metal piping whose configuration differed based on the test section configurations. The details of

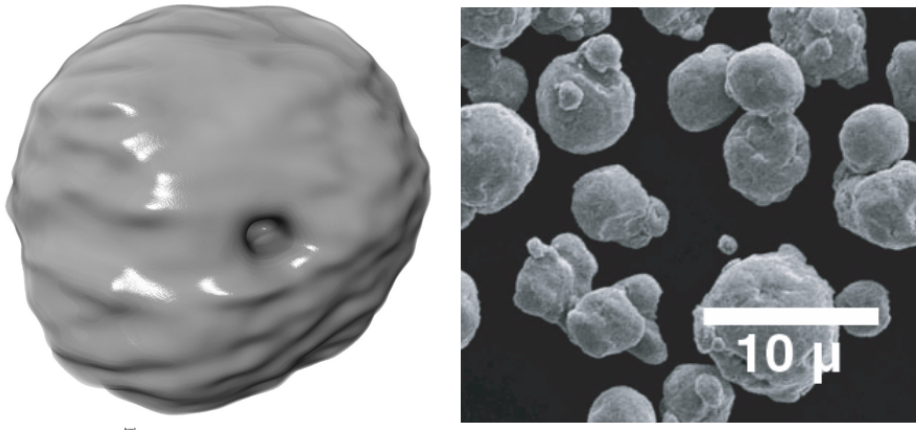


Figure 2.4: Scanning electron microscope (SEM) images of the nickel particles used in the present work.

each configuration after the test section are described in Section 2.1.3 and Section 2.1.4. Both configurations eventually turn vertical and enter a cyclone separator used by Benson and Eaton (2003). Particles fall out through the bottom of the separator and are collected in a sealed bucket, while the air is exhausted outside the facility. A fraction of particles are lost with each experiment, varying from less than 3 percent to up to as high as 10 percent, depending on the test section configuration; the co-flowing jet configuration tended to lose more particles than the duct configuration.

The particles used for the experiment were chosen by Banko (2018) to satisfy various competing criteria. The Kolomogrov Stokes number should be in the range $\mathcal{O}(1) - \mathcal{O}(10)$ such that the particles preferentially concentrate in the turbulent flow. The (mass) density of the particles should be high enough such that mass fractions of $\mathcal{O}(1)$ could be achieved, while the volume fraction remains lower than $10^{-4}$ such that the bulk of the flow is not collision-dominated. The thermal Stokes number is chosen to be $\mathcal{O}(1)$, as this results in the particles strongly interacting with temperature fluctuations in the carrier phase turbulence. The particles also must be strongly absorb near-infrared radiation. With these criteria in mind, Nickel particles from Novamet were chosen. These particles are nearly spherical, as demonstrated by SEM images shown in Figure 2.4, and also polydisperse. The key material properties of the particles are shown in Table 2.1.

| Property | Value |
|---|---|
| Density $\rho_p$ | 8908 kg/m$^3$ |
| Specific heat capacity (isobaric) $c_{p,p}$ | 450 J/kg K |
| Complex index of refraction ($\lambda = 975$) $n + ik$ | $2.78 + i5.02$ |
| Complex index of refraction ($\lambda = 635$) $n + ik$ | $1.99 + i4.11$ |

Table 2.1: Table of material properties of nickel particles.

The size distribution of the particles is characterized using a Beckman Z2 Coulter counter. Coulter counters measure particles volumes by passing particles suspended in an electrolytic solution through a small orifice, and measuring changes in current through the orifice. The probability density function (PDF) of the particle diameters are shown in Figure 2.5, assuming spherical particles. Notable statistics are the mean diameter $\langle d_p \rangle = 11.9$ mm and diameter standard deviation of 2.7 mm. A log-normal fit to the distribution is also shown. The polydispersity of particles results in variability for the non-dimensional parameters that depend on the radius of the particles; the most important of which are the particle radius to Kolmogorov scale ratio, the Kolmogorov scale based aerodynamic Stokes number, the thermal Stokes number, and the particle Mie coefficients. The first three parameters strongly determine the how the particles interact with the turbulence, while the Mie coefficients determine the degree of absorption or extinction of radiation as it interacts with a particle. Tabulated in Table 2.2 are the mean values of these non-dimensional parameters. The parameters requiring the Kolmogorov scales were computed for the duct configuration using a cross-sectionally averaged dissipation rate, and the Mie absorption and extinction coefficients $\sigma_a$ and $\sigma_e$ were computed by Banko (2018) using an open source Mie scattering code written by Mätzler (2002).

### 2.1.3 Test section - duct configuration

The duct configuration is one of two flow configurations used in the present work. The duct test section is the simpler of the two configurations, and aims to keep the cross-section as close as possible to the development section. It needs to be as transparent as possible to radiation such that the particles are the dominant absorbing medium in

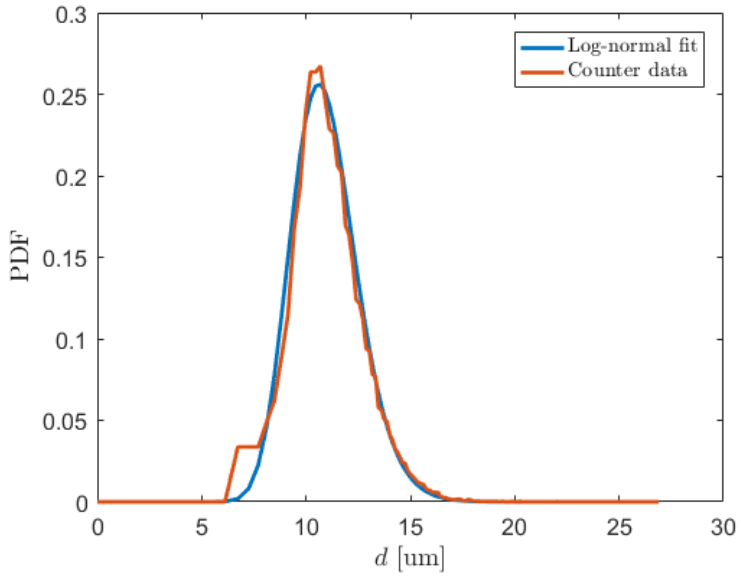


Figure 2.5: Size distribution of the nickel particles used in the work, measured with a Coulter counter.

| Parameter | Variable | Value |
|---|---|---|
| Diameter to Kolmogorov scale ratio | $d_p/\eta$ | 0.17 |
| Aerodynamic Stokes number (based on Kolmogorov scale) | $St_\eta$ | 11.3 |
| Thermal Stokes number | $St_{th}$ | 5.2 |
| Absorption efficiency ($\lambda = 975$) | $Q_{abs}$ | 0.39 |
| Absorption efficiency ($\lambda = 635$) | $Q_{abs}$ | 0.41 |
| Extinction efficiency ($\lambda = 975$) | $Q_{ext}$ | 2.19 |
| Extinction efficiency ($\lambda = 635$) | $Q_{ext}$ | 2.17 |

Table 2.2: Table of particle diameter-dependent non-dimensional parameters. The parameters are computed from cross-sectionally averaged values in the duct, or right at the jet exit for the co-flowing jet.

the experiment, but also must withstand a significant temperature rise and resulting thermal expansion. To that end, a monolithic borosilicate glass section 475 mm long, 2 mm thick, and 40 mm x 40 mm wide is used. Separate sections for each wall are avoided as any method used to join the surfaces are likely to either absorb more radiation, and/or cause additional stresses due to mismatched thermal expansion. Because of the manufacturing process, the corners are rounded with inner radii of 2 mm and outer radii of 5 mm. The actual cross-section area is 0.2% smaller than the square cross section, and the maximum linear dimension mismatch is 0.8 mm along the corner bisector, which is less than 25 viscous units based on the perimeter averaged friction velocity. Spectrometer measurements show that the glass is $91 \pm 0.3\%$ transmissive of radiation at 975 nm wavelength, $7 \pm 0.3\%$ reflective, and $1 \pm 0.6\%$ absorptive.

Aluminum caps are used at the top and bottom end of the test section to secure the glass test section onto the rest of the wind tunnel, and are shown in more detail in Figure 2.6. The caps are adhered to the glass section using high temperature epoxy to accommodate the temperature rise occurring from the radiation absorption. The upstream end is aligned with the rest of the test section using dowel pins, and the downstream section is a sliding joint with some clearance in the streamwise direction to account for thermal expansion. The downstream end is sealed using an o-ring and an aluminum ring, which also serve to further align the test section. The sliding base aluminum joint has an opening to accommodate caps on the side walls of the base to allow the introduction of probes into the wind tunnel after the glass section. The caps are screwed on and off as necessary and sealed during experiments with vacuum grease. The test section design for this configuration was designed with easy removability of the glass section in mind, as particle accumulation necessitated removal of the test section after each particle-laden experiment. The cleaning and preparation of the surfaces before each experiment involves three steps: rinsing the inner and outer surfaces, cleaning with acetone and isopropyl alcohol in conjunction with lint-reducing wipes, and application of an anti-static spray, which is spread throughout the inner surface using a sponge and lint-reducing wipes. Numerous approaches were

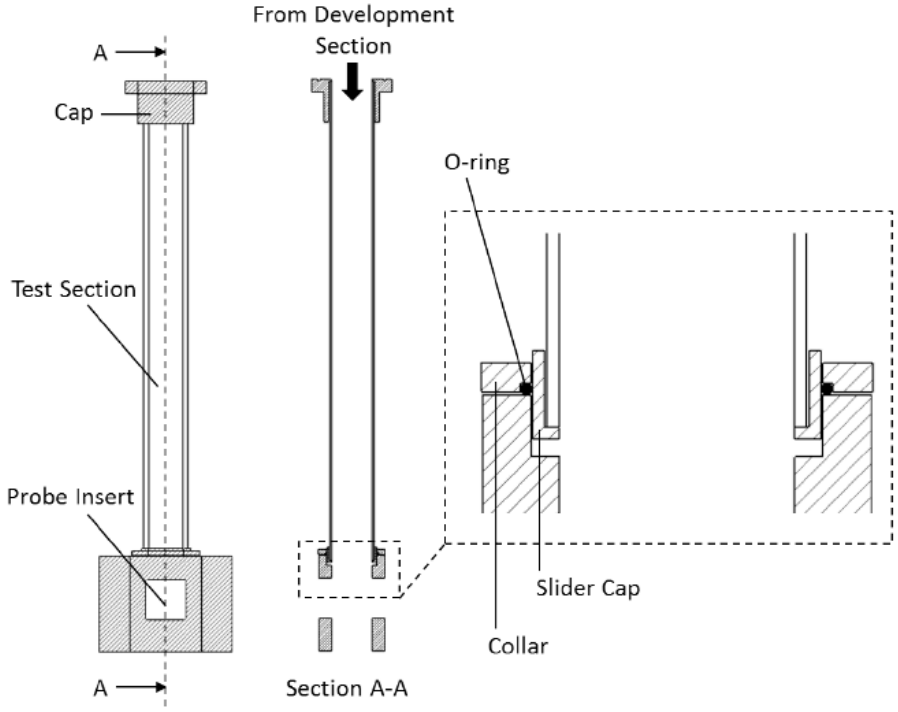


Figure 2.6: Section view of the duct test section and its constituent components. Figure credit to Banko (2018).

tested to attempt to reduce the particle accumulation on the walls, including different cleaning and preparation approaches, and altering the conductivity of the surface using chemical vapor deposition (CVD) of metal films. The aforementioned cleaning approach, while insufficient for high radiative power, still proved to be the most effective, as other coating approaches changed the transmissivity of the radiation through the glass.

Once past the test section, the flow mixes with the dilution flow before entering the cyclone separator as described in Section 2.1.2. This is accomplished by transitioning a flow to a 2-inch diameter metal pipe, which eventually reduces down to a 1-inch diameter pipe. This enters into the t-junction and turns 90 degrees inside the larger 4-inch diameter junction, before exhausting into 4-inch diameter aluminum piping. The flow is configured this way to align its momentum in the new streamwise direction, and eliminate interactions between the dilution flow and the main flow from the

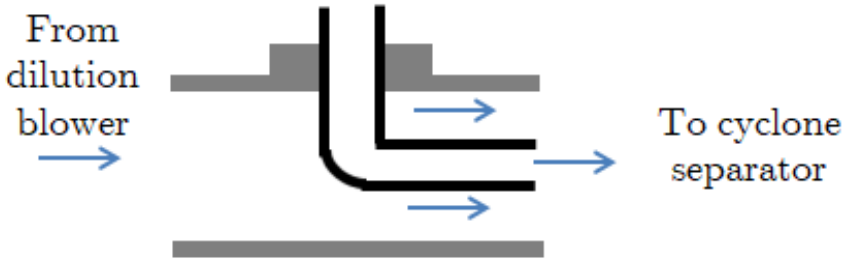


Figure 2.7: Section view of the duct configuration t-junction geometry.

test section. The t-junction is shown in more detail in Figure 2.7. Once past the t-junction, the now-mixed flow from the dilution blower and the main flow travels through 1.8 m of 4 inch diameter aluminum piping, which turns upward for 2.5 m, and turns one final time into the cyclone separator.

### 2.1.4 Test section - co-flowing jet configuration

The co-flowing jet configuration is the second of the two flow configurations used in the present work, and is the result of an attempt to eliminate particle accumulation of the side walls. Particles on the side walls of the glass wall absorb radiation and cause significant local thermal stresses in the glass, which resulted in numerous occurrences of test section breakage. The best compromise, which sacrificed some flow simplicity for radiative power, was the co-flowing jet configuration.

All components upstream of the test section are kept the same, including the particle feeding, flow conditioning, and flow development sections as described in Section 2.1.1 and Section 2.1.2. The first difference occurs at the end of the development section, where the 1/4-inch thick development section walls taper down to a thickness of 1 mm. The dimensions of the inner walls are kept constant with the same cross-section as the development section and duct at 40 mm x 40 mm while the tapering of the outer wall occurs over a length 70 mm. At the end of the tapered section, the duct flow discharges into a larger, 160 mm x 160 mm square duct co-flow. The co-flow is generated by drawing in ambient air through a bell mouth. The bell mouth is 3-D printed using stereolithography at the University of Texas' at El Paso's W.M Keck Center, and its wall curvature is defined using a third order polynomial with

zero slope and curvature at the end of the inner downstream side. Four struts extend at the wall bisectors into the center, which holds up a square frame that centered the bell mouth around the development section. Supporting the bell mouth and test section walls are two horizontal aluminum flanges, which are in turn held in place using 80/20 aluminum struts. The upper flange supports the bell mouth and the upstream end of the test section walls, while the lower flange supports the contraction and the downstream end of the test section walls.

The flow enters the 160 mm x 160 mm square duct section at the bell mouth exit. The walls of this expanded square duct section are constructed using 1/4 inch thick polycarbonate or aluminum, depending on each individual wall's orientation relative to the radiation. The two side walls parallel to the radiation propagation direction are polycarbonate, with dimensions of 558 mm x 185 mm. The walls are transparent for optical access, but are polycarbonate as radiation is not incident in any of these walls. The wall normal to the radiation direction and closer to the radiation source is composed of three components: the aluminum wall, the glass sheet, and the glass clamps. The aluminum wall had dimensions of 558 mm x 148 mm, and has a square hole with dimensions of 285 mm x 105 mm. The hole is centered in the streamwise normal and radiation normal direction, but offset from the center in the streamwise direction by 118 mm. Around the hole on the inner side of the wall is a larger inset 3.2 mm deep and 5.05 mm wide, which is designed to accommodate a 295 mm x 115 mm x 1 mm quartz glass window and an 1.5 mm thick aerogel fabric gasket. The purpose of the thin glass window is to allow radiation to pass through with minimal absorption. The glass window is held down onto the aluminum wall with custom-made aluminum fasteners, leaving the glass window flush with the inner surface. The fasteners themselves, however, extrude into the flow by 1 mm, but were found to have no significant effect on the flow. The fourth and final wall, which is also normal to the radiation direction but further from the radiation source, is composed of two components: the radiation sink and the optical window. The radiation sink is a 1/4 inch thick aluminum sheet measuring 379 mm x 154 mm with the inner surface spray painted flat black. It is placed directly opposite the radiation source. Two Lytron cold plates are bolted on the outside with thermal paste on the interface to transfer

heat out of the plate. Placed directly below the radiation sink is a 1/4 inch 169 mm x 148 mm polycarbonate window, which is attached to the radiation shield via a flange. Depending on the experiment, an identical window with holes for probe mounts is used instead. Since all the aluminum parts experience enough temperature rise at high radiation power to start melting the polycarbonate, custom cut 1/8 inch thick silicone gaskets are placed between all heated aluminum walls and polycarbonate walls for sealing and insulation. The walls and the full assembly are shown in Figure 2.8.

Once past the test section, the flow encounters a square contraction that reduces the 160 mm x 160 mm cross section to 72.3 mm x 72.3 mm over a 80 mm distance. The contraction is made by water-jet cut aluminum sheets that were welded together. A 4 inch diameter aluminum pipe is placed after the contraction with a butterfly valve to control the co-flow flow rate. After the valve the flow encounters a 90 degree bend (instead of the t-junction present in the duct flow) and proceeds through 1.6 m of 4 inch aluminum piping, leading to the same New York blower that was used to drive the dilution flow for the duct configuration. Instead of providing the dilution flow, however, the blower now provides suction for the co-flow. The blower re-directs the flow vertically into the cyclone separator for particle recycling. The differences in the post-test section components are shown schematically in Figure 2.9.

## 2.2 Radiation source and instrumentation

### 2.2.1 Laser diode array

The radiation is supplied to the experiment using a laser diode array from Princeton Optronics. It emits monochromatic radiation at a wavelength of 975±1 nm, with optical powers nominally ranging from 1-10kW. The array is composed of three rows each with twenty-four 4.8 mm x 4.8 mm square emitting chips, with each chip containing thousands of vertical cavity surface emitting diodes. Each cavity emits radiation with a profile close to Gaussian at a full angle divergence of 18°. Each group of three chips is mounted to a microchannel cooler, since the 40% efficient diodes require significant

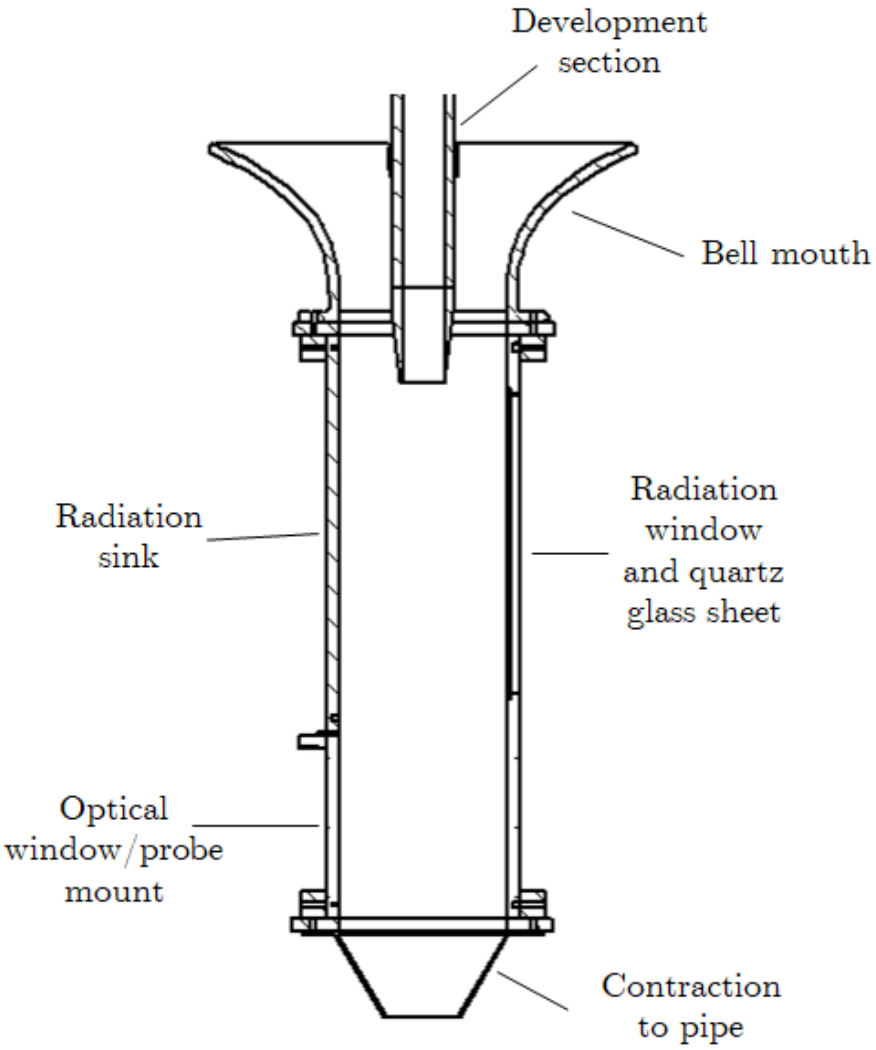


Figure 2.8: Section view of the co-flowing jet configuration.

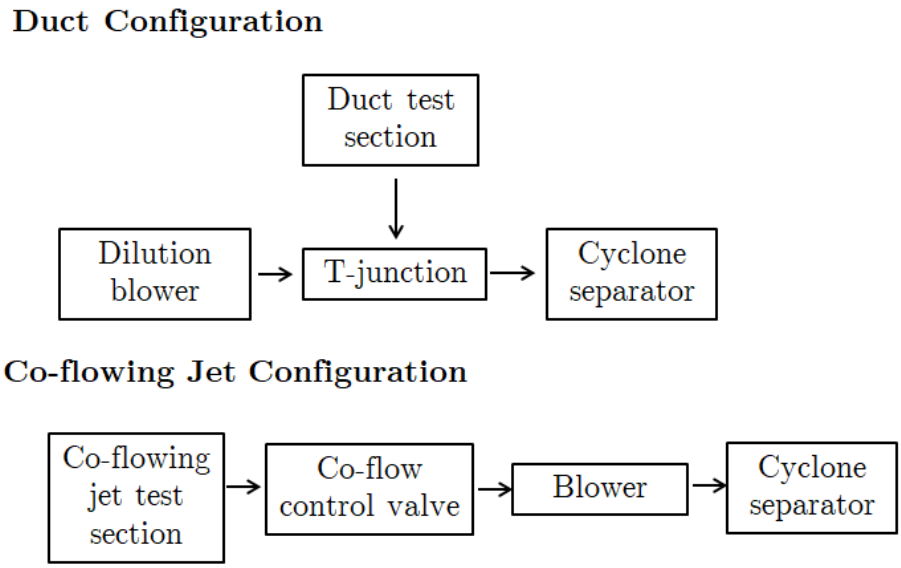


Figure 2.9: Comparison of the components downstream of the test section between the duct and co-flowing jet geometry.

heat rejection. Each chip is separated with 1.9 mm of spacing, while the columns are separated by 10 mm. Each column of diode arrays is powered by a Sorensen SGA200 power supply, which can deliver up to 60A of current to each column. The described chip configuration is shown in Figure 2.10. The chips are protected from dust settling on its surface by being isolated from ambient air with a custom-made polycarbonate case. During diode operation, a blade of dried and filtered air was blown over the chips to further protect the diode surfaces from any particles settling.

The full array is mounted on a copper manifold base which distributes the cooling water to the micro-channel coolers, and the cooling water is supplied by a system of chillers, heat exchangers, and pumps. The cooling water is supplied from a 55 gallon tank of water, which is pumped with a 5 hp Goulds 45HB15013 booster pump. The water passes through a brazed plate heat exchanger and a pair of 5 $\mu m$ filters before entering the copper manifold. The flow rate, pressure drop, and temperature are monitored using a flow meter, pressure gauge, and thermocouple. The chilled water for the heat exchanger is on a separate flow loop, supplied using a Thermoflex TF240B chiller which maintains the tank of water at $7°C$. This chilled water loop

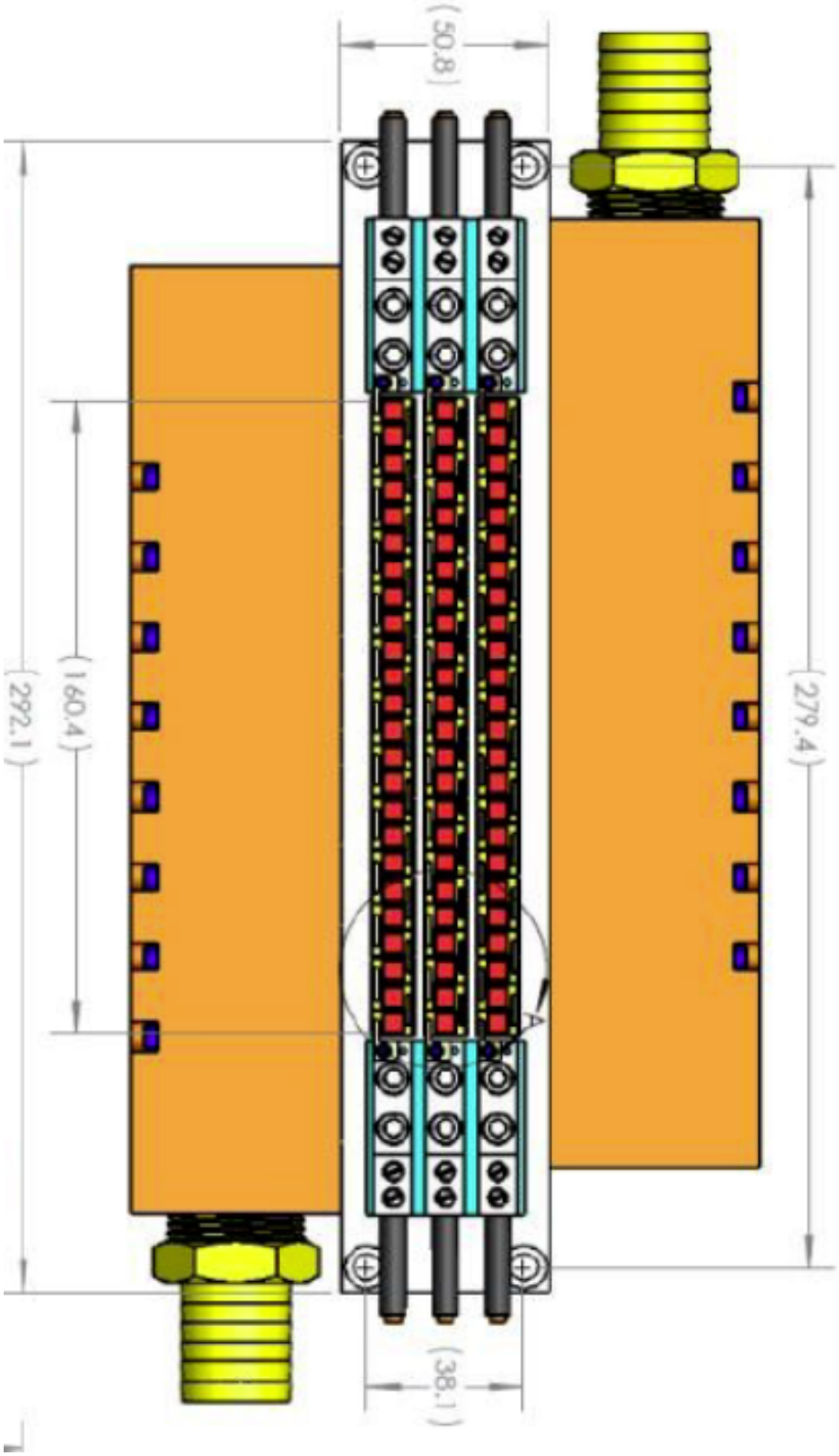


Figure 2.10: Schematic of the laser diode array, showing the configuration of the chips, the columns of microchannel coolers, and the copper block.

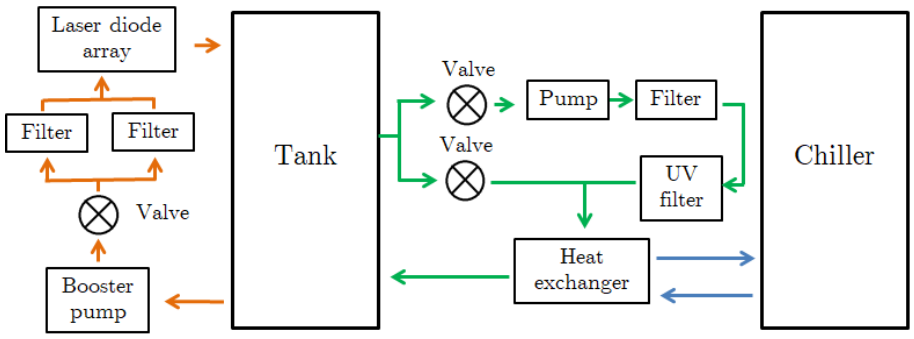


Figure 2.11: Schematic of the flow loop used to cool the laser diode array.

passes through a UV filter and a 5 $\mu$m filter. The tank of water and the heat exchanger are wrapped in fiberglass insulation to improve the cooling efficiency, but even with the insulation the temperature of the cooling water cannot be maintained at $7°C$ at maximum power. At maximum power, the diode array could be powered for about 20 minutes before the drop in cooling efficiency becomes unsafe for the diode array. A schematic of the two flow loops used are shown in Figure 2.11.

The positioning of the laser diode array relative to the test sections is shown in Figure 2.12. In the duct configuration, a shield is placed between the laser diode array and test section to mask some of the radiation. This ensures that all the radiation that propagate past the test section is incident on the water-cooled copper calorimeter (described in the next section). For the co-flowing jet configuration, this shield is not necessary as the radiation sink on the far wall of the duct was designed to capture all radiation from the laser diode array.

### 2.2.2 Copper calorimeter

A copper calorimeter designed by Dr. Chris Elkins is employed to quantify the total power emitted by the laser diode array. The calorimeter is roughly trapezoidal-prism-like in shape, with the smaller lengthwise surfaces painted black to absorb radiation. It is placed normal to the radiation direction, adjacent to the test section for the duct configuration. This allows the calorimeter measurement to be conducted parallel to any other measurement in the duct configuration. For the co-flowing configuration,

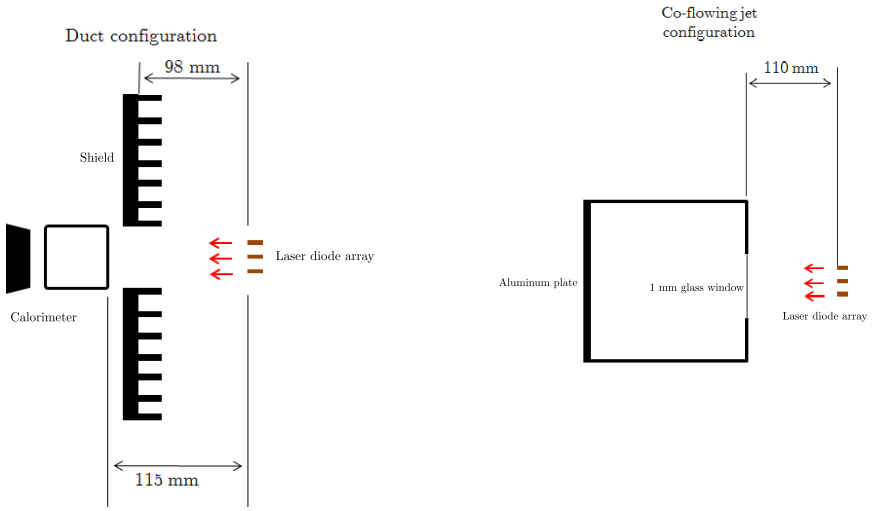


(a) Configuration of the laser diode array relative to the duct test section.

(b) Configuration of the laser diode array relative to the co-flowing jet test section.

Figure 2.12: Configuration of the laser diode array relative to the two flow configurations.

the calorimeter cannot be employed parallel to the experiment due to the presence of the radiation sink wall. Inside the calorimeter are two ribbed serpentine passages through which water flows and convectively absorbs the heat delivered radiatively to the surface of the calorimeter. The ribbed passages are shown in Figure 2.14a. The water is supplied to each passage by building chilled water, and its flow rate is monitored using a Transonic Systems T402 box and a ME8PXL flow probe. The incoming and outlet temperatures of the two channels of water are monitored using thermistors powered by a 5V reference. The thermistor resistance is backed out from its voltage signal, and the temperature is determined using a calibration provided by the thermistor manufacturer. On the rear side of the calorimeter are thermocouples epoxied onto the surface to monitor the surface temperature of the calorimeter, which is important for estimating convective losses to the ambient air.

The uncertainty in the copper calorimeter measurement is obtained through uncertainties in flow rate from the flow meter, the temperature change from the thermistors, and variability in particle accumulation during a run. The uncertainty from the flow

meter calibration is roughly 1% at 5 mL/min with a 500 mL/min flow rate, which is estimated by calibrating against a known flow rate. The uncertainty from the thermistors is estimated to be relatively small, with 0.05° C agreement in isothermal flow, with one thermistor measuring 0.2° C higher. The variability in absolute transmission due to particle accumulation was observed to be as large as 2%, while losses due to convection and blackbody emission were estimated to be much smaller. The resultant estimated uncertainty on the relative transmission was approximately 5%, where the relative transmission is defined as the radiation transmitted through the test section and particles (essentially the radiation incident on the calorimeter), divided by the transmission through the test section without the particles flowing through the system measured *after* the experiment to account for particle accumulation.

### 2.2.3 Calorimeter array

While the copper calorimeter is capable of measuring the total incident radiative power over its entire surface, it cannot make spatially resolved measurements of power or heat flux. To better quantify the spatial profile of the incident radiation, a calorimeter array was designed. The array is composed of 9 separate small copper absorbing elements, embedded in a ceramic base. Each element is 5 mm x 5 mm wide, with 0.5 mm of spacing between elements. Machine-able ceramic (Macor) was used as the base to minimize conduction between them. A 3 mm diameter hole is drilled out in the back of each copper element, where a 20 gage K-type thermocouple is attached with a high thermal conductivity epoxy. The front surface of the copper elements are painted with black high emissivity paint to maximize radiation absorption. Figure 2.14 shows a schematic of the array. To measure the radiative power incident on each element, the temporal response to a step increase in radiative flux is measured. The step increase is achieved by placing a shield in front of the calorimeter array, allowing the radiation output to stabilize, and dropping the shield to expose the elements to radiation. If the radiative power incident on the element is significantly larger than conductive or convective losses, the response (temperature vs time) is initially linear.

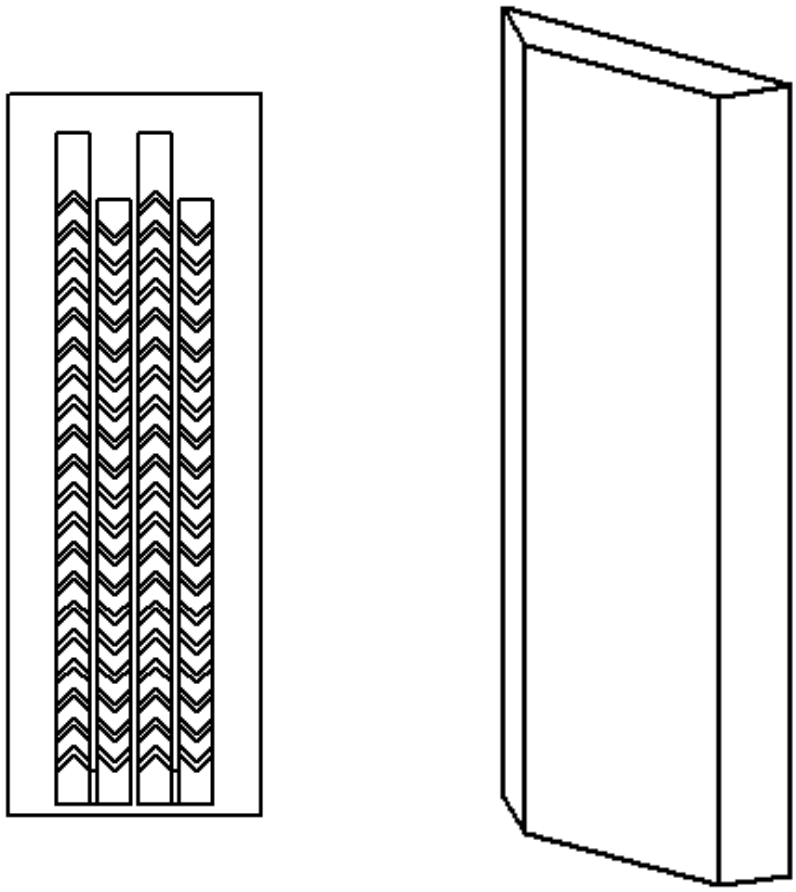

(a) Section view of the calorimeter, showing the ribbed internal passages.

(b) Trimetric view of the calorimeter absorbing surfaces.

Figure 2.13: Schematics of the copper calorimeter used to measure the laser diode array output or transmission.

(a) Frontal view of the calorimeter array. Each copper element is 5 mm x 5 mm, and the base is made from Macor ceramic.

(b) Trimetric view of the calorimeter array.

Figure 2.14: Schematic of the calorimeter array used to measure the spanwise radiative power profile.

This initially linear region is used to back out the relative incident heat flux differences between elements. In order to account for differences in heating response from element to element (due to marginally different boundary conditions, thermocouple contact, etc), a calibration response was obtained using a separate 3W laser where each element was focused on individually. This allowed the measurement of the individual response for a given incident power. During the measurement the calorimeter is placed where the duct wall nearest to the radiation would have been, and is moved to different streamwise locations using a traverse.

The uncertainty in this measurement arises from heat loss from the element due to radiative emission, free convection, and conduction, and uncertainty arising from the fitting. The heat loss due to radiative emission, free convection, and conduction was estimated to be negligible compared to the incident radiation at 1kW and higher powers, and were concluded to not have a notable effect on the temperature response. However, with high enough temperature rise the effect of convective losses became notable as the linear increase starts to level out. Hence each response is manually examined, and the region of linear fit chosen for each response. This is likely the largest source of uncertainty in the measurement, due to the subjective nature of deciding the extent of the linear region. The uncertainty varies depending on the location of the calorimeter element, but can be as large as approximately 15%. More detailed results on the uncertainty can be found in Chapter 3.

### 2.2.4 Photodiode

While the calorimeters are capable of making measurements of mean transmission, they cannot be used for any instantaneous measurements. To study the radiation transport in a random medium, means to measure the instantaneous transmission is critical to obtain higher order statistics of transmission. To that end, a photodiode was used in conjunction with a separate helium-neon (HeNe) laser. The photodiode could not be used to measure the transmission directly from the laser diode array as the sensing area of the photodiode was only a few square millimeters wide, and the rest of the photodiode could not safely be exposed to radiation from the relative large area of incidence of radiation. While the sensor could conceivably be shielded, the shield itself would also need to be cooled, which increased the complexity of the measurement. The compromise was using a separate radiation source instead, which could be focused directly on to the small sensor area, at the cost of the radiation being at a different wavelength and divergence.

The photodiode used for the experiments was a Thorlabs DET36A detector. The sensor had a 14 ns rise time, which was sufficient to resolve the smallest time scales relevant in the experiment. The sensor was paired with a $OD = 6$ band pass filter to attenuate the radiation from the HeNe laser to a suitable level, and to minimize noise from ambient light. The HeNe laser used in conjunction with the photodiode emitted a collimated beam at a wavelength of 632 nm, power of 35 mW, and a radius (as defined by the $1/e^2$ drop-off) of 1.2 mm. This beam was also attenuated immediately upon exiting the laser head with a $OD = 4$ filter, which in conjunction with the band pass filter attached on the photodiode, set the radiative power incident on the sensor area to a suitable level. Due to space constraints in the experiment, the beam and photodiode were oriented such that the beam path was perpendicular to the direction of radiation propagation from the laser diode array, at a streamwise location of 8 mm upstream from the probe location. Due to the rotational symmetry of the flow in all configurations, the transmission statistics were not affected by this rotation. The voltage signal from the photodiode was passed through a Frequency Devices 901 8-pole Butterworth filter, which low-pass filtered the signal at 14 kHz. The signal was

sampled at 30 kHz using a Labview PCI card (PCI-MIO-16E-4) in conjunction with a NI BNC-2090 breakout board. The uncertainty in the photodiode was quite minimal, with contributing sources from electrical noise and day-to-day variation in particle accumulation rate on the side wall. The day-to-day variation was found to be the dominant source of uncertainty, contributing to about 3% variation in transmission.

## 2.3 Flow instrumentation

### 2.3.1 Hot-wire velocimetry

Hot-wire velocimetry was employed in order to make instantaneous measurements of gas phase velocity. Hot-wire velocimetry was chosen over other conventional methods of measuring gas-phase velocity such as PIV due to its relative simplicity and ability to make accurate measurements very close to the wall. The probe used for the measurements was a boundary-layer type probe from Dantec dynamics with a 4 mm prong spacing. The wire used was a 5 $\mu$m diameter, gold plated tungsten wire with a 1.25 mm long active region, which was soldered to the prongs. The wire was operated with an AA Lab Systems AN-1003 hot-wire box in constant temperature mode at an overheat ratio of 1.8. The voltage signal passes through a Frequency Devices 901 8-pole Butterworth filter, and then is sampled using a Labview PCI card (PCI-MIO-16E-4). The hot-wire box allows for the measurement of the frequency response of the wire, which is found to be around 30 kHz, larger than the highest frequency that needed to resolved in the flow for all Reynolds numbers.

The hot-wire is calibrated using the same calibration jet used by Elkins (1997). The jet air is supplied by the main wind tunnel, and the blower speed was manually adjusted using a manual control available on the blower controller. The wire was placed in the potential core of the jet during calibration, and the jet speed at this location could be controlled between 1-25 m/s. The jet turbulence intensity at its core was less than 1% for the given range of velocities. The jet velocity during calibration was measured using a pitot probe in conjunction with a Setra model 239 pressure transducer, with the pitot probe placed as close as possible to the hot-wire probe

without disturbing the flow around the probe. The velocity was calibrated for 5-6 points around the expected mean velocity in the experiment, and the raw voltage signal from the probe and the amplified bridge voltage from the hot-wire box were both recorded simultaneously. The calibration was also conducted at two different temperatures, with a resistive heater connected to the jet, and a thermocouple attached to the hot-wire probe stem recording the temperatures. The following equation used by Elkins (1997) is fit to the calibration data for different temperatures:

$$u = \nu(T_{film}) \left( \frac{Be^2}{k_f(T_{film})(T_w - T_f)} - E_0^2 \right)^{1/n} \tag{2.1}$$

Where $u$ is the gas phase velocity, $\nu$ is the gas kinematic viscosity, $e$ is the hot-wire voltage, $T_{film}$ is the film temperature of the hot-wire probe, $k_f$ is the gas thermal conductivity, $T_w$ is the hot-wire temperature, and $T_f$ is the gas phase temperature. $B, E_0^2$, and $n$ are all fitting parameters. The calibration is performed before and after the experiment to check for drift. Once the calibration is obtained, the hot-wire voltage can readily to converted into velocities. The uncertainty for the measurement was computed by using the residual from fitting the calibration data to the above equation, as the errors from other parts of the measurement such as the pressure transducer or thermocouple were nearly negligible.

### 2.3.2 Fine-wire thermocouple

To make mean temperature measurements of the flow, a fine-wire thermocouple mounted on a custom made pronged probe is used. The thermocouple is a 75 $\mu$m diameter butt-welded K-type thermocouple from Omega. The body of the probe is a custom made hollow aluminum body with two hypodermic needles inserted and glued onto the body; the two needles are oriented at an angle away from each other, acting as the prongs for the thermocouple wire. The thermocouple is fed through these two prongs, with the junction centered between the two prongs. The length of thermocouple wire exposed between the two wires is 5.5 mm, and the rest of the wire inside the needles and cylinder body is insulated. The configuration of the probe is

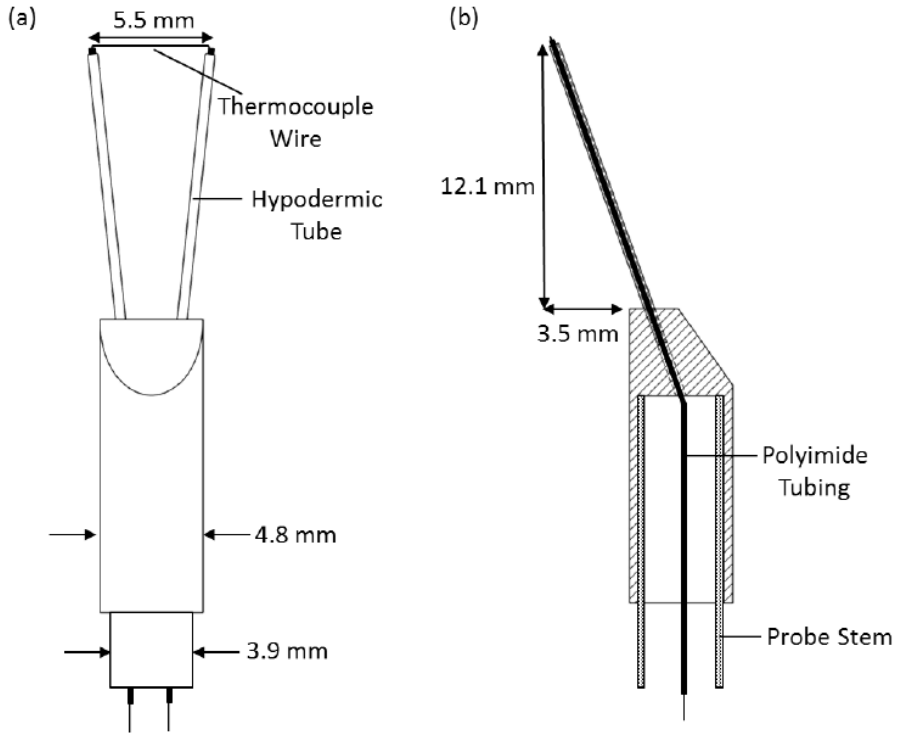


Figure 2.15: Two perpendicular views of the custom made fine-wire thermocouple probe. Figure credit to Banko (2018).

shown in Figure 2.15. The thermocouple signal is acquired using a NI 9214 module, with 500 samples at 50 Hz for each traverse point. The uncertainty in the mean temperature measured by the thermocouple is estimated to be about 0.2° C. This was obtained by comparing measurements to other similar K-type thermocouples in an isothermal environment. Estimates by Banko (2018) show that conductive losses to the prongs are negligible: to have the junction reach 99 % of the flow temperature relative to the prong temperature, the required wire length is 6 mm at the highest Reynolds number of the experiments. The fine-wire thermocouple is only used for mean temperature measurements, as its thermal response is too slow to resolve the relevant time scales in the flow.

### 2.3.3 Cold-wire thermometry

Cold-wire thermometry was used to make measurements of fluctuating temperature, as the response of the thermocouple was too slow. The probe used for the cold-wire measurements is a Dantec Dyanmics boundary-layer type probe with a 0.6 mm prong spacing. The wire used is an unplated 2.5 $\mu$m tungsten wire soldered onto the prongs. The original attempts at measurement employed a 1 $\mu$m wire, but this was found to be too fragile and always broke in the harsh environment of particle-laden flow. As the response time for a 5 $\mu$m wire is too high, the compromise is to use 2.5 $\mu$m diameter wire with frequency compensation. The cold-wire is run in constant current mode using the circuit developed by Elkins (1997). The bridge voltage is excited using an Agilent E3634A digital power supply, with an excitation voltage selected such that the wire is heated by less than 0.2° C. This excitation voltage allows for a temperature sensitivity of approximately 6° C/V. The voltage signal is passed through the same Frequency Devices 901 8-pole Butterworth filter used for the photodiode and hot-wire measurements, and is acquired with a Labview PCI card (PCI-MIO-16E-4).

To calibrate the cold-wire, the same calibration jet used for the hot-wire measurements is employed. The bridge is balanced to the expected mean temperature and velocity expected in the experiment. The jet temperature is varied with a resistive heater, and the temperature is monitored with a K-type thermocouple. The temperature is given time to reach steady state before each calibration point. The temperature varies less than 0.05° C during acquisition of the calibration point, and the RMS temperature fluctuations are found to be less than 0.07°C. Once 3-4 calibration points are obtained, the temperature and voltage are fit to a line. Comparing calibrations before and after the experiment, the slope was found to vary by less than 2%.

As the frequency response of the 2.5 $\mu$m wire is insufficient to resolve all fluctuations associated with the preferential concentration of particles, a frequency compensation scheme is used to correct the high frequency response of the wire. The method is described in more detail in Elkins (1997) and Banko (2018), but works as

follows. The wire is placed in the calibration jet at the mean temperature and velocity expected in the experiment, and the bridge excitation is oscillated at 10 Hz using square waves generated from the function generator. The response of the wire to the oscillating excitation is then measured. For the calibration, the cut-off frequency of the low-pass filter is increased to 90 kHz to minimize the effects of Gibbs ringing from the function generator on the response of the wire. This procedure is repeated for multiple velocities as the frequency response is velocity dependent. Once the step response is obtained, the transfer function of the probe is backed out and fit to two model transfer functions in order to determine the wire cut-off frequency $f_w$:

$$H(f) = \frac{1}{1 + if/f_w} \tag{2.2}$$

$$H(f) = \frac{1}{1 + if/f_w} - \frac{tanh(\sqrt{1 + if/f_w}L_w)}{1 + if/f_w\sqrt{1 + if/f_w}} \tag{2.3}$$

Where $L_w = (l_w/2)\sqrt{\alpha_w/(2\pi f)}$ is a non-dimensional conduction length scale, and $\alpha_w$ is the thermal diffusivity of the wire. Equation 2.2 models the transfer function of a very long wire with $l_w/d_w \geq \mathcal{O}1000$, while Equation 2.3 also considers the 1-D unsteady conduction in the wire to prongs held at a fixed temperature (Wroblewski and Eibeck, 1991). The compensated response is then obtained by dividing the Fast Fourier Transformed (FFT) signal with the transfer function. Also worth noting is the effect of the prongs on the response of the wire; Wroblewski and Eibeck (1991) found that it could attenuate the frequency spectrum by a roughly constant factor above 1 Hz, with the plateau given by the following:

$$|H_{plat}| = 1 - \frac{1}{L_w} \tag{2.4}$$

For the probe used in the present work, this plateau was found to be around 0.5.

The uncertainty in the cold-wire measurements had numerous sources: the electronic noise floor of the circuitry, day-to-day variations in the same measurement, and sensitivity to the cut-off frequency. For the lower power measurements (1 kW and lower), the uncertainty was found to be approximately 0.1°C.

### 2.3.4 High-speed imaging

To determine instantaneous particle positions (from which various statistics such as particle concentration or velocity could be obtained), the particles had to be imaged at a high frequency. To that end a Phantom V2012 high speed camera is used in conjunction with a 200 mm Nikkor lens. The illumination for the particles is provided with a Spectra Physics Model TBD Argon ion laser spread into a laser sheet with a cylindrical lens. The sheet thickness was measured to be approximately 1 mm. A custom made calibration grid is used to focus and calibrate the images. For synchronized measurements between the camera, cold-wire, and photodiode, the camera is triggered using a falling edge signal provided by a Labview PCI card (PCI-MIO-16E-4).

The images are acquired at 30 kHz for up to 12 seconds, and post-processed to identify particle locations. The images are first background subtracted, median filtered, and thresholded, and particles are identified as connected components within each image. The centroids, areas, and moments of inertia of the particles can then be computed; the centroids are used for the computation of preferential concentration statistics.

# Chapter 3

# Duct Configuration Measurements

The square duct configuration was used to obtain a variety of temperature and radiation transmission measurements. The objective was to examine the effect of a preferentially concentrated particle phase on the radiation transmission, and the effects on the heat transfer to the fluid phase from the radiation absorbed by a non-uniformly distributed particle phase. The initial characterization of the unheated flow, particle concentration, and preferential concentration was performed by Andrew Banko and Laura Villafane prior to the author's involvement in the project. These unheated characterization measurements of the duct flow are detailed in Banko (2018).

## 3.1 Parameter space

The main parameter that was varied for the experiments was the mass loading ratio $\Phi_m$, which is defined as the ratio of mass flux of the disperse particle phase to that of the fluid phase. The experiments were all performed at the same Reynolds number of $Re_H = U_b H/\nu = 20000$, where $U_b$ is the bulk flow velocity and $H$ is the duct width. The mass loading ratio values tested were $\Phi = 0, 0.1, 0.2, 0.4$. As described in Chapter 2, higher loadings and lower Reynolds numbers could not be tested due to significant particle accumulation on the walls when heating was present. For these high loading, low Reynolds number cases the accumulation was significant even

| $\Phi_m$ | $\Phi_V$ | $\tau$ |
|---|---|---|
| 0.1 | $1.31 \cdot 10^{-5}$ | 0.08 |
| 0.2 | $2.63 \cdot 10^{-5}$ | 0.16 |
| 0.4 | $5.26 \cdot 10^{-5}$ | 0.32 |

Table 3.1: Table of non-dimensional parameters dependent on mass loading. $\Phi_m$ is the particle mass loading ratio, $\Phi_V$ is the particle volume fraction, and $\tau$ is the mean optical depth through the particle-laden duct, defined by $\tau = \int_0^H Q_{ext} A_{cs} n(s) ds$. Note that $\tau$ is a nominal mean optical depth obtained from the mass loading ratio, assuming a Poisson distributed particle field. $Q_{ext}$ is the particle extinction coefficient, $A_{cs}$ is the particle cross-sectional area, and $n$ is the particle number density.

| $\boldsymbol{Re_H = 20000}$ | | | | |
|---|---|---|---|---|
| $Re_\tau$ | $d_p/\delta_\nu$ | $d_p/\eta$ | $St^+$ | $St_\eta$ |
| 1180 | 0.17 | 0.34 | 11.3 | 46 |

Table 3.2: Table of non-dimensional flow parameters at the test Reynolds number of $Re_H = 20000$. $Re_\tau$ is the friction Reynolds number based on the perimeter-averaged friction velocity. $d_p$ is the particle diameter, $\delta_\nu$ is the viscous length scale, $\eta$ is the Kolmogorov length scale, $St^+$ is the Stokes number based on the friction time scale, and $St_\eta$ is the Stokes number based on the Kolmogorov time scale.

without any heating, and it was observed that often heating increased the particle accumulation. The mechanism behind this increased accumulation due to clustering is unclear, but could possibly be caused by local changes to properties of the glass under heating. Relevant physical properties and non-dimensional parameters at $Re_H = 20000$ and various mass loadings are shown below in Tables 3.1, 3.2, and 3.1.

Table 3.1 summarizes the dependence of various non-dimensional parameters that change with mass loading. The average volume fraction for all loadings is of the order of $10^{-5}$, which indicates the particle momentum and fluid momentum are two-way coupled. This is a slight oversimplification, as there is a large range of particle concentrations depending on the region of the flow; in the core of the duct, the flow is very dilute and likely mostly one-way coupled for all loadings tested. Close to the walls, however, the particle concentration significantly increases due to turbophoresis (particle migration towards the walls caused by Reynolds stress gradients), and the densities are such that the flow and particle momentum are two-way and even

| Quantity | Value |
|---|---|
| Particle diameter $d_p$ | $1.2 * 10^{-5}$ m |
| Particle density $\rho_p$ | 8890 kg/m$^3$ |
| Particle absorption coefficient (at 975 nm) | 0.39 |
| Particle extinction coefficient (with diffraction at 975 nm) | 1.24 |
| Particle extinction coefficient (at 632 nm) | 2.17 |
| Particle Nusselt number $Nu_P$ | 2 |
| Fluid density $\rho_f$ | 1.27 kg/m$^3$ |
| Fluid kinematic viscosity $\nu_f$ | $1.57 \cdot 10^{-5} m^2/s$ |
| Fluid specific heat capacity $c_{p,f}$ | 1005 J/kg$\cdot K$ |
| Fluid thermal diffusivity $\alpha_f$ | $2.21 \cdot 10^{m2}/s$ |
| Duct width $H$ | 0.04 m |
| Duct heated length $L$ | 0.16 m |
| Incident radiative flux* $I$ | 0.245 MW/m$^2$ |
| Radiation wavelength $\lambda$ | 975 nm |
| Radiation full angle divergence $\theta$ | 18° |

Table 3.3: Table of relevant particle, fluid, and radiation properties. *The radiative flux is computed at the wall bisector where the radiation profile peaks, with the diodes outputting 1 kW.

four-way coupled. The mean optical depth varies from an optically thin regime at the lowest mass loading to an optically thick regime at the highest loading. Most other relevant quantities that only vary weakly with mass loading in the parameter space investigated, such as preferential concentration statistics in the duct core, flow statistics, and temperature statistics, are not listed.

The friction Reynolds number $Re_\tau$ in Table 3.2 was computed using the perimeter-averaged wall shear stress; the friction velocity was computed using a momentum balance with the mean pressure gradient. The viscous length $\delta_\nu$ and the viscous particle Stokes number $St^+$ were also obtained from the perimeter-averaged wall shear stress. The Kolmogorov length scale $\eta$ and particle Stokes number based on the Kolmogorov time scale $St_\eta$ were obtained from the streamwise pressure drop along the duct by estimating a cross-sectionally averaged dissipation rate.

In Table 3.3, the particle absorption and extinction coefficients were computed by Banko (2018) using an open source Mie scattering code written by Mätzler (2002).

It is important to note that the phase function for the particles show a large forward lobe caused by diffraction, spanning about 30° in the direction of the radiation propagation. Since much of this forward-propagated radiation is both participating in interactions with the particulate medium and is also measurable by the bulk calorimeter, the particle extinction coefficient is reduced from that without accounting for diffraction effects to give a more representative value (reduced from 2.19 to 1.24) for the bulk calorimeter measurements. The particle Nusselt number $Nu_p$ is obtained using the Nusselt number correlation proposed by Whitaker (1972), using a particle slip Reynolds number of 0.17 estimated from the Kolmogorov velocity. The characteristics of the radiation emitted from the laser diode array are obtained from the manufacturer's specifications. As described in Chapter 2, the laser diode array elements are arranged in three vertical columns of 24 elements each. Only the center column of laser diodes was used at a total power of 1 kW for the measurements presented in this chapter.

## 3.2 Characterization of the radiation source

The radiation profile from the laser diode array must be characterized to understand the variation of the radiative flux in the streamwise and wall-parallel directions. This characterization was performed using the bulk calorimeter and calorimeter array described in Chapter 2. The bulk calorimeter was used primarily to obtain the total transmission of radiation through the duct walls and particles. As it was positioned outside the duct, it was able to obtain the transmitted radiative power during an experiment, but as it spatially-averaged the incident radiative power over its observing surface, it could not be used to obtain spatial profiles of radiative flux. Hence the calorimeter array was designed to perform spatial measurements of radiative flux.

As described in Chapter 2, the calorimeter array consists of 9 copper elements embedded onto a ceramic base. The incident radiative flux on each element is estimated using the thermal response of that element. A typical thermal response for all 9 elements when exposed to the laser diode array is shown in Figure 3.1. The element temperature is initially flat when the radiation is not turned on, then rises

very slightly due to the radiation absorption by the shield itself, which conductively transfers a small amount of heat to the elements. Note that the radiation is not directly incident on the elements at this time. The temperature response then rapidly rises almost linearly when the shield blocking the radiation is removed around 27 seconds in Figure 3.1. The radiation is then turned off, which causes the temperature to fall. The region where the temperature rapidly rises is used to estimate the relative heat flux between the elements by performing a linear fit to this region. By using a linear fit to the temperature response, we are effectively assuming that the heat transfer from the incident radiation on the element is significantly greater than losses to conduction and convection, resulting in a linear increase in the temperature in time.

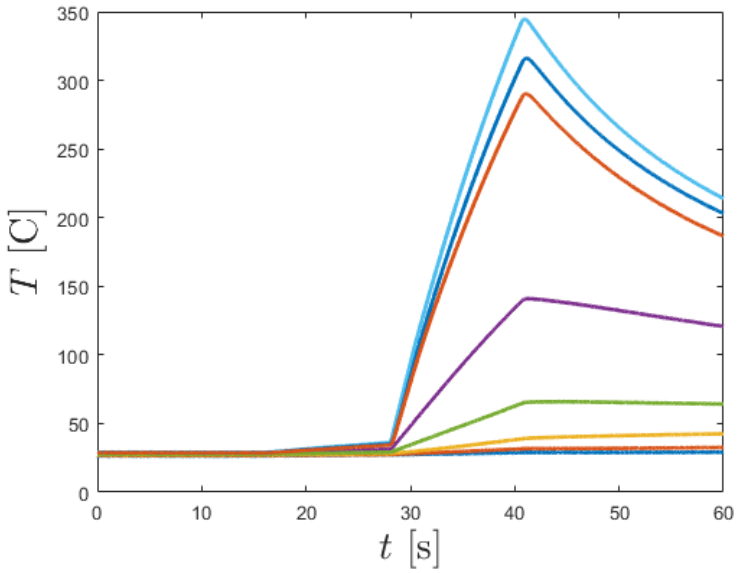


Figure 3.1: Temperature responses of all nine calorimeter array elements. The response is initially zero when the radiation is shielded from the array surface. The shield is then quickly removed, resulting in a linear region of rapid temperature rise, which is used to obtain the relative incident heat flux.

In order to account for minor differences in thermal capacity, contact resistance,

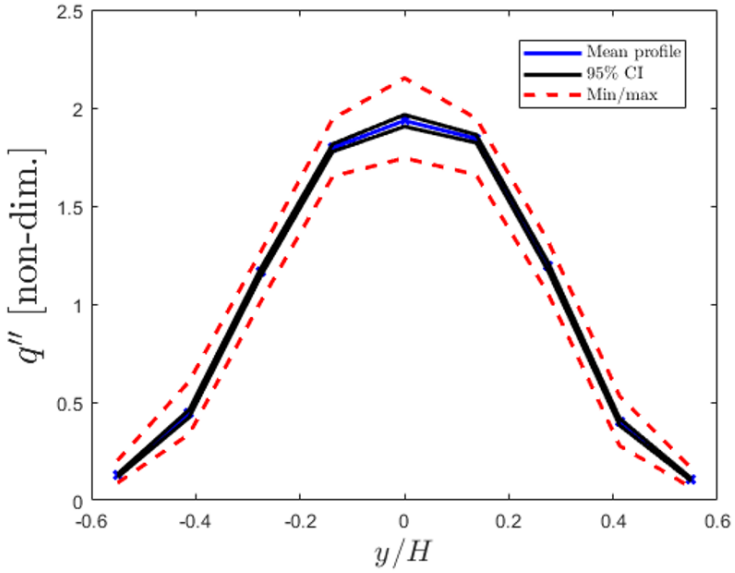


Figure 3.2: The wall-parallel heat flux profile from 14 streamwise locations spaced 11 mm apart. Each wall-parallel profile (for every streamwise location) was scaled by its wall-parallel average value, and the average of these scaled profiles are shown in the blue line. The black line is the 95% confidence interval based on the deviations observed in these scaled profiles. The dotted red lines are the maximum and minimum scaled values for each wall-parallel location.

and surface absorptivity, each element was calibrated with a steady and focused radiation source, and individual responses for each element were obtained for a constant radiative flux (the calibration radiation source used was a separate Argon-ion laser). For the calibration response, the region of rapid temperature rise was used again to perform a linear fit, and differences between the slopes of the element responses were used to correct relative differences in the measured heat flux among elements.

As the calorimeter array is only discretized in one dimension, the array was mounted on a traverse to obtain the streamwise variation in the heat flux profile. Fourteen streamwise locations spaced 11 mm apart were measured. Each wall-parallel profile (for every streamwise location) was scaled by its wall-parallel average value,

and the average of these scaled profiles are shown in Figure 3.2. Figure 3.3a shows the relative differences in the peak (center) heat flux for each streamwise location, and Figure 3.3b shows a 2-D map of all heat flux profiles. The profiles show a shape that is close to Gaussian for most streamwise locations, but also show a significant variation in magnitude in the streamwise direction. As most of the other measurements are downstream of the heated section, the effect of these streamwise variations are mostly averaged out. The wall-parallel variations (streamwise-normal, radiation-normal, array-parallel), however, are not random and create persistent gradients in the heat flux in the flow, inducing heat transfer in the wall-parallel direction.

To estimate the error from neglecting convection and conduction from the calorimeter elements, the thermal energy balance was discretized for each element with second order differencing in space and first order differencing in time. A single copper element and the surrounding ceramic was lumped together, leading to the following equation:

$$\left(\rho_{Cu}c_{p,Cu}V_{Cu} + \rho_{ce}c_{p,ce}V_{ce}\right)\frac{T_i^n - T_i^{n-1}}{\Delta t} = \frac{kA_{cs}}{\Delta x}\left(T_{i-1}^n - 2T_i^n + T_{i+1}^n\right) - hT_i^n A_s + q_{rad}A_{rad} \tag{3.1}$$

$T_i^n$ is the temperature of the $i$'th lumped element at the $n$'th time step. For the first unsteady term, $\rho_{Cu}$, $c_{p,Cu}$, and $V_{Cu}$ are the density, specific heat, and volume of the copper element, and $\rho_{ce}$, $c_{p,ce}$, and $V_{ce}$ are the same properties for the Macor ceramic surrounding a single copper element. For the second conduction term, $A_{cs}$ is the cross-sectional area between each lumped element and $k$ is the thermal conductivity. For the third convective heat transfer term $h$ is the heat transfer coefficient for natural convection from a vertical wall, and $A_s$ is total surface area where natural convection can occur. The final term is the incident radiative flux term, where $q_{rad}$ is the radiative flux and $A_{rad}$ is the area the radiation is incident on. Figure 3.4a and Figure 3.4b show the comparison between applying this correction and neglecting this correction. The profiles show little difference with and without correction, demonstrating that neglecting conduction and convection is a valid assumption in

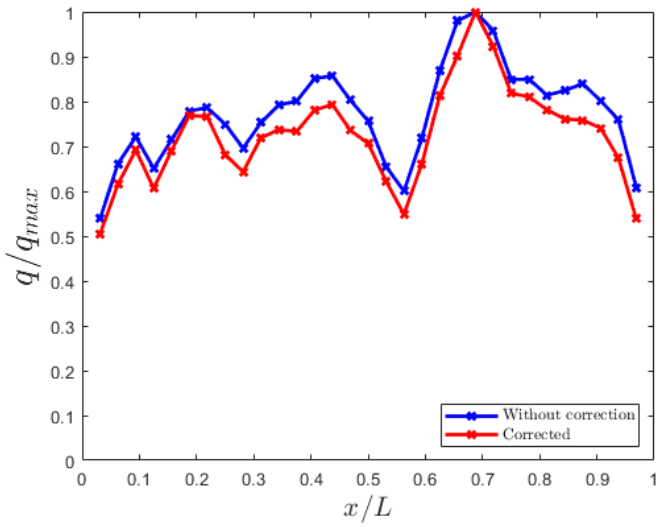


(a) The peak (center) radiative flux measured for each streamwise location measured by the calorimeter array. The peak values are scaled by the globally observed peak. The streamwise coordinate $x$ is normalized by the heated length $L$.

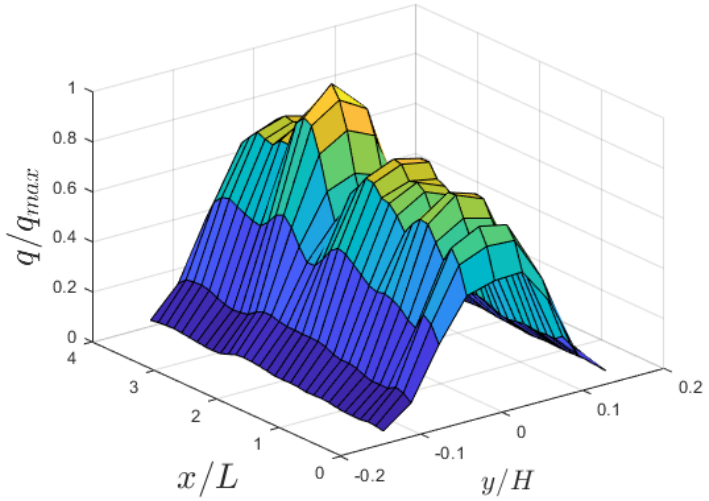


(b) 2-D map of the heat flux profile. The heat flux values $q$ are normalized by the global peak $q_{max}$. The streamwise coordinate $x$ is normalized by the heated length $L$, and the wall-parallel coordinate is normalized by the duct width $H$.

Figure 3.3: Streamwise dependence of calorimeter heat flux quantities.

estimating the radiative heat flux for this regime.

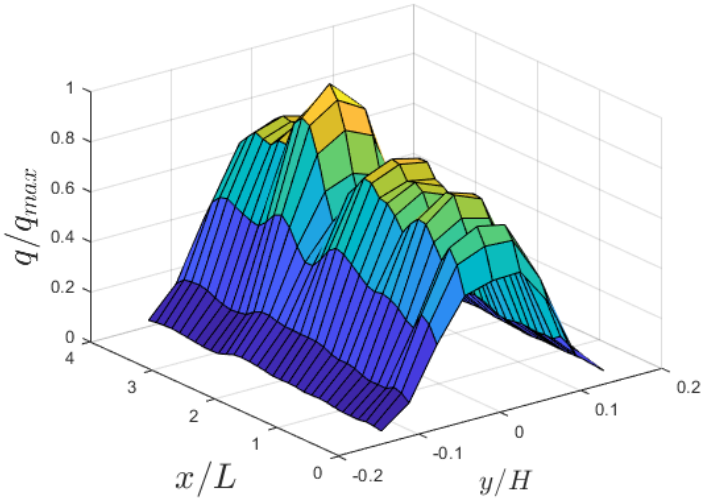


(a) 2-D map of the heat flux profile, without any heat loss corrections.

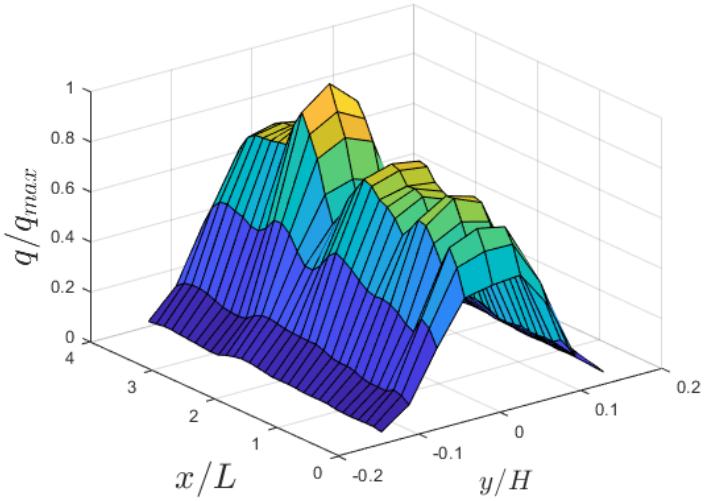


(b) 2-D map of the heat flux profile, with conduction and convection corrections.

Figure 3.4: Effect of the conduction and convection correction on the calorimeter array heat flux estimate. The profiles show little difference with and without correction, demonstrating that neglecting conduction and convection is a valid assumption in estimating the radiative heat flux for this regime.

## 3.3 Transmission measurements

The transmission of radiation through the particle-laden duct flow was measured using a helium-neon laser in conjunction with a fast-response photodiode as described in Chapter 2. The fractional transmission $I/I_0$ is obtained by measuring radiative flux without any particles present $I_0$, and then measuring the incident radiative flux with the particles flowing through the duct, $I$. As the divergence of the laser beam and the sensor area of the photodiode are both small, these measurements capture almost purely the transmitted radiation with minimal scattered radiation. The measurement was performed for the three values of mass loading $\Phi = 0.1, 0.2, 0.4$, downstream of the heated section at the wall bisector. It is important to note that the flow was not heated with the laser diode array during these measurements, and the power from the helium-neon laser was too low to notably heat up the flow; hence there is no modification of the flow due to heating effects. Figure 3.5 plots the fractional mean transmission versus the average optical depth, and compares these values to the expected exponential attenuation from a classical Beer-Lambert Law. As the wall particle concentration is higher than the duct-averaged value in a square duct as demonstrated in Abdehkakha (2017), in order to perform a fair comparison between Beer's Law from the duct-averaged optical depth and the wall-bisector photodiode measurements, the optical depth used for Beer's Law is determined by fitting the exponential curve to the first two lower loading points, rather than just using the duct-averaged optical depth. It is also worth noting that the optical depths here are much larger than the nominal values estimated from the mass loading ratio or the bulk calorimeter measurements, as the photodiode essentially acts as a point measurement of the transmitted light. All the light that is scattered from the beam path misses the photodiode sensor area, whereas in the bulk calorimeter (or any area-averaged estimate), a much larger fraction of the scattered light ends up incident on the calorimeter surface.

Figure 3.5 shows that for the highest loading super-exponential transmission occurs beyond the experimental uncertainty. This is due to the preferential concentration of particles in the flow, and has been hypothesized or observed in computations

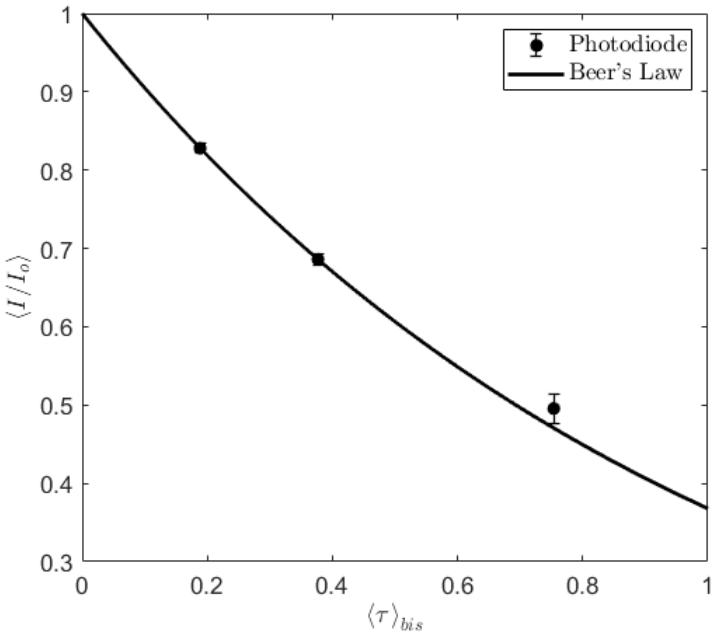


Figure 3.5: Fractional mean transmission of the He-Ne laser beam through the particle-laden duct, as measured by the photodiode. The transmission is plotted versus the mean optical depth and compared to exponential extinction predicted by Beer's Law.

in previous works (Kostinski (2001), Frankel et al. (2017)). It is caused by increased line of sight distances through the medium, which causes increased mean transmission compared to that of a medium distributed from a Poisson process. Assuming homogeneity and isotropy of the extinction field, introducing the two-point correlation function $R_{\sigma\sigma}$, and assuming that the fluctuations in the optical depth are small, analysis from Banko (2018) shows that the mean transmission can be expressed as the following:

$$\langle I/I_0 \rangle = e^{-\langle\sigma\rangle y + \int_0^y (y-s) R_{\sigma\sigma}(s) ds} \tag{3.2}$$

where $\sigma$ is the local extinction coefficient. The second term in the exponential demonstrates that in a medium with positive spatial correlations, the mean transmission can exceed the exponential decay predicted by Beer's Law.

The time-resolved measurements of the transmission and the fast response of the photodiode allow us to also make concurrent measurements of the transmission fluctuations. Plotted in Figure 3.6 is the transmission RMS versus the mean optical depth. As the figure shows, the transmission fluctuations increase with optical depth over the ranges investigated. This is due to the fact that as mean particle concentration increases, the density of the clusters increases, producing large negative fluctuations in transmission. Conversely, as the beam passes through a large void the transmission is very high. As the optical depth is increased beyond the ranges measured, the transmission RMS is expected to start to decrease again as the overall attenuation of the radiation starts to overcome the initial fluctuation increase.

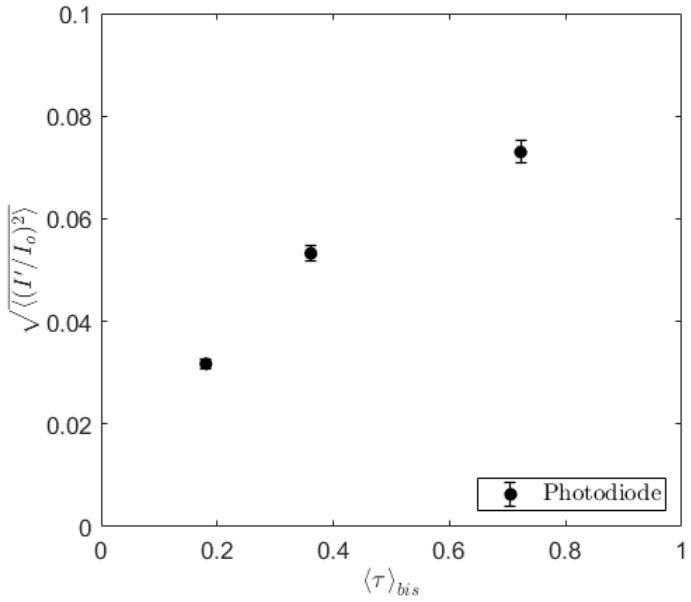


Figure 3.6: The transmission fluctuation RMS of the He-Ne laser beam through the particle-laden duct, as measured by the photodiode. The transmission RMS is plotted versus the mean optical depth.

Figure 3.7a plots the transmission PDFs versus mass loading. When normalized by the RMS, the fluctuations mostly collapse versus mass loading changes. This indicates that for the ranges of mass loadings tested, the preferential concentration

is not significantly changed when averaged over the length of the duct width (local changes versus mass loadings can and do occur especially at the walls, as shown later in the near-wall temperature results). The PDFs also show a negative skew, likely due to the fact that the transmission cannot exceed one. Figure 3.8a and Figure 3.8b show the spectra and pre-multiplied spectra. The frequency axes have been normalized with a characteristic bulk advection time scale $\tau_H = H/U_b$. The spectra show a similar trend to the transmission, with the spectra mostly collapsing for all mass loadings. The pre-multiplied spectra show that much of the contributions to the fluctuations come from relatively large structures in the flow corresponding to streamwise length scales of $\mathcal{O}(0.1H) - \mathcal{O}(H)$, which can cause the largest fluctuations as they attenuate a relatively large fraction of the radiation.

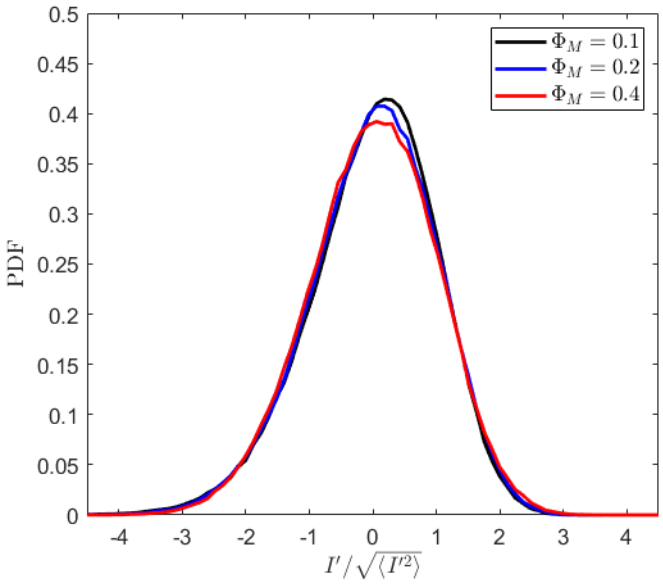


(a) The transmission fluctuation PDF of the He-Ne laser beam through the particle-laden duct, for varying mass loadings. The transmission fluctuations are normalized by the transmission fluctuation RMS.

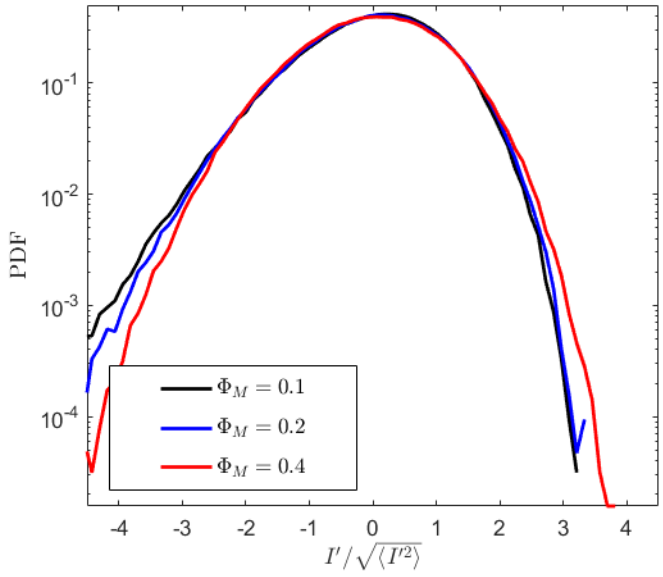


(b) The transmission fluctuation PDF of the He-Ne laser beam through the particle-laden duct, for varying mass loadings, in semi-log coordinates.

Figure 3.7: Transmission fluctuation probability density functions.

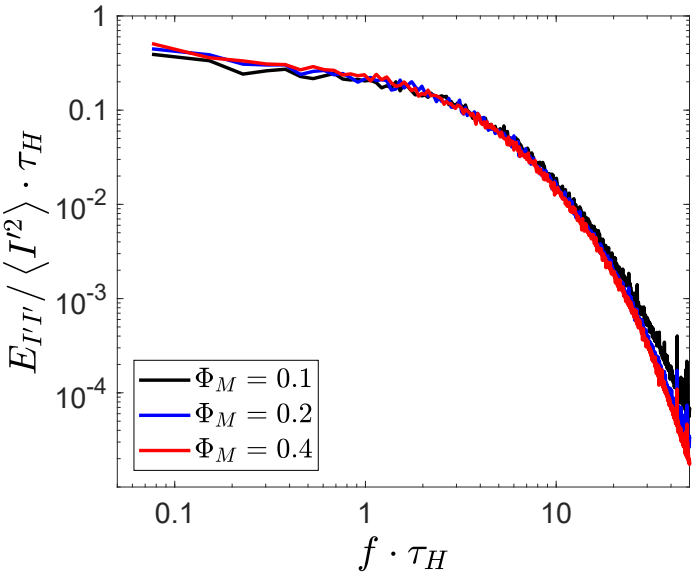


(a) The transmission spectra of the He-Ne laser beam through the particle-laden duct, for varying mass loadings. The frequency axis is normalized by the bulk advection time scale $\tau_H$.

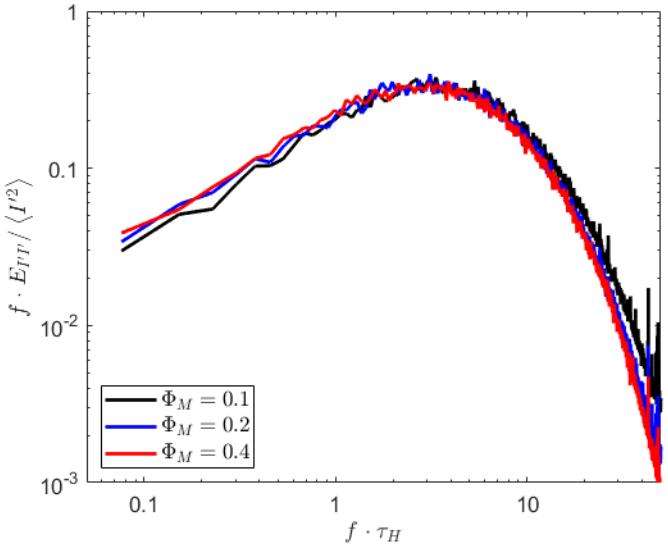


(b) The transmission pre-multiplied spectra of the He-Ne laser beam through the particle-laden duct, for varying mass loadings. The frequency axis is normalized by the bulk advection time scale $\tau_H$.

Figure 3.8: Transmission spectra for varying mass loadings.

## 3.4 Temperature measurements

### 3.4.1 Mean temperature measurements

Temperature measurements of the fluid phase were made in the duct with the fine-wire thermocouple probe described in Chapter 2, positioned 50 mm downstream of the heated section. This distance protected the probe from being irradiated by the laser diode array, and allowed time for the particles to come to thermal equilibrium with the surrounding fluid. Traverses from the duct center towards the wall were made for all three mass loadings, and zero mass loading. There was a non-zero temperature rise in the duct even with no particles due to the radiation absorption by the duct walls, which resulted in the formation of a thermal boundary layer that was present throughout all measurements. The temperature rise in all cases was measured relative to a reference in the contraction section upstream of the development section, denoted as $T_0$. As the addition of the particles into the flow cooled the flow slightly (air from the blower was slightly hotter than the particles in the feeder), a mass loading-dependent correction was also applied to the temperature rise.

The measured mean temperature profiles are shown in Figure 3.9a. The temperature rise is non-dimensionalized by the reference inlet temperature $T_0$, $T^* = \frac{T-T_0}{T_0}$, where all temperatures are measured on an absolute scale. The figure shows that for all loadings the temperature is lowest near the center of the duct and increases monotonically towards the wall. For the zero loading case, this is due to the presence of the thermal boundary layer from the absorbing walls. For cases with non-zero particle loading, the trend in mean temperature is a combination of the effects of radiation attenuation, the particle concentration profile, and the thermal boundary layer on the heated glass wall. As the radiation penetrates into the medium, it is mostly either absorbed or transmitted, and the radiation available for particles to absorb decreases deeper into the medium (close to exponentially, as seen from the transmission measurements), resulting in a lower temperature rise deeper into the medium. Another major controlling parameter for the temperature profile is the particle concentration. As measured by Banko and Villafane (Banko, 2018), the particle

concentration dramatically increases closer to the wall due to turbophoresis, resulting in a disproportionately large amount of radiation being absorbed near the walls, which causes the temperatures to peak near the wall. Finally, the thermal boundary layer also contributes to increasing temperatures closer to the walls. Figure 3.9b shows the same mean temperature rise data with the profile with no loading subtracted out. This gives an approximate measure of the contribution of the particle absorption to the mean temperature rise. As a variable amount of particles were deposited on the walls each time particles were run through the duct, a temperature traverse was performed before and after every particle-laden measurement. This gave an indication of the particle accumulation to potentially weed out measurements with significant particle build-up, but also a more accurate measure of the wall contribution to the temperature rise for each particle-laden traverse. The value of the non-dimensional temperature rise at the core of the duct peaks at around 0.04, which is insufficient to cause changes to the turbulence or particle preferential concentration through variable property, buoyancy, or dilatation effects.

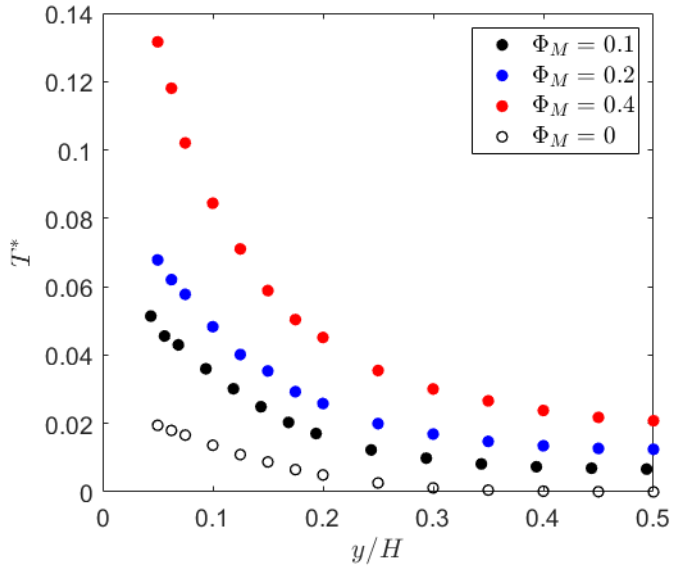


(a) The mean temperature rise in the duct measured with the fine-wire thermocouple probe for varying mass loadings. The non-dimensional temperature rise $T^*$ is normalized by the inlet temperature, and the wall-normal distance is normalized by the duct width $H$.

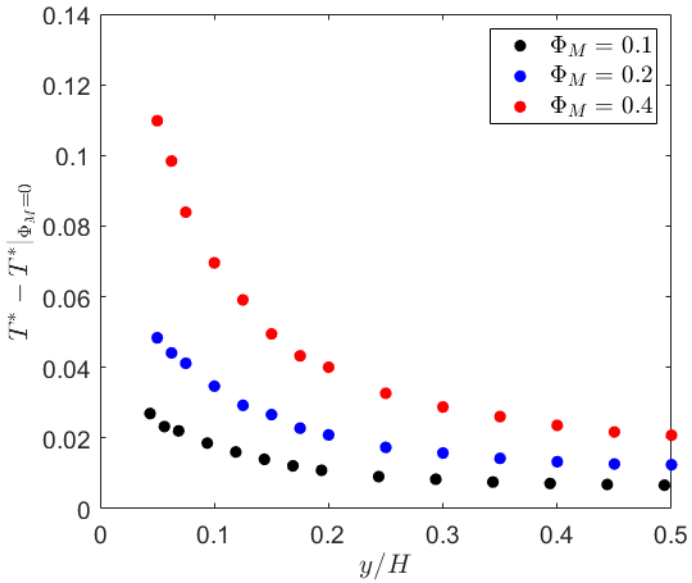


(b) The approximate particle contribution to the mean temperature rise in the duct measured with the fine-wire thermocouple probe for varying mass loadings. The approximate particle contribution is obtained by subtracting the temperature rise when no particles are present in the test section.

Figure 3.9: Mean temperature rise for varying mass loadings.

### 3.4.2 Temperature fluctuation measurements

The temperature fluctuations were measured at the same location using the cold-wire probe as described in Chapter 2. The RMS value of the non-dimensional temperature rise $T^*$ is plotted versus the distance from the wall normalized by the duct width. Similar to the mean temperature rise, we see the temperature fluctuations rise closer towards the wall and with increasing loading. This is likely due to the increase in the particle concentration towards the wall and with increasing loading, resulting in more intense spots of heating causing stronger fluctuations. While the fluid surrounding the particles has enough time to come into thermal equilibrium with the particles, the variations in temperature caused by preferential concentration have not yet have time to be fully mixed out by turbulence. The particles close to the wall are also transported away from the wall by ejection events (Rouson and Eaton (2001), Ninto and Garcia (1996)), which can act to enhance the temperature fluctuations near the wall. The RMS temperature rise is close to 1/3 of the mean temperature rise at its highest, and this is without compensation for the low frequency response due to the finite length of the wire, which can account for up to a factor of 2 increase in the fluctuations across all frequencies. The fluctuation magnitudes therefore can be significant compared to the mean temperature rise.

Figure 3.10 shows the temperature fluctuation PDFs, normalized by the RMS fluctuations. Figure 3.11a, which show the PDFs at the center of the duct, mostly collapse for varying mass loading. Similar to the transmission fluctuation PDFs, this indicates that changes in mass loading do not have a significant effect on the preferential concentration in the core of the duct. The PDFs are positively skewed, as the flow is mostly composed of cold voids devoid of particles, and the probe is more often sampling from these cold regions than the hot particle clusters. Figure 3.11d shows the temperature fluctuation PDFs near the walls in the log layer (at $y/H = 0.05$, $y/\delta_\nu = 62$). These near wall PDFs do not collapse for increasing mass loading; as the mass loading is increased we see the PDFs start to deviate from that of just the thermal boundary layer. For zero or low loading the PDFs are negatively skewed, which is in line with findings for a single-phase boundary layer with a heated

wall Kim and Moin (1989). As the loading is increased however, the PDFs skewness starts to increase towards symmetric. Similar to what was observed in the core of the duct, the fraction of negative fluctuations increase due to the more intermittent nature of the positive fluctuations. It is also worth noting the significant difference in the shape of the PDFs compared to that of the core of the duct. While the fluctuations from the thermal boundary layer is partly responsible for this difference, we can also note an increase in the probability of moderate fluctuations, and a decrease in the probability of intense fluctuations, which suggest a difference in the spatial organization of the particles and subsequent heat transfer to the fluid.

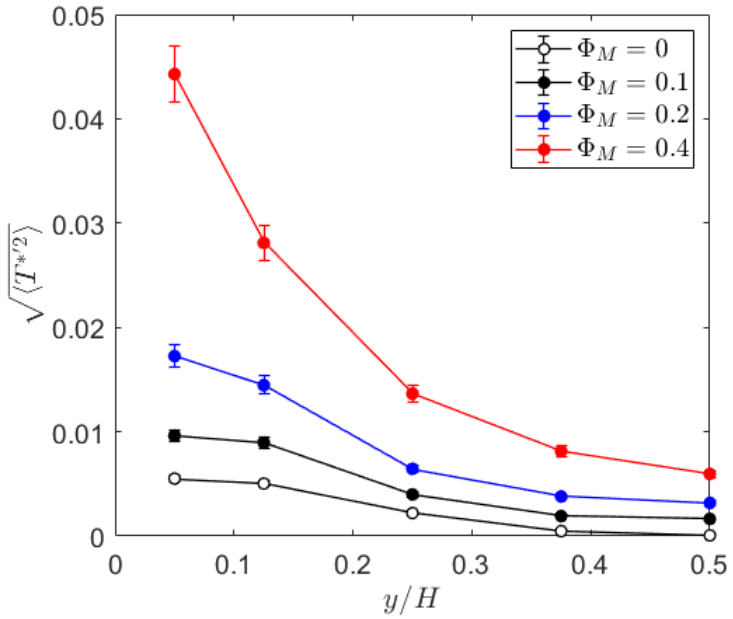


Figure 3.10: The temperature fluctuation RMS versus distance from the wall. The temperature fluctuation is normalized by the inlet temeprature, and the wall-normal distance is normalized by the duct width.

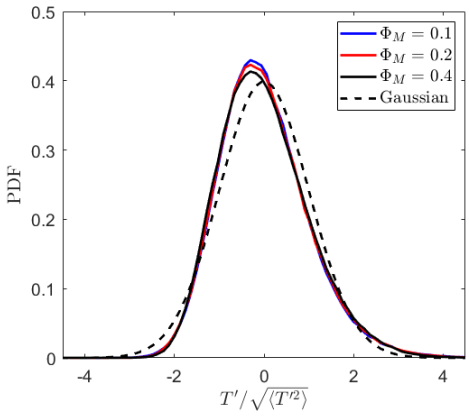


(a) The temperature fluctuation probability density function for varying mass loading at the center of the duct. The temperature fluctuations are normalized by the fluctuation RMS.

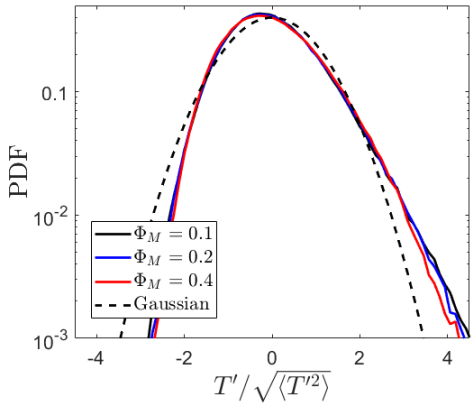


(b) Temperature fluctuation PDFs at the center of the duct, in semilog axes.

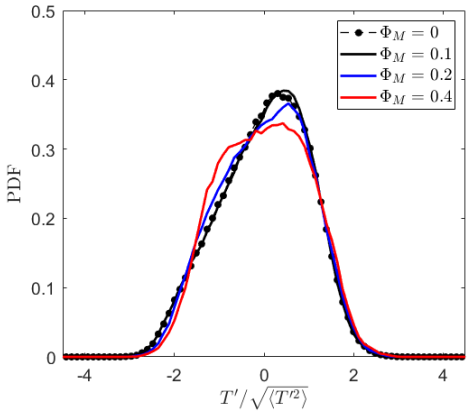


(c) The temperature fluctuation probability density function for varying mass loading in the log layer $y/\delta_\nu = 62$. The temperature fluctuations are normalized by the fluctuation RMS.

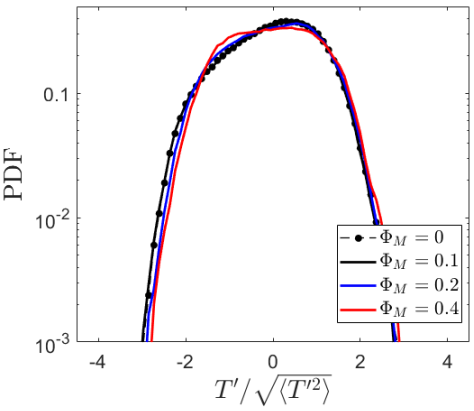


(d) Temperature fluctuation PDFs in the log layer $y/\delta_\nu = 62$, in semilog axes.

Figure 3.11: Temperature fluctuation PDFs for varying mass loadings at the center of the duct and near the wall.

Figure 3.12a shows the temperature fluctuation spectra at the core of the duct and near the wall, measured at the same locations as the PDFs. The frequency axis is again normalized by the bulk advection time scale $\tau_H$. Similar to the transmission

spectra, the spectra at the core of the duct are broadband and collapse for changing mass loadings. The pre-multiplied spectra in Figure 3.12b show that the the bulk of the energy contribution to the fluctuations come from structures with an implied streamwise length scale of about $0.5H$. The spectra in the log-layer, plotted in Figure 3.13a and Figure 3.13b, show a distinct effect of mass loading on the temperature fluctuations. As the mass loading is increased, the contribution to the fluctuations from low frequencies increase while the contributions from higher frequencies decrease. This pivoting effect becomes more pronounced for higher mass loadings. The increase in the low frequency content is likely due to the ejection of particles from low-speed streaks near the wall into the log-layer. Particles collect into long streamwise streaks as they interact with the near-wall turbulence as observed by Ninto and Garcia (1996). These streaks tend to be longer than the low velocity streaks characteristic of turbulent boundary layers, and are likely also coherent for a longer time scale after they are lifted from ejection events. Due to the thermal inertia of the particles, this can cause an increase in low-frequency content. The pre-multiplied spectra show that for lower loadings the bulk of the fluctuating energy contribution comes from structures with an implied streamwise length scale of order $0.1H$ to $10H$, while for the highest loading the energy contribution mostly comes from structures with an implied streamwise length scale of order $H$ to $10H$. These scales match with typical length scales of low-speed streaks near the wall, which are typically $\mathcal{O}(1000)$ viscous units. These results suggest that near-wall temperature statistics in a radiatively heated particle-laden flow are strongly modulated by coherent structures generated by wall turbulence.

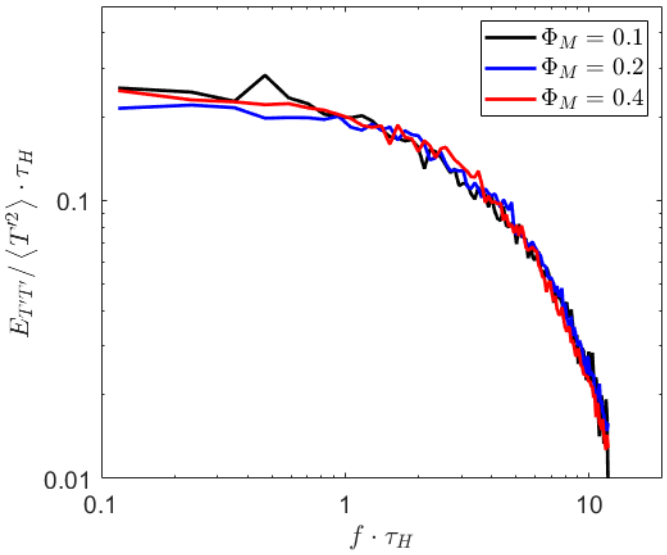


(a) The temperature spectra for varying mass loading at the center of the duct. The frequency axis is normalized by the bulk advection time scale $\tau_H$.

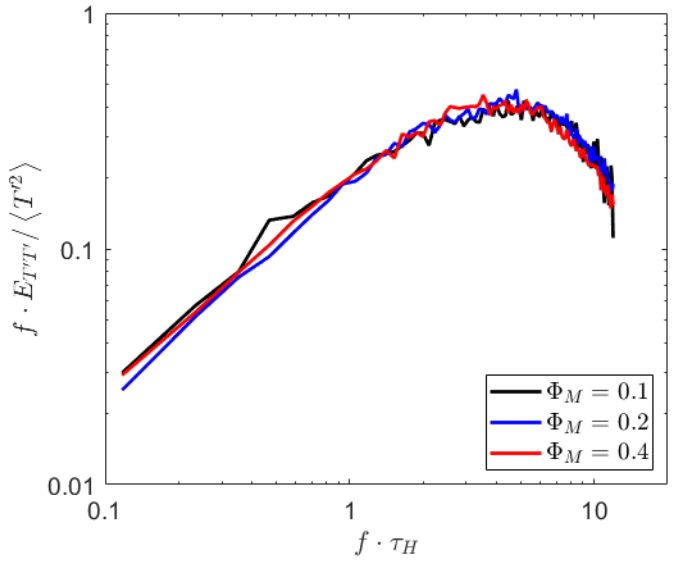


(b) The temperature pre-multiplied spectra for varying mass loading at the center of the duct. The frequency axis is normalized by the bulk advection time scale $\tau_H$.

Figure 3.12: Temperature spectra and pre-multiplied spectra at the core of the duct.

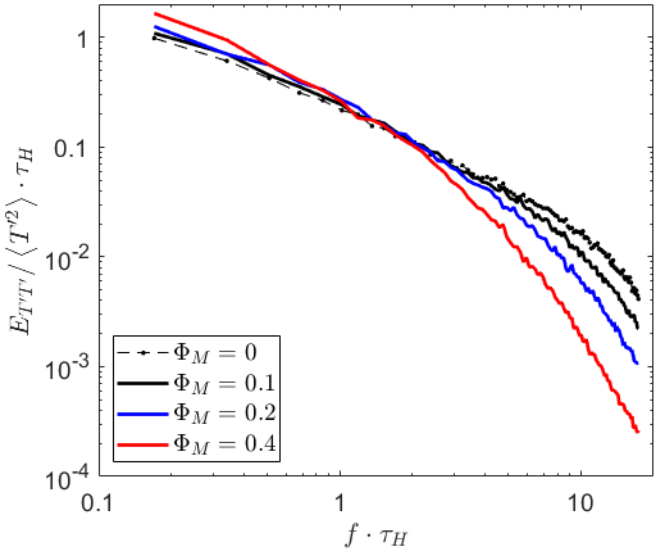


(a) The temperature spectra for varying mass loading in the log layer $y/\delta_\nu = 62$. The frequency axis is normalized by the bulk advection time scale $\tau_H$.

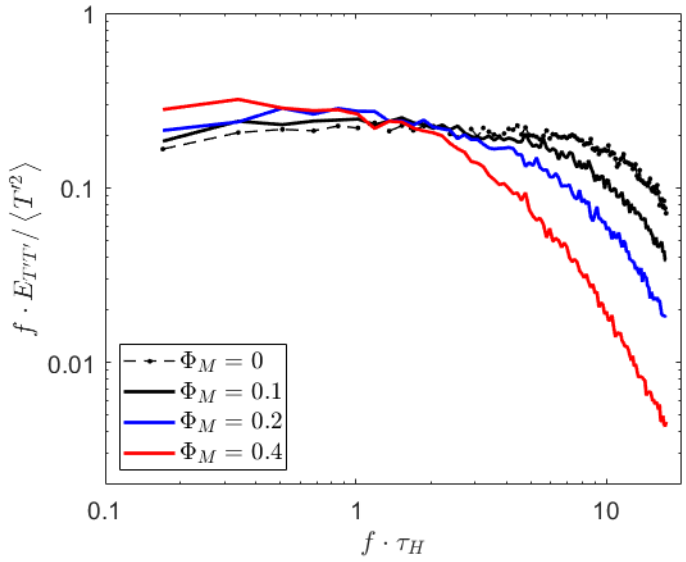


(b) The temperature pre-multiplied spectra for varying mass loading in the log layer $y/\delta_\nu = 62$. The frequency axis is normalized by the bulk advection time scale $\tau_H$.

Figure 3.13: Temperature spectra and pre-multiplied spectra in the log-layer of the duct wall.

## 3.5 Correlation measurements

Cross-correlation measurements between the number density and the fluid phase temperature were made using synchronized measurements of both quantities as described in Chapter 2. The temperature fluctuations are measured at the same streamwise location, at the center of the duct. The number density is measured by imaging particles that are illuminated by a beam from the helium-neon laser with a high-speed camera, with the beam positioned 0.2 duct widths above the cold-wire probe. The field of view of the high speed camera covers 3/4 of the duct width, centered at the duct center. The images are median filtered, background subtracted, contrast adjusted and thresholded. The particle centroids are then identified, and the particle counts are discretized into 1 mm bins along the beam to obtain the number density. The cross-correlation is then computed with the following definition:

$$\rho_{n'T'}(\Delta t) = \frac{\langle n'(t)T'(t+\Delta t)\rangle}{\sqrt{\langle n'^2\rangle}\sqrt{\langle T'^2\rangle}} \tag{3.3}$$

Figure 3.14 shows the number density-temperature correlation for varying mass loading. The time delay has been normalized by the bulk advection scale $\tau_H$. We first note that the effect of mass loading on the cross-correlation is relatively minimal, with small decreases in the correlation peak with mass loading. This can be attributed to the reduction in Poisson noise from finite particle count effects. The other feature worth noting is the value of the correlation peak. As the particles act as heat sources for the fluid flow, we can expect a very strong correlation with the particle number density and temperature with a correlation peak close to unity, but the peak is at a relatively diminished value of around 0.5. This is likely due to the combined effects of turbulent mixing and cluster break-up. Turbulent mixing can distribute the thermal energy away from the hot clusters into the cold fluid in void regions, and the break-up of clusters during its passage through the heated section can have similar effect by transporting the particles away from the heated fluid. A quantity closely related to the correlation coefficient that can be examined is the temperature-number density coherence function, which is defined as:

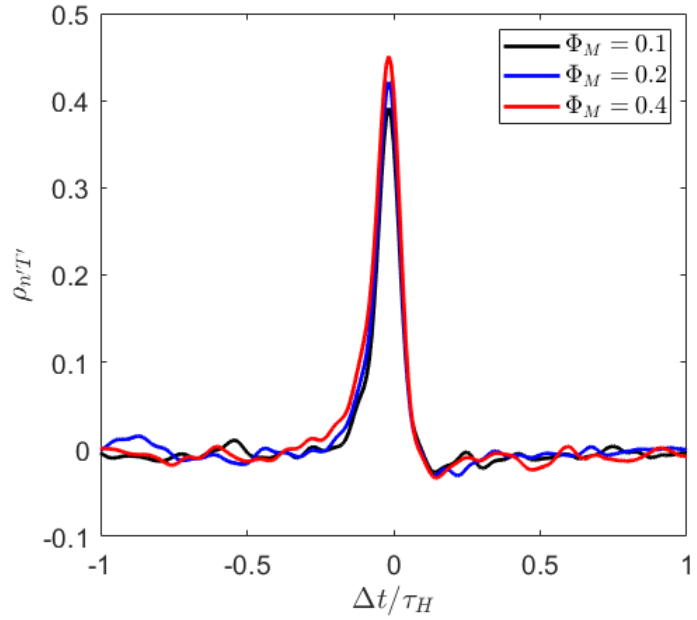


Figure 3.14: The number density-temperature cross-correlation for varying mass loadings.

$$C_{n'T'}(f) = \frac{|\hat{n}^f T'^*|^2}{\sqrt{|\hat{n}'^2|}\sqrt{|T'^2|}} \tag{3.4}$$

The coherence function, which can be interpreted as a measure of the frequency dependence of the correlation coefficient, is plotted in Figure 3.15 for all mass loadings. The frequency axis is again normalized by the bulk advection scale. For all loadings the coherence is relatively constant at approximately 0.35, and drops off for higher frequencies. The length scales associated with the lower frequencies correspond to scales larger than the duct width, consistent with length scales of coherent structures implied by the cold-wire and photodiode measurements. The drop-off at higher frequencies can likely be attributed to the aforementioned turbulent mixing, during which smaller eddies evolve faster to de-correlate the number density field with the temperature field.

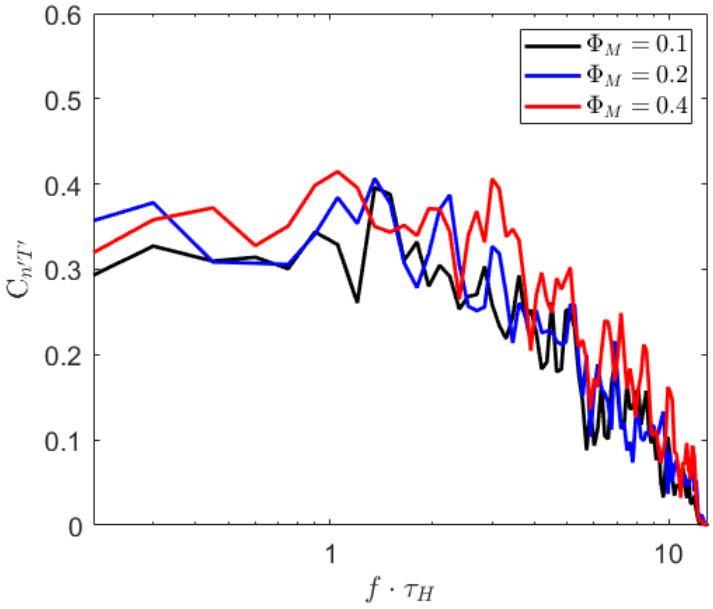


Figure 3.15: The number density-temperature coherence function for varying mass loadings. The frequency axis is normalized by the bulk advection time scale $\tau_H$.

# Chapter 4

# Co-flowing jet configuration measurements

The co-flowing jet configuration was used to examine effects of stronger radiative heating without the risk of test section breakage associated with particle accumulation on the test section walls. As described in Chapter 2, the aim of the new configuration was to try to keep the flow as consistent as possible to the duct configuration without a wall that could potentially break. The removal of the wall also removes a key aspect of the convective heat transfer present in the duct configuration in the form of a heated wall. As seen in the temperature statistics from the previous chapter, the heated wall and its associated thermal boundary layer played a significant role in the dynamics of the heat transfer, dominating the changes in temperature statistics for lower loadings. As the focus of this work is not to investigate the effects of a thermal boundary layer on the dynamics of a particle-laden flow, the new co-flow configuration will allow the experiment to better isolate the effects on the system purely due to heating from radiation absorption by the particles.

The co-flow and square jet bulk velocities are matched to minimize effects of significant shear layers and the additional mixing resulting from a square jet, but the removal of a no-slip wall does introduce significant changes to the flow even with this bulk velocity matching. As a point of emphasis, these changes are not introduced to

investigate possible effects resulting from aerodynamic differences between the duct and co-flowing jet configuration. The additional aerodynamic complexities of the co-flowing jet also imply that this new configuration is not as suitable as a test case for extensive validation as was planned for the duct measurements. The focus instead will be on exploring a new parameter space afforded to the experiment by being able to drive up the total incident radiative power and the radiation to five times what was possible in the duct flow. This increase has the potential to introduce new physics and phenomena that were not observed in the duct configuration.

## 4.1 Changes to parameter space

The main changes in the parameters explored in the co-flowing jet configuration are the changes to the mass loading ratio, the total incident radiative power, and an additional jet width-based Reynolds number. All other parameters are kept constant, although the modified flow configuration is expected to introduce some amount of change in parameters related to the aerodynamics of the flow. Two different duct width-based Reynolds numbers are tested: the previous Reynolds number of $Re_H = 20 \cdot 10^3$ tested in the duct is kept, but a lower Reynolds number of $10 \cdot 10^3$ also is investigated. The lower Reynolds number allows the mass loading ratio to be pushed to higher values, which leads to increased total optical depth and radiation absorption. The slower flow also results in a increased residence time in the heated section, which can lead to a more significant temperature rise. With the lower Reynolds number, the mass loading ratio can be extended up to $\Phi_M = 2.1$, over five times larger than the highest mass loading value of $\Phi_M = 0.4$ tested in the duct configuration. Although $Re_H = 40 \cdot 10^3$ feasibly could have been tested in the facility, it is omitted since it would have the opposite effect of limiting the temperature rise that could be observed in the flow. The mass loading ratio is capped at $\Phi_M = 2.1$ even though the feeder is capable of feeding more particles, as the system is limited total amount of particles that can be used in one experimental run; higher mass loadings would not be capable of running for the minimum measurement duration required to reduce initial system unsteadiness and reach statistical convergence. The wind tunnel was defined as having

reached steadiness when the Reynolds number did not fluctuate more than 5 percent from the target Reynolds number. This would usually be achieved in 2-3 minutes in the unladen cases, but with high loadings could take up to 5 minutes, potentially depleting a significant amount of particles from the feeder. Unheated flow parameters for both Reynolds numbers are shown in Table 4.1. $d_p/\eta$ is the ratio between the particle diameter and the Kolmogorov length scale, $St_\eta$ is the Stokes number based on the Kolmogorov time scale, and $\Phi_M$ is the mass loading ratio. All parameters are based on turbulence properties at the centerline of the duct exit. The Kolmogorov scale was estimated from a TKE balance with the pressure term and dissipation term, yielding a cross-sectionally averaged value.

The maximum incident radiative power capable in the new configuration was increased from 1kW to 5kW. This maximum was lower than the nominal maximum power of the laser diode array of 10 kW due to breakage of a section of emitting chips, and eventual breakage of an entire line of diodes. Non-dimensional measures of the total radiative power are listed in Table 4.2 for the lower Reynolds number case with the maximum heating of 5 kW. The first parameter $\tau_{res}/\tau_{rad}$ is the ratio of the residence time in the heated section to the time taken for the particle temperature to approximately double due to radiative heating. The second parameter $\alpha = \frac{\gamma\tau_{eddy}\Phi_{th}}{\tau_{rad}}$ as defined in Pouransari and Mani (2017) is the ratio of the eddy time scale to time scale of increase in internal energy due to heating, where $\tau_{eddy}$ is the large eddy turnover time, $\gamma$ is the heat capacity ratio, $\Phi_{th}$ is the thermal capacity ratio between the disperse and carrier phase. Here $\tau_{eddy}$ is calculated as $\tau_{eddy} = H/u_{rms}$. The third parameter $R = \frac{P}{Nu_p\pi d_p k_f T_0}$ is the ratio of the radiative heating rate on the particle to the heat transfer rate from a particle to the gas per unit temperature difference, where $Nu_p$ is the particle Nusselt number, $d_p$ is the particle diameter, $k_f$ is the fluid thermal conductivity, and $T_0$ is a reference temperature. All of these dimensionless measures give an estimate of the radiative power relative to various quantities relevant to the heat transfer within the system.

| $\boldsymbol{Re_H}$ | $\boldsymbol{d_p/\eta}$ | $\boldsymbol{St_\eta}$ | $\boldsymbol{\Phi_M}$ |
|---|---|---|---|
| $10 \cdot 10^3$ | 0.10 | 4.4 | $0.40 - 2.1$ |
| $20 \cdot 10^3$ | 0.17 | 11.3 | $0.20 - 1.0$ |

Table 4.1: Table of non-dimensional parameters for the duct. $d_p/\eta$ is the ratio between the particle diameter and the Kolmogorov length scale, $St_\eta$ is the Stokes number based on the Kolmogorov time scale, and $\Phi_M$ is the mass loading ratio. The parameters are computed from cross-sectionally averaged values at the jet exit.

| $\boldsymbol{Re_H = 10000}$ | | |
|---|---|---|
| $\tau_{res}/\tau_{rad}$ | $\alpha$ | $\mathcal{R}$ |
| 5.5 | 7.9 | 0.23 |

Table 4.2: Table of non-dimensional parameters pertaining to total radiative power incident on system. $\tau_{res}/\tau_{rad}$ is the ratio of the residence time in the heated section to the time taken for the particle temperature to approximately double due to radiative heating. $\alpha$ is the ratio of the eddy time scale to time scale of increase in internal energy due to heating, and the third parameter $R$ is the ratio of the radiative heating rate on the particle to the heat transfer rate from a particle to the gas per unit temperature difference.

## 4.2 Flow Characterization

As the new configuration resulted in significant aerodynamic changes to the flow, the carrier phase statistics needed to be characterized. The purpose of this characterization was to ensure that the behavior of the flow was close to what the initial design aimed to do: a square jet with a co-flow velocity that matches its bulk velocity, which ideally mixes away most its non-uniformities by the time the flow reaches the measurement section further downstream. The purpose of these velocity measurements was not to obtain a detailed and exhaustive characterization of a relatively complicated flow for validation, but rather to ensure that the flow was behaving mostly as expected and is unlikely to be contributing to significant changes to the system behavior from the duct flow.

Mean velocity profiles of the unladen flow were first obtained at two different streamwise locations: just downstream of the exit of the jet at $x/H = 0.05$, and further downstream past the heated section at $x/H = 9$. The probe was traversed

in the radiation propagation direction (defined as $y$) along the jet exit bisector (at $z = 0$). The measurements were made for both Reynolds numbers; the measured mean velocity profiles are shown in Figure 4.1. At the jet exit, the center of the velocity profiles show the clear presence of a jet core exiting from the development section. Further away from the centers we see a mostly flat velocity profile from the bulk velocity-matched co-flow. At the intersection of these two regions, there is a region of significant shear due to the presence of boundary layers both on the inner and outer surfaces of the tapering development section wall. There is significant asymmetry between the boundary layer wakes at $y/H = +/-0.5$. This asymmetry is due to inadequate spatial resolution; the region of very low velocity downstream of the tapered channel wall is very thin. From the flow measurements, there is no evidence of the jet meandering or oscillating causing potential asymmetry. The jet was initially marginally misaligned with the co-flow, but the misalignment was fixed for all measurements shown. While at the jet exit the jet itself can be visually made out in the laden cases, it is quickly obscured by particles that spread beyond the jet. Far downstream at a streamwise distance of $x/H = 9$ from the jet exit, most of the non-uniformity in the mean velocity profiles has decayed away. The mean velocity has mostly mixed out to match the co-flow velocity, although weak velocity gradients are still present directly downstream of the channel walls. These gradients are more significant for the $Re_H = 20 \cdot 10^3$ case.

Velocity fluctuations measurements are needed to characterize the turbulence. Hot-wire anemometry described in Chapter 2 was used to obtain time-resolved, fast-response measurements of the unladen flow velocity. Shown in Figure 4.2 are velocity fluctuations at the same Reynolds numbers and streamwise locations as shown for the mean velocity. Near the exit of the jet, for both Reynolds numbers we can see significantly enhanced turbulent fluctuations associated with the interaction of the two merging boundary layers, which coincides with the location of significant mean gradients. The fluctuations in the co-flow are negligible in comparison. Far downstream, the fluctuations associated with these boundary layers have decayed away, and only weaker fluctuations associated with the core of the jet are still present. This is essentially the turbulence from the center portion of the duct carried downstream.

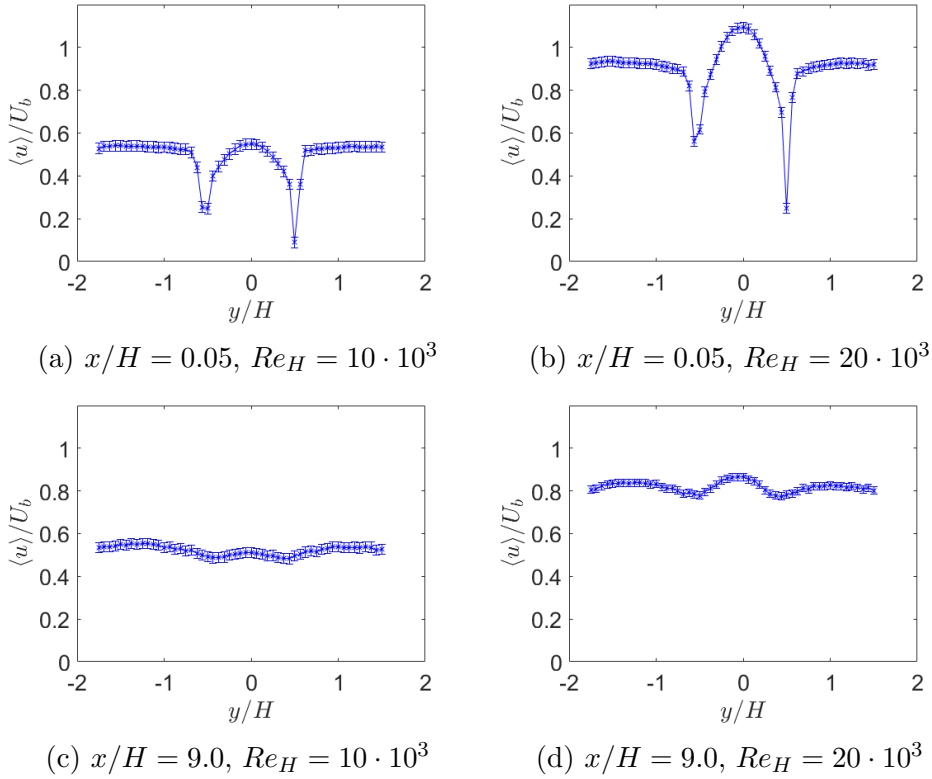


(a) $x/H = 0.05$, $Re_H = 10 \cdot 10^3$ (b) $x/H = 0.05$, $Re_H = 20 \cdot 10^3$

(c) $x/H = 9.0$, $Re_H = 10 \cdot 10^3$ (d) $x/H = 9.0$, $Re_H = 20 \cdot 10^3$

Figure 4.1: Mean unladen flow velocity profiles at two different streamwise locations.

In the co-flow, the fluctuations increase markedly approaching the outer wall of the facility. This is apparently due to the presence of turbulent boundary layers on the walls bounding the co-flow. The boundary layer turbulence is stronger on the negative y side; this is most likely caused by the presence of the cooled plates used to absorb any transmitted radiation. The cooled plates needed to be insulated from the plastic components surrounding to ensure the plastic did not deform or melt, and this was accomplished by placing insulating materials on the interface. The material used for insulation was under compression when fit into the assembly, and this sometimes caused a deformation of the insulation that could slightly jut out into the flow, potentially acting as a turbulent boundary layer trip.

For a more detailed characterization of the turbulence, velocity spectra were measured at a few select points in the flow. Shown in Figure 4.3 are velocity spectra for the same Reynolds numbers and streamwise locations. Three wall-normal coordinates

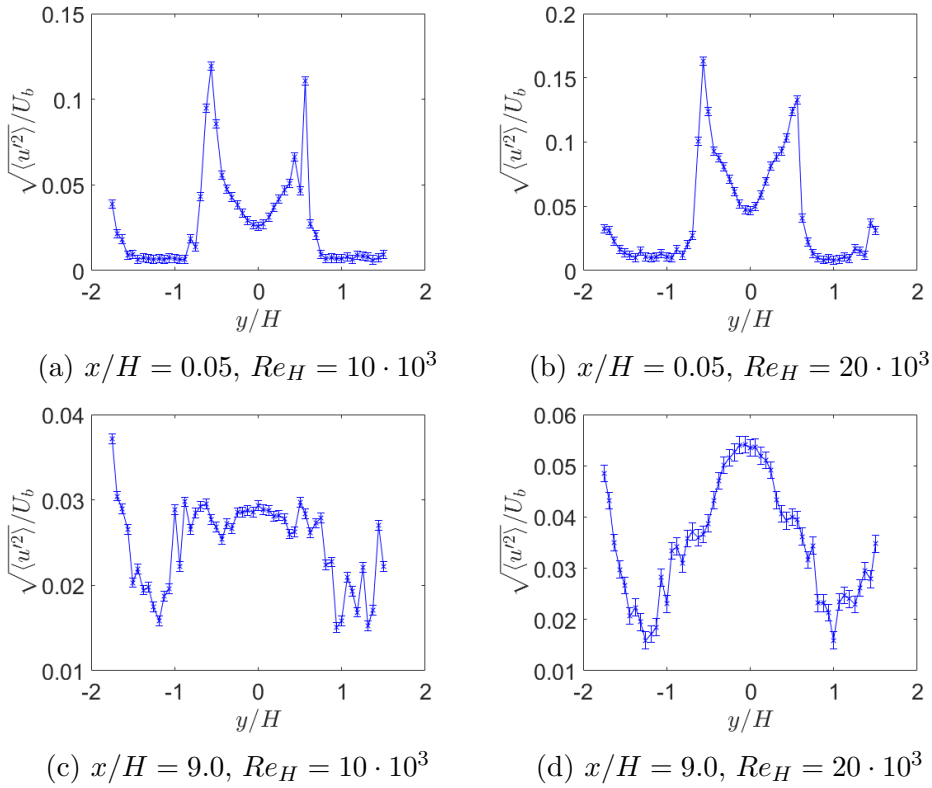


(a) $x/H = 0.05$, $Re_H = 10 \cdot 10^3$ (b) $x/H = 0.05$, $Re_H = 20 \cdot 10^3$

(c) $x/H = 9.0$, $Re_H = 10 \cdot 10^3$ (d) $x/H = 9.0$, $Re_H = 20 \cdot 10^3$

Figure 4.2: Unladen flow RMS velocity fluctations at two different streamwise locations for two different $Re_H$.

in the radiation propagation direction were chosen for the spectra measurements: at the jet center $y = 0$, in the co-flow towards the radiation source $y = 1.5$, and away from the radiation source $y = -1.75$ (note the flow was unladen and unheated for these measurements; radiation direction is mentioned mostly to orient the coordinate system). The frequency axis is non-dimensionalized by the bulk advection timescale $\tau_H$. The velocity spectra are mostly qualitatively similar for all cases, with the spectra spanning a wide range of scales. Much of the turbulent kinetic energy is contained in the large integral scales. The most notable difference between the spectra are in the lowest frequency components when comparing the jet center spectra to that of the co-flow: the co-flow regions seem to have all have enhanced low-frequency components. This could possibly be due to intermittent, large scale velocity fluctuations associated with the butterfly valve and the downstream blower driving the co-flow. In

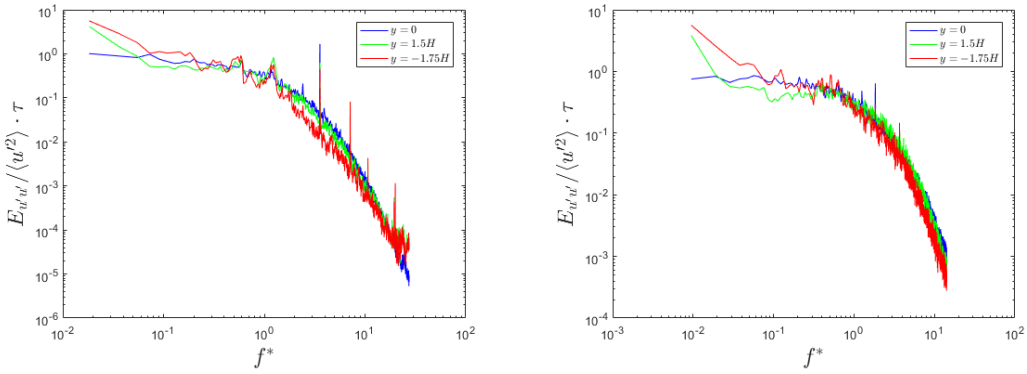


(a) $x/H = 0.05$, $Re_H = 10 \cdot 10^3$ (b) $x/H = 0.05$, $Re_H = 20 \cdot 10^3$

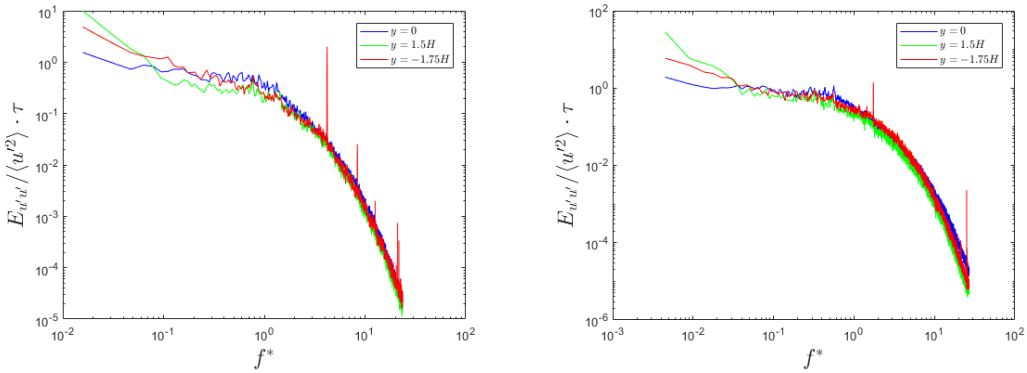


(c) $x/H = 9.0$, $Re_H = 10 \cdot 10^3$ (d) $x/H = 9.0$, $Re_H = 20 \cdot 10^3$

Figure 4.3: Unladen flow velocity spectra at two different streamwise locations, three different wall-normal locations, and two different $Re_H$. The frequency axis is normalized by the bulk advection timescale $\tau_H$.

the velocity fluctuation profiles seen earlier we see that the fluctuations start to rise slightly as we move deeper into the co-flow, which are likely caused by these slower but more intense low frequency fluctuations.

## 4.3 Mean temperature parameter scaling measurements

Once the velocity was fully characterized, heating was added to the laden flow. The aim of these measurements were to quantify the degree of heating present in the

system in the expanded parameter space of higher loading and heating, and to obtain broad, large-scale behaviors of the heat transfer. Similar to the duct case, a mean temperature traverse was performed using a fine-wire thermocouple probe, at the downstream location of $x/H = 9$. Figure 4.4a shows the mean temperature profile in the radiation propagation direction for the highest loading and heating case of $Re_H = 10 \cdot 10^3$, $\Phi_M = 2.1$, and $P = 5.0$ kW. As radiation propagates through the mixture from positive $y$, it is absorbed by the particles resulting in a rapid increase in the mean temperature rise with increasing depth into the medium. This sharp initial rise is slightly broadened by turbulent mixing. The temperature rise then peaks at approximately $y = 0.2$, then starts to decay with decreasing $y$. This is due to the attenuation of the radiation as it propagates through the medium, as particles encountering the radiation earlier have mostly absorbed or scattered the incident radiation. It is also worth noting the absolute value of the peak mean temperature rise in this flow of about 220 degrees, which is more than 5 times larger than any mean temperature rise measured in the duct configuration. The temperature rise at this location is large enough that variable property effects from temperature changes can potentially be altering the system behavior. To emphasize this point, Figure 4.4b shows the same data plotted on an absolute temperature scale normalized by the temperature upstream of any heating. A large decrease in mean density is expected in the hottest region surrounding $y/H = 0.2$. Furthermore, one must expect that the peak absolute temperature in dense particle clusters is considerably higher than the local mean.

While the mean temperature profile characterizes the large-scale absorption behavior throughout the flow in (physical) space, a parametric sweep can provide additional insight on how key driving parameters could be altering the system behavior reflected in the mean temperature rise. If any higher order effects significantly altered the radiation absorption and convective heat transfer, this could be reflected in the scaling of the mean temperature rise as a function of these parameters. Two key parameters were chosen for investigation: the mass loading ratio and the total incident radiative power. A fixed point in space at $x/H = 9$, $y/H = 0.2$, and $z/H = 0$ was chosen, as this location provided the largest mean temperature as indicated by the

mean temperature profile. The mass loading ratios, incident radiative powers, and Reynolds numbers swept through are summarized in 3.13.

Figures 4.5 show the temperature scaling behavior as a function of incident radiative power. The quantity on the y-axis is a non-dimensionalized scaling factor. It is a ratio between the temperature rise for each incident power normalized by a reference temperature rise, and the incident power normalized by the a reference incident power. The reference temperature is the temperature rise averaged across all powers at the given $Re_H$ and mass loading ratio, and the reference power is the average of all powers tested. This parameter should nominally be equal to 1 if the mean temperature rise scales linearly with incident power. Examining the value of this ratio across all the radiative powers tested, we see that the ratio is equal to one to within the measurement uncertainty. This indicates that the lowest order modeling assumption of the mean temperature rise scaling linearly with the incident power is an accurate assumption. Significant modification to the preferential concentration and turbulence from radiative heating on a bulk scale could be indicated by a change to this linear scaling, but this indicator was not observed in the mean temperature rise scaling.

A similar scaling comparison can also be performed by sweeping the mass loading ratio, examining the scaling behavior of the mean temperature versus the thermal capacity ratio rather than incident power. Even though the main parameter being altered is the mass loading ratio, the mean temperature rise is expected to scale linearly with the thermal capacity ratio rather than the mass loading ratio. This is because even though the radiative absorption scales linearly with the mass loading ratio, the thermal capacity of the air-particle mixture also increases with increasing mass loading, resulting in a slower-than-linear increase in the mean temperature rise in the mixture. The thermal capacity ratio $C$ is defined as:

$$C = \frac{\Phi_M c_{p,p}/c_{p,f}}{1 + \Phi_M c_{p,p}/c_{p,f}} \tag{4.1}$$

The quantity plotted in 4.6 shows the ratio of the mean temperature rise normalized by a reference mean temperature rise, and the thermal capacity ratio normalized

by a reference thermal capacity ratio. In these cases the reference temperature rise and thermal capacity ratio are the corresponding values at the lowest mass loading ratio for a given Reynolds number: for $Re_H = 10 \cdot 10^3$ it is $\Phi_M = 0.4$, and for $Re_H = 20 \cdot 10^3$ it is $\Phi_M = 0.2$. Like the scaling analysis done for incident radiative power, the plotted quantity should nominally be equal to one if the scaling of mean temperature rise was linear with the thermal capacity ratio. We see that the plotted ratio is close to one with some some spread for all cases, with some values deviating from one beyond the estimated uncertainty range. Given the strong linearity shown in the power scaling results, and the spread of these quantities both above and below the value of one, it seems unlikely that the deviation from linearity is caused by any changes induced by the heating, but is instead due to an uncaptured source of additional uncertainty. While a mean temperature profile for each case could have potentially elucidated the cause of additional uncertainty, due to the higher rate of particles loss in the co-flowing configuration, the larger mass loadings tested, and the large number of cases, mean temperature profiles were not obtained for every case.

## 4.4 Preferential concentration modification and turbulence modulation

The scaling results from the previous section show that the coupling between the radiation and the turbulence is not strong enough to cause a deviation from linear scaling arguments derived from simple one-dimensional models that do not account for turbulence or preferential concentration. However, changes could be still be occurring at the smaller cluster and turbulence scales which could point to a more subtle coupling, that cannot be captured from the mean temperature alone. In order to probe these more specific changes, an examination of the effect of heating on changes to the preferential concentration and turbulence statistics was performed. For the results shown in this section, the mass loading and incident radiative power were fixed to the highest values of $\Phi_M = 2.1$ and $P = 5.0$ kW, at $Re_H = 10 \cdot 10^3$. The measurements were made using a PIV system, with the laser sheet illuminating the

flow field centered at a wall-normal coordinate of $y/H = 0.21$ (wall-normal location of highest temperature rise) and $z/H = 0$, streamwise location of $x/H = 9.4$, and a square imaging region with a width of $H/2$. Three measures of preferential concentration were examined: the radial distribution function (RDF), the clustering index, and Voronoi tesselation area PDFs. To study the effects of turbulence modification, particle velocity statistics were also obtained. To isolate the effect of the radiative coupling, comparisons of these statistics were made with and without heating at equivalent loading and flow conditions. The statistics were computed by obtaining 2000 images of the flow, and were pre-processed with background subtraction, median filtering, contrast adjustment, thresholding, binarizing, morphological opening, and finally centroid computation in order to determine particle positions.

### 4.4.1 Radial distribution function

The first statistic examined was the RDF. The RDF is one of the most commonly used descriptors of preferential concentration and particle distribution, due to its importance in determining collision rates and its relation to the two-point number density correlation. The radial distribution function $g(r)$ is defined as the probability of finding a particle pair at a separation distance $r$, normalized such that a Poisson-distributed field of particles yield a value of one. Figure 4.7a shows the RDF for the particles in the flow without any heating and in the presence of maximal possible heating in the experiment. Figure 4.7b shows this same result but with the maximum and minimum bounds observed for each case among independently acquired batches of data, with each batch containing 500 images sampled over a duration of about a minute, with 4 total batches obtained totalling 2000 images gathered. We see from these plots that the RDF is not globally equal to one, confirming that the flow is preferentially concentrated in this region with and without heating. The RDF rises as we approach a separation distance of zero, indicating that particles are more likely to be found at small separations due to clustering. While it is not possible to resolve with our current experiment, the RDF is expected to drop to below one if the separation distance becomes small enough to approach the particle diameter scale.

As we move to large separations, the RDF asymptotes to a value of one.

Comparing the two lines, we see that the value of the RDF is smaller for the heated case until a cross-over point, where it then becomes larger than the unheated case. This result is significant as it is the first evidence that the radiative heating is causing a change in the preferential concentration of the particles. When the particles are irradiated, they are less likely to be found at smaller separations, and more likely to be found at larger separations, indicating reduced clustering at smaller scales. The larger change in clustering at smaller scales is consistent with our expectations, as the densest clusters with the smallest separation distances are likely to be the most intensely heated due to increased radiation absorption. It is worth noting that this measurement of the RDF is subject to a few biases. The first is that the images obtained are a 2D projection of the 3D field illuminated by the laser sheet, as the laser sheet as a finite thickness. This can bias separation distances that are smaller than the laser sheet thickness. This projection can also cause overlapping of particle images, causing the particle detection algorithm to perceive distinct but overlapped particles as a single particle, further biasing the measurements at smaller separations. Additionally, the RDF does not account for anisotropy in the particle distribution; while it averages the pair detection probability in all directions in the measurement plane, it does not capture the contribution to the RDF in the radiation-parallel direction. While these biases may cause deviations from the true RDF in the flow, it is expected to bias the results in both the heated and unheated cases in the same manner. Therefore, we believe the observation of reduced clustering at the smaller scale with the addition of heating is a real effect, not a measurement artifact.

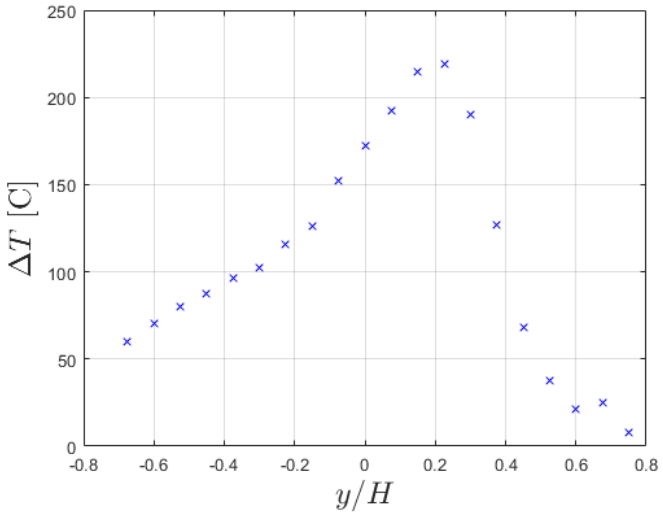


(a) Dimensional mean temperature rise at $Re_H = 10 \cdot 10^3$, $\Phi_M = 2.1$, and $P = 5.0$ kW, traversed in the radiation propagation direction at a streamwise location of $x/H = 9$.

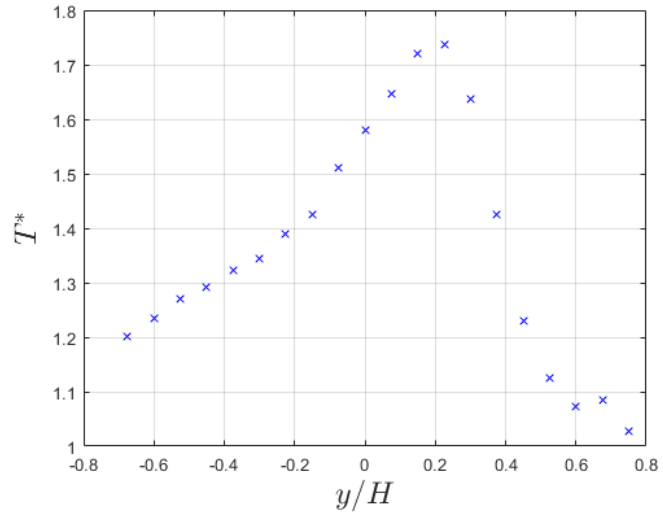


(b) Non-dimensional absolute temperature normalized by unheated upstream temperature at $Re_H = 10 \cdot 10^3$, $\Phi_M = 2.1$, and $P = 5.0$ kW, traversed in the radiation propagation direction at a streamwise location of $x/H = 9$.

Figure 4.4: The mean temperature profiles at the highest loading and heating case, dimensional and non-dimensional.

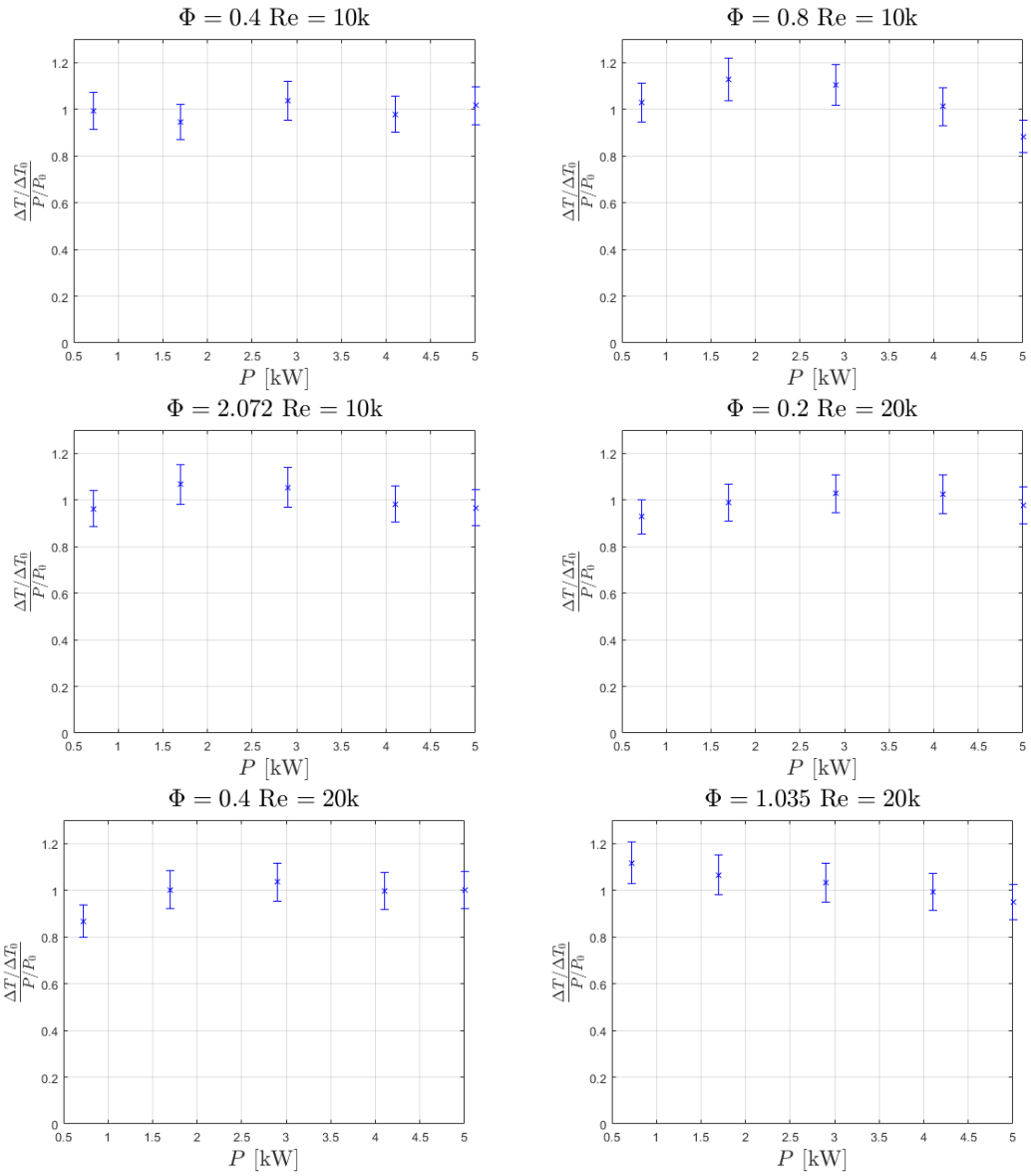


Figure 4.5: Mean temperature rise scaling versus incident radiative power, for different mass loading ratios and Reynolds numbers. A value of one indicates linear scaling between the mean temperature rise and incident radiative power.

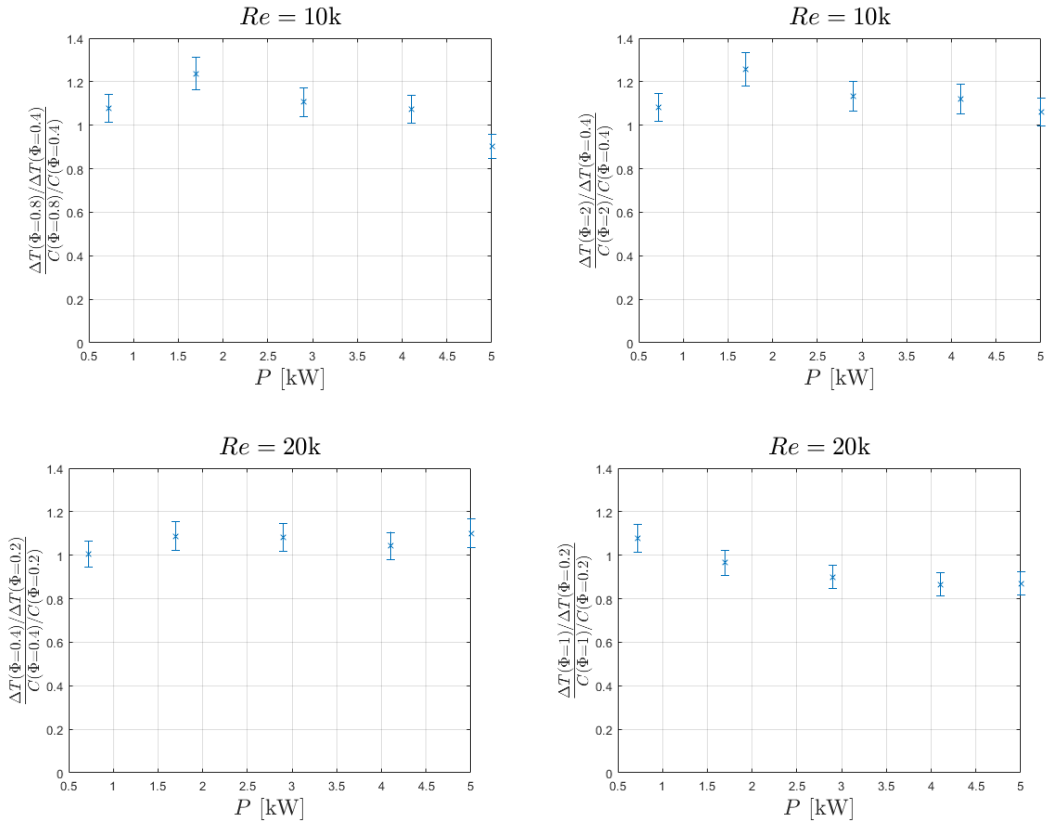


Figure 4.6: Mean temperature rise scaling versus thermal capacity ratio $C = \frac{\Phi_M c_{p,p}/c_{p,f}}{1+\Phi_M c_{p,p}/c_{p,f}}$, for different incident radiative powers and Reynolds numbers. A value of one indicates linear scaling between the mean temperature rise and thermal capacity ratio.

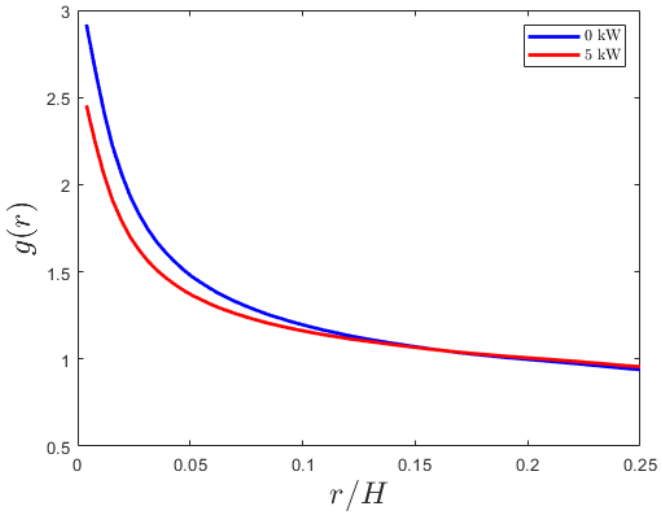


(a) Radial distribution function $g(r)$ comparisons with and without radiative heating. Particle separation distance $r$ is normalized by the duct width $H$.

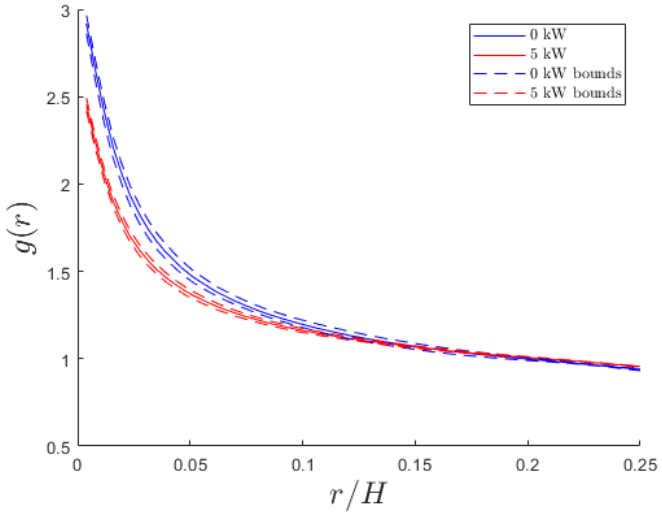


(b) Radial distribution function $g(r)$ comparisons with and without radiative heating. The solid line is the RDF averaged over all independent measurement batches, while the dotted line shows the minimum and maximum values observed across all batches.

Figure 4.7: Radial distribution function $g(r)$ comparisons with and without radiative heating.

### 4.4.2 Clustering index

Another statistic often used to quantify preferential concentration is the clustering index (CI), a box-counting method first proposed by Eaton and Fessler (1994). To compute this quantity, the measurement domain is divided into boxes of width $\delta$, and the statistics of the number of particles in each box are measured for different $\delta$. The CI for a given box size $\delta$ is then defined to be the difference between the standard deviation of the number of particles in a box and the standard deviation of particles in a box from particles distributed with a Poisson process, normalized by the mean number of particles per box:

$$D(\delta) = \frac{\sqrt{\langle N_p' \rangle_\delta} - \sqrt{\langle N_{p,Poiss} \rangle_\delta}}{\langle N_p \rangle_\delta} \tag{4.2}$$

Similar to the RDF, the CI can quantify the degree of preferential concentration across different length scales by varying the box width $\delta$. A preferentially concentrated particle field will tend to have boxes with more particles than that of a Poisson distributed field when sampling a cluster, or boxes with fewer or no particles when sampling a region devoid of particles, resulting in a non-zero CI. In a preferentially concentrated particle field the CI tends to zero as the box width approaches zero, as the number of particles per box becomes too small and the Poisson variability arising from the finite number of particles dominate the variability due to preferential concentration (Banko, 2018). As the box width gets larger, the CI also eventually tends to zero as a single box can now encompass entire clusters and voids.

Figure 4.8a shows a comparison of the CI between the heated and unheated cases, and Figure 4.8b show minimum and maximum values of the CI observed across independent batches of measurements. These results again confirm that the flow is preferentially concentrated, as the value of the CI is non-zero. With the addition of heating, we can also see that the value of the CI decreases for all length scales examined in the analysis. This indicates a reduction in the preferential clustering across all the length scales examined with the CI. This result is consistent with what

was observed in the RDF, which also indicated reduced clustering at scales ranging from $\delta/H = 0.01 - 0.1$.

The CI is subject to similar biases as the RDF, in that it obtained from a 2D projection from a 3D space illuminated by the laser sheet, and suffers from the attenuation at small separations due to particle overlap. In addition, it is sensitive to the number of particles in the measurement domain. To control for finite particle effects, the number of particles in each image was downsampled to the same number of particles for all images analyzed.

### 4.4.3 Voronoi tesselation

The final statistic of preferential concentration examined in this section is Voronoi area PDFs. Voronoi decomposition has been used in the literature to identify cluster and void regions of the flow (Monchaux et al., 2012), and the same method is applied here. Voronoi tesselation divides up a domain into Voronoi cells, where each cell is centered at the particle location. All other points in the cell are closer to the particle location in the cell than any other particle, and the edges of the cell become equidistant from nearby particle pairs. This results in the domain being broken up into many cells, with small cells surrounding particles in clusters, and large cells surrounding particles in void regions. Figure 4.9 shows the tesselation performed on a preferentially concentrated particle field.

Once the particle field has been decomposed into Voronoi cells, PDFs of the cell areas can be computed. Figure 4.10a shows the area PDFs computed with and without heating, with the area PDF arising from a Poisson distributed field included as well for comparison. The area $A$ is normalized by the mean cell area $\langle A \rangle$. We can see that both heated and unheated PDFs have been shifted from the Poisson PDF. In the preferentially concentrated particle field, there is increased probability of finding very small Voronoi cells in highly dense particle clusters, as well as increased fraction of very large cells in regions devoid of particles. A cluster cell can be defined by designating all cells with areas smaller than the left intersection point between the Poisson PDF and that of the preferentially concentrated field belonging to a

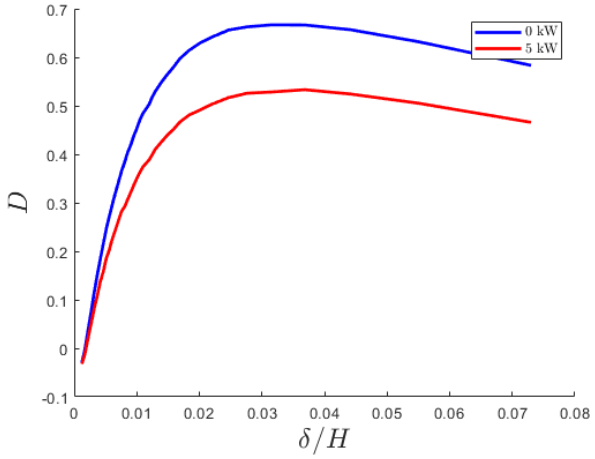


(a) Clustering index $D$ comparisons with and without radiative heating. Box size $\delta$ is normalized by the duct width $H$.

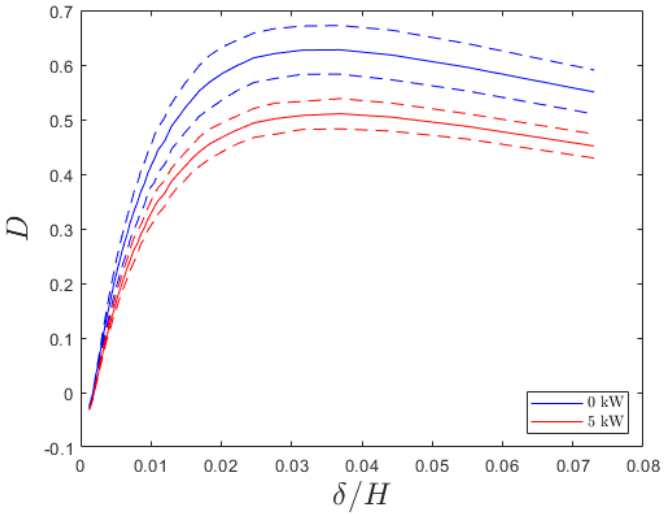


(b) Clustering index comparisons with and without radiative heating. The solid line is the CI averaged over all independent measurement batches, while the dotted line shows the minimum and maximum values observed across all batches.

Figure 4.8: Clustering index $D$ comparisons.

cluster, and all cells with areas larger than the right intersection point between the Poisson PDF and that of the preferentially concentrated field as belonging to a void

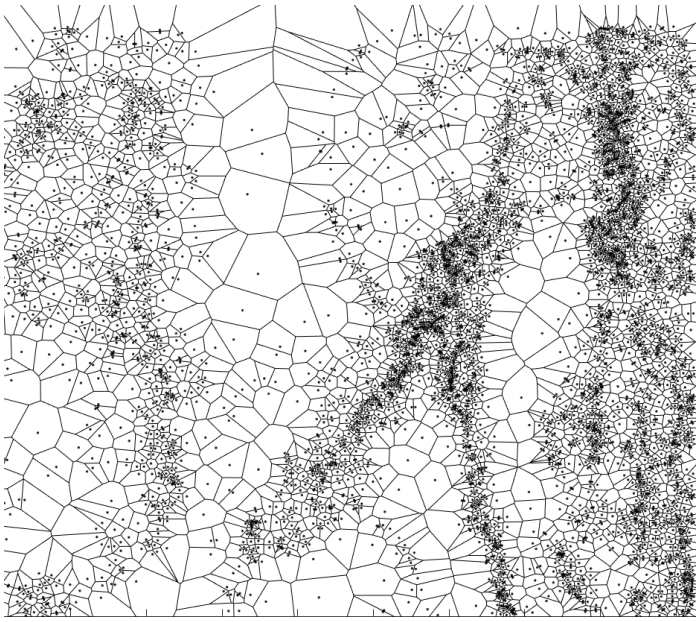

Figure 4.9: An example of a particle field decomposed into Voronoi cells.

(Monchaux et al., 2012).

Comparing the cluster area PDFs between the heated and unheated cases using the aforementioned definitions, we see that there is redistribution of the cell area as heating is added into the flow. There is a decreased fraction of cluster cells as heating is added, and this is more prominent for the smallest cluster cells. There is a crossover point in the cluster regime at which we find more cells in the heated case than the unheated case. This increased fraction of cells in the heated case continues as we move into intermediate cell sizes and eventually the void cell sizes as well. This result is again consistent with what was seen in previous measures of preferential concentration: we see that clustering is reduced at the smallest scales, as the clusters are the densest at these scales and the heating is the most intense. There is a redistribution of length scales in the clustering, with a slight net shift towards reduced overall clustering.

Vornoi area PDFs can also provide additional insight into the structure of clusters if we look at the joint PDF of cluster concentration and area. Constraining the analysis to just the cells that are in a cluster, we can examine changes in the cluster

density with the addition of heating, as seen in Figure 4.10b. Here $C$ is defined as the number of particles in a cluster divided by the cluster area, normalized by $C_0$, the number of particles in the full image divided by the image area. As heating is introduced, we see a shift in the cluster density PDF towards lower densities, which is consistent with the previous results: there is not only reduced clustering at the smallest scales, but also decreased densities of clusters.

The three different measures of preferential concentration all paint a consistent picture: when sufficient heating is introduced into the system, there is an overall reduction in preferential clustering, which is most strongly displayed at the smallest scales due to the most intense heating present at these scales. The reduction in clustering occurs through a reduction in the densities of the clusters. Three possible mechanisms are hypothesized to be contributing to these changes: dilatational effects arising from the reduction in carrier phase density in strongly heated clusters, buoyancy effects from carrier phase density changes, and variable property effects due to temperature dependent flow properties.

Out of these mechanisms possibly active in the system, dilatational effects seem to be the most likely in explaining the observed changes in the preferential concentration. The densest clusters experience the largest temperature rise, causing the largest change in the density of the local fluid surrounding the cluster. This change in density causes the fluid to locally expand, which can cause the particle separations to become larger at the cluster scales. A simple analysis can be performed to estimate a velocity associated with this expansion. Take a sphere of a fluid-particle mixture with a diameter associated with the preferential concentration length scale (e.g. length scale associated with an exponential fit from the RDF, equal to approximately 0.8 mm), at a volume fraction 5 times higher than the mean volume fraction, heated for a duration equal to the residence time of the flow in the heated section. We then make the following assumptions:

- The fluid temperature responds instantaneously to changes to the particle temperature.
- The volume of fluid in the sphere is much larger than the volume of particles.

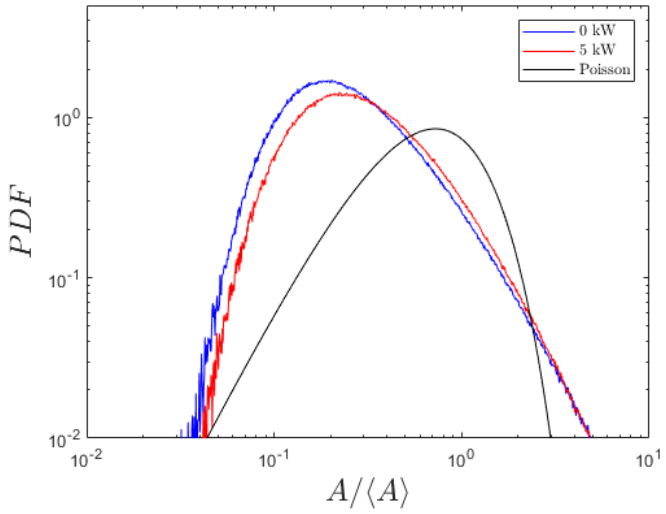


(a) Voronoi cell area PDFs, comparing cases with heating, without heating, and that from a Poisson distribution. The cell area $A$ is normalized by the mean cell area $A/\langle A\rangle$.

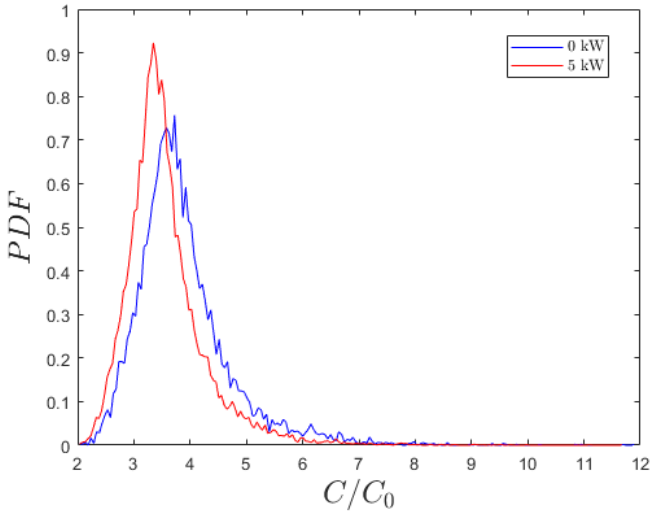


(b) Voronoi cell cluster density PDFs, comparing cases with and without heating. $C$ is defined as the number of particles in a cluster divided by the cluster area, normalized by $C_0$, the number of particles in the full image divided by the image area.

- For computing the radiation absorption, we use Beer's Law but assume the medium is a cylinder with length and diameter euqal to that of the sphere.

We can then perform a simple energy balance to obtain an estimated temperature rise in this heated sphere:

$$Q_{abs}A_{pc}I = \frac{(\rho_p c_{p,p} V_p n V_s + \rho_f c_{p,f} V_s)\Delta T}{dt} \tag{4.3}$$

where $Q_{abs}$ is the particle absorption efficiency, $A_{pc}$ is the particle absorption cross-section, $I$ is the absorbed radiative flux, $\rho_p$ and $\rho_f$ are the particle and fluid densities, $V_p$ and $V_s$ are the volumes of the particles and the sphere, $c_{p,p}$ and $c_{p,f}$ are the particle and fluid specific heats, and $dt$ is the residence time. We also obtain the radiation absorption $I$ from Beer's Law:

$$I = I_0 exp(-Q_{abs}A_{pc}nl) \tag{4.4}$$

where $n$ is the particle number density and $l$ is the hypothetical cylinder length. From mass conservation, we can then estimate the outward dilatational velocity:

$$u_{dil} \approx \frac{1}{\rho_0}\frac{d\rho}{dt}l \tag{4.5}$$

This velocity value is estimated to be approximately $u_{dil}/U_b = 0.007$, which about a fourth of the streamwise RMS velocity of the unladen flow at the downstream center region of the test section. This demonstrates that the velocity associated with dilatational effects are large enough to make small but measurable changes to the preferential concentration.

### 4.4.4 Turbulence modulation

In the previous section, we observed changes to the preferential concentration induced by radiative heating. The heating of the particles alone cannot induce these changes in the preferential concentration; it is rather the changes induced in the surrounding carrier phase flow by the convective heat transfer from the particles to the carrier phase that are causing these observed effects. More specifically, it is the modulation of the turbulence that modifies the preferential concentration, as it has been shown that

the underlying turbulence in the carrier phase is strongly correlated to the clustering behavior of particles. The present study unfortunately was not able to directly probe the statistics of the carrier phase turbulence, as the combination of a heated flow and a high concentration of particles resulted in an environment that made directly probing the turbulence statistics difficult without either significant alterations to the experimental apparatus, or development of a new measurement technique. Instead we approach this problem by first looking at the particle velocity statistics since they are directly measurable with the PIV system and are related to the gas phase turbulence. We then perform simple scaling analyses to compare the relevant time scales of mechanisms that might be modulating the turbulence, and isolate the presence of these different mechanisms via an examination of directional clustering statistics.

Two-component particle velocity statistics were obtained using PIV, from the same data set used for to quantify the preferential concentration. The velocity statistics were averaged along the streamwise direction in the 2-D measurement domain, which extended from $x/H = 9.2$ to $x/H = 9.6$. Figure 4.11 shows the mean streamwise particle velocities after the heated section, at the same measurement location as the preferential concentration statistics. We see that as the flow is heated, the mean streamwise velocity increases. This is due to the reduction in density caused by the heating, which results in an acceleration of the flow following from mass conservation. This provides the most concrete evidence the density of the flow is being changed, and significantly enough to observe changes in the bulk flow. In the measurement domain, the streamwise particle velocity is also observed to be uniform; if the measurement domain was rotated 90 degrees to align with the radiation direction, it is possible that mean particle velocity gradients would be present. Note that the measurement window covers only the central region of the flow, so it is not known if the co-flow also accelerates. However, it seems likely that the acceleration extends across the entire co-flowing duct since the observed acceleration is only 2.6%.

Figure 4.12 shows the particle velocity RMS, in the streamwise and wall-normal (radiation normal) directions. The first notable feature of the velocity fluctuation profiles is the slight asymmetry of the fluctuations in a nominally symmetric flow. This is possibly due to two effects: first is slight asymmetry of the jet itself. All

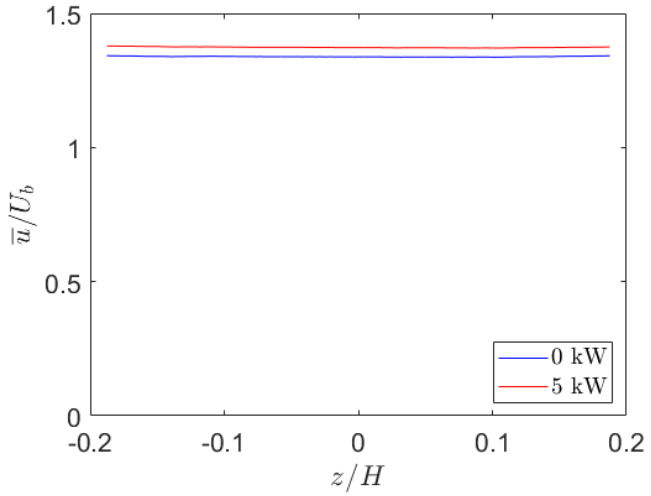


Figure 4.11: Mean streamwise particle velocities after the heated section, normalized by the bulk velocity $U_b$. Particle velocities with and without radiative heating are compared.

the velocity characterization measurements were performed in the y-direction, and rotational symmetry was simply assumed. Slight misalignments could potentially have a more pronounced effect in the far downstream measurement location, which would not be captured in a y-direction traverse. An alternative possibility is biasing due to laser sheet attenuation; the particle number density is high enough at the tested mass loadings such that the laser sheet gets attenuated by a non-negligible amount. This would bias smaller particles to be less likely to be captured by the camera with decreasing $z$, biasing the sampling of particles depending on the z-coordinate of the imaging region.

The more interesting feature of these results is the change that occurs with heating: the particle velocity fluctuations are reduced both in the streamwise and wall-normal directions as heating is introduced into the flow. This was contrary to initial expectations, as both effects of buoyancy and dilatation were hypothesized to intensify the turbulence, which would result in an increase in the particle velocity fluctuations. Buoyancy effects could intensify the turbulence by the generation of buoyant plumes at various cluster scales from local cluster heating, which would increase turbulent fluctuations. Local dilatation of the fluid could also increase turbulent fluctuations:

Pouransari and Mani (2017) found that particle heating can introduce additional turbulent kinetic energy through the pressure-dilatation term, and this can occur through changes in the dilatational modes of the velocity field.

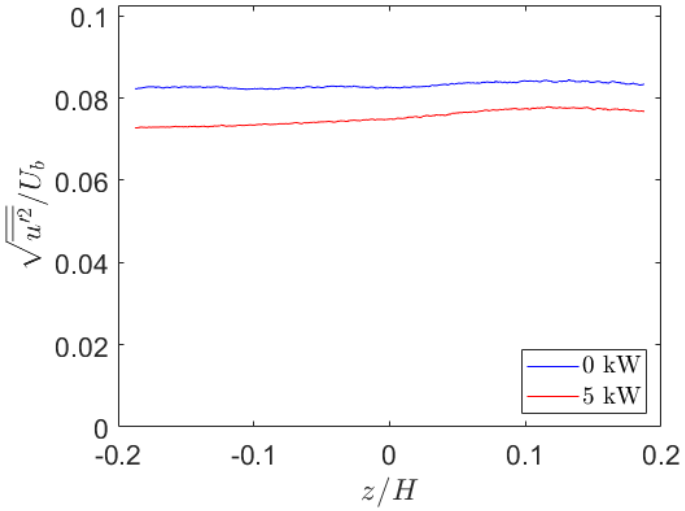


(a) Streamwise particle velocity fluctuation RMS after the heated section.

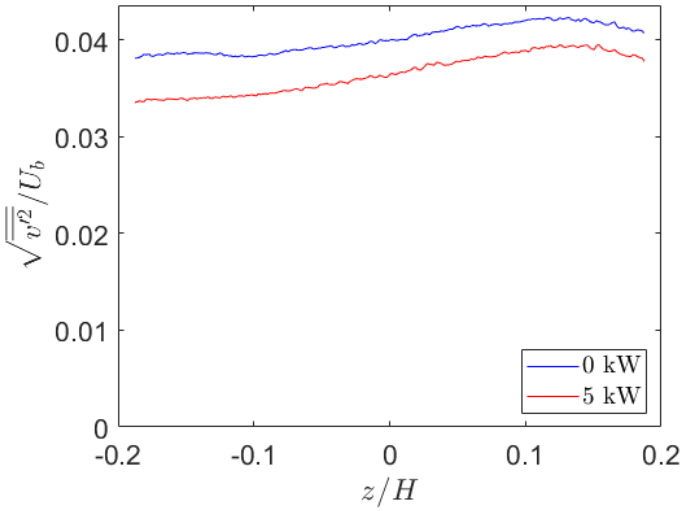


(b) Wall-normal (and radiation-normal) particle velocity fluctuation RMS after the heated section..

Figure 4.12: Particle velocity fluctuation RMS after the heated section.

What is likely happening is a different mechanism for turbulence modulation, via temperature-dependent variable property effects. Using the maximum mean temperature rise observed at the measurement location, we can estimate the changes in particle properties, listed in Table 4.3. The ratios from the table show a significant enough increase in the kinematic (and dynamic) viscosity to cause measurable changes to the turbulence. More specifically, the increased viscosity is likely enhancing the dissipation occurring at the smallest scales, which explains the dampening of the turbulence observed in the reduction of the particle velocity fluctuations. It is difficult to make any more conclusive statements on how the property changes are modulating the turbulence without direct measurements of the carrier phase, but the results seem to indicate that these variable property effects have the greatest effect in introducing large-scale, bulk changes to the flow, while the dilatation and buoyancy effects are likely inducing smaller, local changes in the turbulence that do not strongly manifest in the bulk properties of the flow in the current parameter space.

| $T/T_0$ | $\rho/\rho_0$ | $\mu/\mu_0$ | $\nu/\nu_0$ |
|---|---|---|---|
| 1.64 | 0.60 | 1.5 | 2.6 |

Table 4.3: Table of the ratio of estimated particle property changes at the location of maximal temperature rise, compared to properties at the unheated temperature.

As measurements of the carrier phase are not feasible to probe the details behind how these mechanisms might be modulating the turbulence, a scaling analysis was performed to further investigate the effects of dilatation and buoyancy effects. Given the limited information available on the carrier phase statistics, the purpose of this analysis was to compare the time scales at which distortions of turbulent structures could be occurring, and to compare them to the time scales of turbulence to determine if these effects could feasibly be affecting change in the flow. Using continuity and the transport equation for thermal energy, we can obtain characteristic velocities for dilatational and buoyancy effects:

$$u_{dil} = l_{clust}\frac{U_b}{L}T^* \qquad u_{buoy} = \sqrt{gT^* l_{clust}} \tag{4.6}$$

where $l_{clust}$ is a chracteristic clustering length scale, $T^*$ is the non-dimensional temperature rise and $g$ is the gravitational acceleration. Using these characteristic velocities and a clustering length scale, we can also obtain characteristic time scales associated with these effects:

$$t_{dil} = l_{clust}/u_{dil} \qquad t_{buoy} = l_{clust}/u_{buoy} \tag{4.7}$$

With these time scales obtained, we can compare these timescales to a variety of time scales associated with the turbulence. The full comparison is shown in Figure 4.13. The ratios of most interest are those that compare the buoyancy and dilatation times at the cluster scales to the large and intermediate eddy turnover times, as these scales provide a measure of the rate of evolution of turbulence at the integral and inertial ranges. Table 4.4 isolates these parameters from the larger table. We find that these ratios are mostly $\mathcal{O}(1) - \mathcal{O}(10)$, indicating that these processes are occurring at similar time scales, allowing for the possibility for these effects to feasibly be modulating the turbulence. Even for the ratio furthest from unity ($t_{eddy,l}/t_{buoy} = 17$), the value is still larger than one; this implies that the turbulence at the integral scales is evolving slower than the changes caused by buoyancy, which allows for the faster buoyancy effects to still modify the turbulence at those scales. While this analysis does not provide direct evidence of these mechanisms modulating the turbulence, it allows us to not rule out any of these effects due to a large separation of scales.

| $\boldsymbol{t_{eddy,l}/t_{buoy}}$ | $\boldsymbol{t_{eddy,\lambda}/t_{buoy}}$ | $\boldsymbol{t_{eddy,l}/t_{dil}}$ | $\boldsymbol{t_{eddy,\lambda}/t_{dil}}$ |
|---|---|---|---|
| 17 | 3.6 | 3.6 | 0.78 |

Table 4.4: Key time scale comparisons isolated. $t_{eddy,l}$ is the large eddy turnover time, $t_{eddy,\lambda}$ is the intermediate eddy turnover time, and $t_{buoy}$ and $t_{dil}$ are the characteristic buoyancy and dilatation time scales at the cluster scales respectively.

| | **Residence time** $t_{res} = \frac{L}{U_b}$ $= 0.040$ s | **Radiation time** $t_{rad} = \frac{\rho_p c_{p,p} V_p}{Q_{abs} A_{pc} I_o}$ $= 0.0073$ s | **Thermal relaxation time** $t_{th} = \frac{\rho_p c_{p,p} V_p}{h_p A_p}$ $= 0.031$ s | **Momentum relaxation time** $t_{mom} = \frac{\rho_p d_p^2}{18\mu}$ $= 0.0040$ s | **Buoyancy time (cluster scale)** $t_{buoy,l} = \frac{l_{clust}}{u_{buoy,l}}$ $= 0.012$ s | **Buoyancy time (integral scale)** $t_{buoy,L} = \frac{L}{u_{buoy,L}}$ $= 0.00093$ s | **Dilatation time** $t_{dil} = \frac{l_{clust}}{u_{dil}}$ $= 0.055$ s | **Large eddy turnover time** $t_{eddy,l} = \frac{H}{u_{rms}}$ $= 0.2$ s | **Intermed. eddy turnover time** $t_{eddy,\lambda} = \frac{\lambda}{u_{rms}}$ $= 0.043$ s | **Kolmog. time** $t_\eta = \left(\frac{\nu}{\epsilon}\right)^{0.5}$ $= 9.6 * 10^{-4}$ s |
|---|---|---|---|---|---|---|---|---|---|---|
| $t_{res}$ | | 5.48 | 1.29 | 10 | 3.3 | 42.4 | 0.73 | 0.2 | 0.93 | 41 |
| $t_{rad}$ | 0.18 | | 0.24 | 1.8 | 0.61 | 7.7 | 0.13 | 0.037 | 0.17 | 7.6 |
| $t_{th}$ | 0.78 | 4.2 | | 7.8 | 2.6 | 33 | 0.56 | 0.16 | 0.72 | 32 |
| $t_{mom}$ | 0.1 | 0.55 | 0.13 | | 0.33 | 4.2 | 0.073 | 0.02 | 0.093 | 4.2 |
| $t_{buoy,l}$ | 0.3 | 1.64 | 0.39 | 3 | | 13 | 0.22 | 0.06 | 0.28 | 13 |
| $t_{buoy,L}$ | 0.024 | 0.13 | 0.030 | 0.24 | 0.079 | | 0.017 | 0.0047 | 0.022 | 0.98 |
| $t_{dil}$ | 1.4 | 7.5 | 1.8 | 14 | 4.6 | 58.3 | | 0.28 | 1.3 | 57 |
| $t_{eddy,l}$ | 5 | 27 | 6.5 | 50 | 17 | 210 | 3.6 | | 4.7 | 210 |
| $t_{eddy,\lambda}$ | 1.1 | 5.9 | 1.4 | 11 | 3.6 | 16 | 0.78 | 0.22 | | 45 |
| $t_\eta$ | 0.024 | 0.13 | 0.031 | 0.24 | 0.08 | 1.0 | 0.018 | 0.0048 | 0.022 | |

Figure 4.13: A table of time scale comparisons. The numbers in the tables are the ratio of the quantity in the column, divided by the quantity in the row.

### 4.4.5 Directional measures of preferential concentration

The previous analyses showed evidence of preferential concentration modification, but did not necessarily provide evidence for a specific mechanism causing the changes. A different analysis is hence proposed to try to isolate the presence of either buoyancy or dilatation effects, through directional measures of preferential concentration. Effects of buoyancy are expected to manifest predominantly in the gravity-parallel (streamwise) direction, while dilatational effects should cause changes in both streamwise and wall-normal directions. The clustering index is re-examined for this purpose, with the box-counting now performed in one dimension along long bins with thickness $\delta$, rather than square boxes with side length $\delta$.

Figure 4.14 shows the directional clustering indices with and without radiative heating, with the streamwise CI's plotted with crosses and wall-normal CI's plotted with circles. The first feature to note is that when heating is introduced, the CI's in the wall-normal direction are reduced for all length scales examined. This indicates that dilatational effects are modifying the preferential concentration, as buoyancy effects in the wall-normal direction would be minimal. It also confirms the earlier hypotheses that local dilatiation caused by heating is reducing the preferential concentration at the cluster scales. Examining the streamwise CI's, we see that the CI is also modified in the streamwise direction, to a greater extent than the wall-normal direction. While it is not possible to fully decouple the contributions from buoyancy and dilatational effects to this change, if we assume a similar contribution from the dilatational effects in the streamwise direction as we saw in the wall-normal direction, the remaining contribution to these changes are likely from buoyancy effects, which would confirm that buoyancy effects are also contributing to changes in the preferential concentration.

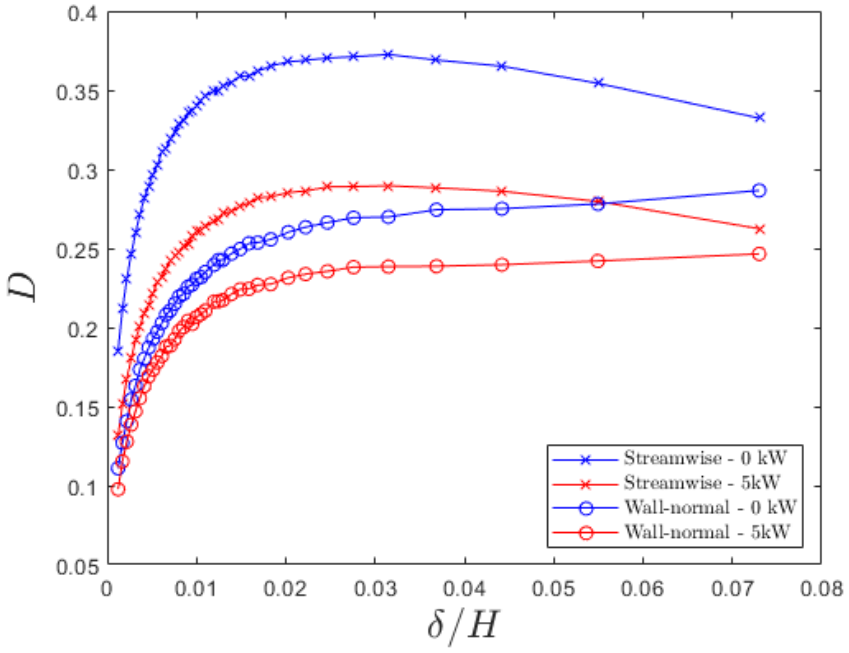


Figure 4.14: 1-D directional clustering indices obtained by binning the domain in bins of width $\delta$ in their respective directions, rather than a 2-D box. Red lines are the CI's with heating, and blue lines are CI's without heating. Circles are the directional CI's in the wall-normal direction, and crosses are CI's in the streamwise direction

# Chapter 5

# Conclusions and future work

This work experimentally examined the effect of radiative heat transfer on absorbing, particle-laden turbulent flows, and the coupling between the different physical processes present in such a system. This multi-physics system is relevant to understanding a variety of natural phenomena and engineering processes, but the primary motivating case was the particle solar receiver. A key aspect of particle-laden turbulent flows that was not explored in previous studies of particle solar receivers was the phenomenon of preferential concentration (which refers to the behavior of particles preferentially clustering in turbulent flows based on the flow topology), and the potential effects of such clustering on the system behavior. The aim of this work was to therefore study the effect of preferential concentration on relevant system quantities such as radiation transmission and convective heating to the carrier phase. An additional objective was to further explore the full two-way coupling by studying the reverse effects, by examining how radiative heating modified the preferential concentration and the turbulence statistics of the carrier phase.

To accomplish these goals, an experimental apparatus was designed to study these effects. The wind tunnel facility used for the experiments generated a fully-developed, turbulent square duct flow, which could be joined with two different test section configurations. The first configuration used was a continuation of the square duct flow from the development section, while the second configuration had the duct flow from

the development section eject into a velocity-matched co-flow, generating a co-flowing, isokinetic square jet. In both test sections the particle-laden flow was irradiated with radiation generated from a laser-diode array, and the heated mixture was studied using a variety of instrumentation. Particle positions, carrier phase velocity and temperature, and radiation transmission were measured to characterize the turbulence, radiation transport, and preferential concentration in the system. The test section configuration was altered from the initial duct configuration to the co-flowing jet configuration due to limitations on the radiative power and mass loading that could be tested in the duct, and to remove the effects of heating from the wall.

## 5.1 Conclusions

The main conclusions of the work are summarized below:

- Measurements of mean radiation transmission made with the photodiode in the duct configuration showed sub-exponential attenuation of the radiation, demonstrating a deviation from Beer's Law. This was due to the preferential concentration present in the absorbing medium, which created longer line-of-sight distances in the medium, resulting in more radiation transmission and reduced absorption compared to a Poisson distributed medium.

- Measurements of radiation transmission fluctuations made with the photodiode in the duct configuration showed increased transmission variance with optical depth, due to the radiation passing through progressively larger numbers of clusters that absorbed or scattered radiation. The transmission spectra showed that the fluctuations were broadband, with fluctuations dominated by the largest structures with implied length scales of $\mathcal{O}(0.1H) - \mathcal{O}(H)$.

- The carrier phase mean temperature and temperature fluctuations in the duct measured with the fine-wire thermocouple and the cold-wire probe were elevated with increasing mass loading and decreasing distance from the wall. This was due to increasing particle concentration with increasing mass loading and

decreasing distance from the wall. The increasing particle concentrations were increased towards the wall was attributed to turbophoresis. The increased particle concentration resulted in more absorbing, intensely heated clusters, which caused increased mean temperatures and temperature fluctuations.

- The carrier phase temperature spectra at the center of the duct showed no sensitivity to changes in the mass loading ratio for the ranges of loadings examined. The spectra near the wall at $y^+ = 60$ showed a redistribution of energy from the higher frequencies (smaller scales) to the lower frequencies (larger scales) with increasing mass loading. This was attributed to the development of long, coherent particle streaks in the boundary layer; the longer timescales of coherence associated with these particles streaks resulted in increased contributions to lower frequency components of the temperature spectra.

- The particle number density - temperature cross-correlation measured in the duct flow showed a smaller than expected correlation coefficient at all loadings (around 0.4). The reduction in the correlation between the two quantities was attributed to cluster break-up and turbulent mixing. The number density - temperature coherence function showed that this mixing and cluster break-up occurred predominantly at smaller scales.

- For the expanded parameter space examined in the co-flowing jet, the scaling of the mean temperature rise was linear to increases in power and the thermal capacity ratio, indicating that the lowest order modeling assumption of the mean temperature rise scaling linearly with the incident power and thermal capacity ratio is an accurate assumption. Significant modification to the preferential concentration and turbulence from radiative heating on a bulk scale could be indicated by a change to this linear scaling, but this indicator was not observed in the mean temperature rise scaling.

- Measurements made in the co-flowing jet showed that radiative heating caused measurable changes in the preferential concentration. The radial distribution function showed a reduction in the RDF at smaller scales, and a small increase

in the larger scales when heating was introduced. The clustering index was globally reduced for all length scales examined by the quantity. The cell area PDFs from Voronoi decomposition showed decreased fraction of the smallest scale clusters, and a reduction of particle concentration within these clusters. All these statistics consistently indicated a reduction of preferential concentration within clusters, particularly in denser clusters with smaller associated separation length scales, which correspond to the most intensely heated regions of the flow.

- Measurements of particle velocities in the co-flowing jet when heating was introduced showed an increase in the mean particle velocity in the core of the jet due dilatation of the carrier phase gas, which was significant enough to cause bulk acceleration of the carrier phase in the core of the jet. The particle velocity fluctuations in the streamwise and wall-normal directions were reduced with heating contrary to expectations, as buoyancy and dilatational effects were expected to enhance carrier phase turbulence. It was hypothesized that variable property effects caused by carrier phase temperature changes were likely responsible for this dampening of the turbulence in the bulk, primarily through the increasing kinematic viscosity, while buoyancy and dilatation effects were acting at the smaller cluster scales.

- Scaling analyses derived from the thermal energy transport equation and continuity demonstrated that the time scales associated with buoyancy and dilatational effects at the cluster scale were comparable to large and intermediate eddy turnover times, implying that these effects could feasibly be modifying the preferential concentration and modulating the turbulence.

- The directional clustering index was measured, a clustering index computed in one specific dimension, to isolate specific mechanisms behind the changes in preferential concentration by heating. The wall-normal clustering index showed a measurable decrease in the clustering index with the addition of heating, providing evidence of dilatational effects modifying the preferential concentration (as buoyancy effects would only minimally manifest in directions other than the gravity-parallel direction). The streamwise clustering index showed a larger

change than that of the wall-normal direction, indicating that both dilatational effects and buoyancy effects contributed to modifying the preferential concentration in the streamwise direction, though the exact contributions of these effects could not be decoupled.

## 5.2 Future work

Numerous areas of this work could be expanded upon in future investigations. The instantaneous particle velocities could be measured with a high-speed camera and particle tracking velocimetry, which could provide a more in-depth characterization of the effect of heating on particle velocity statistics beyond just the mean and fluctuation RMS. Particle velocity PDF's and spectra would provide better insights into how changes in the particle motion caused by radiative heating are contributing to changes in their clustering behavior.

Another major area of further study would be performing carrier phase measurements in the presence of radiative heating. Carrier phase velocities and temperatures could not be measured in the current experiment, as hot-wire anemometry requires an isothermal flow, and the wire thickness required for cold-wire thermometry necessitated a probe too fragile to explore very high mass loadings. Much of the analysis behind determining the presence of dilatational and buoyancy effects can be made much more concrete with measurements of the carrier phase velocity and temperature in the heated mixture. The carrier phase velocity can potentially be measured with two-phase PIV, using smaller (or less dense) tracer particles in conjunction with the particle phase under study; alternatively a cross-wire probe capable of simultaneous measurement of carrier phase velocity and temperature could be used to which would also enable measurement of velocity-temperature correlations.

A further expanded parameter space could also be worth investigating, especially higher radiative heating. The changes to the preferential concentration were relatively subtle in the parameter space explored in this work; stronger coupling between the radiative heating and the preferential concentration would potentially allow observation of changes in the radiation transport caused by radiation-induced changes in the

clustering, and a deviation from the linear scaling between the radiative power and bulk quantities like the mean temperature. Changing the particle Stokes numbers could also be of interest, as Stokes numbers strongly govern the preferential concentration; sensitivities of different Stokes number regimes to modification of preferential concentration and turbulence by radiation could be of interest.

Finally, an alternative flow configuration could be worth exploring to better accommodate validation studies. A co-flowing jet is relatively complex and more difficult to characterize; a canonical flow geometry that is simple, can accommodate very high radiative fluxes, and has minimal contributions from boundary layers or secondary flows to isolate effects caused by the radiative coupling would be an ideal test bed.

# Bibliography

H Abdehkakha. *Computational Modeling of Wall-Bounded Particle-Laden Flows*. PhD thesis, Stanford University, 2017.

M Niazi Ardekani and Luca Brandt. Turbulence modulation in channel flow of finite-size spheroidal particles. *Journal of Fluid Mechanics*, 859:887–901, 2019.

Dominique Baillis and Jean-François Sacadura. Thermal radiation properties of dispersed media: theoretical prediction and experimental characterization. *Journal of Quantitative Spectroscopy and Radiative Transfer*, 67(5):327–363, 2000.

S Balachandar and John K Eaton. Turbulent dispersed multiphase flow. *Annual review of fluid mechanics*, 42:111–133, 2010.

A Banko. *Radiation Absorption by Inertial Particles in a Turbulent Square Duct Flow*. PhD thesis, Stanford University, 2018.

Andrew J Banko, Laura Villafañe, Ji Hoon Kim, Mahdi Esmaily, and John K Eaton. Stochastic modeling of direct radiation transmission in particle-laden turbulent flow. *Journal of Quantitative Spectroscopy and Radiative Transfer*, 226:1–18, 2019.

Jeremy Bec, Luca Biferale, Guido Boffetta, Antonio Celani, Massimo Cencini, Alessandra Lanotte, S Musacchio, and Federico Toschi. Acceleration statistics of heavy particles in turbulence. *Journal of Fluid Mechanics*, 550:349–358, 2006.

Michael J Benson and John K Eaton. *The effects of wall roughness on the particle velocity field in a fully developed channel flow*. PhD thesis, Stanford University Stanford, CA, 2003.

Andrew D Bragg, Peter J Ireland, and Lance R Collins. Mechanisms for the clustering of inertial particles in the inertial range of isotropic turbulence. *Physical Review E*, 92(2):023029, 2015.

E Brundrett and WD Baines. The production and diffusion of vorticity in duct flow. *Journal of Fluid Mechanics*, 19(3):375–394, 1964.

L Chen, S Goto, and JC Vassilicos. Turbulent clustering of stagnation points and inertial particles. *Journal of Fluid Mechanics*, 553:143–154, 2006.

SW Coleman and JC Vassilicos. A unified sweep-stick mechanism to explain particle clustering in two-and three-dimensional homogeneous, isotropic turbulence. *Physics of Fluids*, 21(11):113301, 2009.

Clayton T Crowe, John D Schwarzkopf, Martin Sommerfeld, and Yutaka Tsuji. *Multiphase flows with droplets and particles*. CRC press, 2011.

CT Crowe, JN Chung, and TR Troutt. Particle mixing in free shear flows. *Progress in energy and combustion science*, 14(3):171–194, 1988.

Qi Dai, Kun Luo, Tai Jin, and Jianren Fan. Direct numerical simulation of turbulence modulation by particles in compressible isotropic turbulence. *Journal of Fluid Mechanics*, 832:438–482, 2017.

R Gonçalves dos Santos, Mickael Lecanu, Sébastien Ducruix, Olivier Gicquel, Estelle Iacona, and Denis Veynante. Coupled large eddy simulations of turbulent combustion and radiative heat transfer. *Combustion and Flame*, 152(3):387–400, 2008.

John K Eaton and JR Fessler. Preferential concentration of particles by turbulence. *International Journal of Multiphase Flow*, 20:169–209, 1994.

C Elkins. *Heat transfer in the rotating disk boundary layer*. PhD thesis, Stanford University, 1997.

M Esmaily, L Villafane, AJ Banko, G Iaccarino, JK Eaton, and A Mani. A benchmark for particle-laden turbulent duct flow: A joint computational and experimental study. *International Journal of Multiphase Flow*, 132:103410, 2020.

Mahdi Esmaily-Moghadam and Ali Mani. Analysis of the clustering of inertial particles in turbulent flows. *Physical Review Fluids*, 1(8):084202, 2016.

Antonino Ferrante and Said Elghobashi. On the physical mechanisms of two-way coupling in particle-laden isotropic turbulence. *Physics of fluids*, 15(2):315–329, 2003.

A Frankel, G Iaccarino, and A Mani. Optical depth in particle-laden turbulent flows. *Journal of Quantitative Spectroscopy and Radiative Transfer*, 201:10–16, 2017.

S Gavrilakis. Numerical simulation of low-reynolds-number turbulent flow through a straight square duct. *Journal of Fluid Mechanics*, 244:101–129, 1992.

FB Gessner. The origin of secondary flow in turbulent flow along a corner. *Journal of Fluid Mechanics*, 58(1):1–25, 1973.

RA Gore and Clayton T Crowe. Effect of particle size on modulating turbulent intensity. *International Journal of Multiphase Flow*, 15(2):279–285, 1989.

Kuniaki Gotoh, Shuhei Yamada, and Tatsuo Nishimura. Influence of thermal convection on particle behavior in solid-liquid suspensions. *Advanced Powder Technology*, 15(5):499–514, 2004.

F Grinstein and C DeVore. Coherent-structure dynamics in spatially developing square jets. In *28th Joint Propulsion Conference and Exhibit*, page 3441, 1992.

EJ Gutmark and FF Grinstein. Flow control with noncircular jets. *Annual review of fluid mechanics*, 31(1):239–272, 1999.

G Hetsroni. Particles-turbulence interaction. *International Journal of Multiphase Flow*, 15(5):735–746, 1989.

G. Hetsroni and M. Sokolov. Distribution of Mass, Velocity, and Intensity of Turbulence in a Two-Phase Turbulent Jet. *Journal of Applied Mechanics*, 38(2):315–327, 1971.

WGI IPCC. Climate change 1995-the science of climate change. contribution of working group i to the second assessment report of the intergovernmental panel on climate change. *JT Houghton et al*, 1995.

John Kim and Parviz Moin. Transport of passive scalars in a turbulent channel flow. In *Turbulent Shear Flows 6*, pages 85–96. Springer, 1989.

Alexander B Kostinski. On the extinction of radiation by a homogeneous but spatially correlated random medium. *JOSA A*, 18(8):1929–1933, 2001.

Jonathan D Kulick, John R Fessler, and John K Eaton. Particle response and turbulence modification in fully developed channel flow. *Journal of Fluid Mechanics*, 277:109–134, 1994.

J Kussin and M Sommerfeld. Experimental studies on particle behaviour and turbulence modification in horizontal channel flow with different wall roughness. *Experiments in Fluids*, 33(1):143–159, 2002.

Timothy CW Lau and Graham J Nathan. Influence of stokes number on the velocity and concentration distributions in particle-laden jets. *Journal of fluid mechanics*, 757:432–457, 2014.

BE Launder and WM Ying. Prediction of flow and heat transfer in ducts of square cross-section. *Proceedings of the Institution of Mechanical Engineers*, 187(1):455–461, 1973.

Chung K. Law. Combustion physics, 2006.

Francesco Lucci, Antonino Ferrante, and Said Elghobashi. Is stokes number an appropriate indicator for turbulence modulation by particles of taylor-length-scale size? *Physics of Fluids*, 23(2):025101, 2011.

Christian Mätzler. Matlab functions for mie scattering and absorption, version 2. *IAP Res. Rep*, 8(1):9, 2002.

Martin R Maxey. The gravitational settling of aerosol particles in homogeneous turbulence and random flow fields. *Journal of Fluid Mechanics*, 174:441–465, 1987.

Daniel W Meyer. Modelling of turbulence modulation in particle-or droplet-laden flows. *Journal of fluid mechanics*, 706:251–273, 2012.

Romain Monchaux, Mickael Bourgoin, and Alain Cartellier. Analyzing preferential concentration and clustering of inertial particles in turbulence. *International Journal of Multiphase Flow*, 40:1–18, 2012.

Johann Nikuradse. Untersuchungen uber die geschwindigkeits-verteilung in turbulenten stromungen vdi. *Forschungsheft*, 291, 1926.

Y Ninto and Marcelo Horacio Garcia. Experiments on particle—turbulence interactions in the near–wall region of an open channel flow: implications for sediment transport. *Journal of Fluid Mechanics*, 326:285–319, 1996.

Paolo Oresta and Andrea Prosperetti. Effects of particle settling on rayleigh-bénard convection. *Physical Review E*, 87(6):063014, 2013.

AD Paris and JK Eaton. Turbulence attenuation in particle-laden channel flow. report no. tsd-137, dept. *Mech. Engr., Stanford University*, 2001.

C Poelma, J Westerweel, and G Ooms. Particle–fluid interactions in grid-generated turbulence. *Journal of Fluid Mechanics*, 589:315–351, 2007.

Hadi Pouransari and Ali Mani. Effects of preferential concentration on heat transfer in particle-based solar receivers. *Journal of Solar Energy Engineering*, 139(2), 2017.

WR Quinn. Streamwise evolution of a square jet cross section. *AIAA journal*, 30 (12):2852–2857, 1992.

MW Reeks. The transport of discrete particles in inhomogeneous turbulence. *Journal of aerosol science*, 14(6):729–739, 1983.

Damian WI Rouson and John K Eaton. On the preferential concentration of solid particles in turbulent channel flow. *Journal of Fluid Mechanics*, 428:149, 2001.

Yohei Sato, Koichi Hishida, and Masanobu Maeda. Effect of Dispersed Phase on Modification of Turbulent Flow in a Wall Jet. *Journal of Fluids Engineering*, 118 (2):307–315, 1996.

PM Sforza, MH Steiger, and N Trentacoste. Studies on three-dimensional viscous jets. *AIAA journal*, 4(5):800–806, 1966.

Raymond A Shaw, Alexander B Kostinski, and Daniel D Lanterman. Super-exponential extinction of radiation in a negatively correlated random medium. *Journal of quantitative spectroscopy and radiative transfer*, 75(1):13–20, 2002.

Kyle D Squires and John K Eaton. Preferential concentration of particles by turbulence. *Physics of Fluids A: Fluid Dynamics*, 3(5):1169–1178, 1991.

Tomohiko Tanaka and John K Eaton. Classification of turbulence modification by dispersed spheres using a novel dimensionless number. *Physical Review Letters*, 101 (11):114502, 2008.

Yutaka Tsuji, Yoshinobu Morikawa, and Hiroshi Shiomi. Ldv measurements of an air-solid two-phase flow in a vertical pipe. *Journal of Fluid Mechanics*, 139:417–434, 1984.

A Yu Varaksin, Yu V Polezhaev, and Anatoly F Polyakov. Effect of particle concentration on fluctuating velocity of the disperse phase for turbulent pipe flow. *International journal of heat and fluid flow*, 21(5):562–567, 2000.

Ricardo Vinuesa, Azad Noorani, Adrián Lozano-Durán, George K El Khoury, Philipp Schlatter, Paul F Fischer, and Hassan M Nagib. Aspect ratio effects in turbulent duct flows studied through direct numerical simulation. *Journal of Turbulence*, 15 (10):677–706, 2014.

Stephen Whitaker. Forced convection heat transfer correlations for flow in pipes, past flat plates, single cylinders, single spheres, and for flow in packed beds and tube bundles. *AIChE Journal*, 18(2):361–371, 1972.

Donald E Wroblewski and Pamela A Eibeck. A frequency response compensation technique for cold wires and its application to a heat flux probe. *Experimental thermal and fluid science*, 4(4):452–463, 1991.

Hiroshi Yoshimoto and Susumu Goto. Self-similar clustering of inertial particles in homogeneous turbulence. *Journal of Fluid Mechanics*, 577:275–286, 2007.

Andrew Youdin and Anders Johansen. Protoplanetary disk turbulence driven by the streaming instability: linear evolution and numerical methods. *The Astrophysical Journal*, 662(1):613, 2007.

Rémi Zamansky, Filippo Coletti, Marc Massot, and Ali Mani. Radiation induces turbulence in particle-laden fluids. *Physics of Fluids*, 26(7):071701, 2014.

Rémi Zamansky, Filippo Coletti, Marc Massot, and Ali Mani. Turbulent thermal convection driven by heated inertial particles. *Journal of Fluid Mechanics*, 809: 390–437, 2016.

Francesco Zonta, Cristian Marchioli, and Alfredo Soldati. Direct numerical simulation of turbulent heat transfer modulation in micro-dispersed channel flow. *Acta Mechanica*, 195(1-4):305–326, 2008.